AFRL-RX-TY-TR-2008-4603

RESISTANCE OF MULTI-WYTHE INSULATED MASONRY WALLS SUBJECTED TO IMPULSE LOADS – (VOLUME I)

Robert S. Browning and James S. Davidson
Auburn University
Department of Civil Engineering
238 Harbert Engineering Center
Auburn, AL 36849-5337

Robert J. Dinan, PhD
Air Force Research Laboratory
139 Barnes Drive, Suite 2
Tyndall AFB, FL 32403-5323

DECEMBER 2008

Interim Report for 1 May 2006 – 30 September 2008

AIRBASE TECHNOLOGIES DIVISION
MATERIALS AND MANUFACTURING DIRECTORATE
AIR FORCE RESEARCH LABORATORY
AIR FORCE MATERIEL COMMAND
139 BARNES DRIVE, SUITE 2
TYNDALL AIR FORCE BASE, FL 32403-5323

NOTICE AND SIGNATURE PAGE

Using Government drawings, specifications, or other data included in this document for any purpose other than Government procurement does not in any way obligate the U.S. Government. The fact that the Government formulated or supplied the drawings, specifications, or other data does not license the holder or any other person or corporation; or convey any rights or permission to manufacture, use, or sell any patented invention that may relate to them.

This report was cleared for public release by the Air Force Research Laboratory, Materials and Manufacturing Directorate, Airbase Technologies Division, Public Affairs and is available to the general public, including foreign nationals. Copies may be obtained from the Defense Technical Information Center (DTIC) (http://www.dtic.mil).

REPORT NUMBER AFRL-RX-TY-TR-2008-4603 HAS BEEN REVIEWED AND IS APPROVED FOR PUBLICATION IN ACCORDANCE WITH ASSIGNED DISTRIBUTION STATEMENT.

This report is published in the interest of scientific and technical information exchange, and its publication does not constitute the Government's approval or disapproval of its ideas or findings.

REPORT DOCUMENTATION PAGE

1. REPORT DATE *(DD-MM-YYYY)*	2. REPORT TYPE	3. DATES COVERED *(From - To)*

4. TITLE AND SUBTITLE	5a. CONTRACT NUMBER
	5b. GRANT NUMBER
	5c. PROGRAM ELEMENT NUMBER
6. AUTHOR(S)	5d. PROJECT NUMBER
	5e. TASK NUMBER
	5f. WORK UNIT NUMBER

7. PERFORMING ORGANIZATION NAME(S) AND ADDRESS(ES)	8. PERFORMING ORGANIZATION REPORT NUMBER

9. SPONSORING/MONITORING AGENCY NAME(S) AND ADDRESS(ES)	10. SPONSOR/MONITOR'S ACRONYM(S)
	11. SPONSOR/MONITOR'S REPORT NUMBER(S)

12. DISTRIBUTION/AVAILABILITY STATEMENT

13. SUPPLEMENTARY NOTES

14. ABSTRACT

15. SUBJECT TERMS

16. SECURITY CLASSIFICATION OF:			17. LIMITATION OF ABSTRACT	18. NUMBER OF PAGES	19a. NAME OF RESPONSIBLE PERSON
a. REPORT	b. ABSTRACT	c. THIS PAGE			
					19b. TELEPHONE NUMBER *(Include area code)*

RESISTANCE OF MULTI-WYTHE INSULATED
MASONRY WALLS SUBJECTED TO IMPULSE LOADS
VOLUME I

Robert S. Browning and James S. Davidson
Auburn University

A technical report submitted to:

December 2008

ABSTRACT

RESISTANCE OF MULTI-WYTHE INSULATED MASONRY

WALLS SUBJECTED TO IMPULSE LOADS

The overall objective of this project was to define the dynamic flexural resistance of multi-wythe insulated masonry walls with specific emphasis placed on determining the potential application of foam insulation as a blast-resistant material. The project was closely coordinated with full-scale explosive testing conducted by personnel at the Airbase Technologies Division of the Air Force Research Laboratory (AFRL) at Tyndall Air Force Base Florida. The project involved the following tasks: (1) use of finite element (FE) and single-degree-of-freedom (SDOF) analytical models for test analysis and prediction of results, (2) identification of the constitutive relationships of insulating foam(s), (3) synthesis of full-scale test methodology and results, (4) utilization of the data gathered from the full-scale tests to validate the FE models, (5) implementation of input parameter studies using the advanced FE models to characterize the mechanical behavior of the systems tested, and (6) development of engineering-level resistance definitions and multi-degree-of-freedom models of multi-wythe insulated masonry walls. Four standard wall section designs were recommended by the National Concrete Masonry Association (NCMA). Of these designs, two were selected for full-scale testing: a conventional block wall with a brick veneer and an A-block wall with a brick veneer - both with extruded polystyrene board insulation in the cavity and cells fully grouted. A single-wythe control wall with equivalent mass and flexural capacity was also included in the tests. FE models were used to assess the ability of the insulation to reduce the peak deflection of masonry walls subjected to impulse loads. Observations regarding the crushing of the insulation during the full-scale testing are also presented.

TABLE OF CONTENTS

LIST OF TABLES

LIST OF FIGURES

viii

CHAPTER 1

INTRODUCTION

1.1 Overview

In the years following September 11, 2001, there has been much publicity given to the need for structures to be hardened against terrorist attacks. Because of the surge of interest in this field of study, many organizations have decided to fund research in this specialized area of structural design. However, this area of study is not a new idea; throughout the years, many scientists and engineers have sought a clearer understanding of the damage caused by explosions. Their research has led to many design aids that are presently used in the design of critical facilities. One challenge that the design engineer faces is that not only must the strength of the structure be designed, but also an appropriate level of protection must be determined to identify the dynamic load that the structure should be designed to resist.

Blast-resistant design stands out from design to resist wind or earthquake loads since, typically, the structure is not expected to be completely functional after being subjected to a terrorist attack. The primary goal is simply to protect the occupants of the structure. Explosive attacks produce significant fragmentation, which in turn leads to significant casualties. Therefore, by reducing the fragmentation of a structure, harm to the occupants is also reduced.

If safety deems it necessary, the methods and procedures developed here can be applied to any structure. This work, however, is focused on the design of blast-resistant walls for high-risk facilities. The wall sections under investigation are fully grouted multi-wythe masonry walls with polystyrene foam insulation between the wythes. The interest here is in the capability of the extruded polystyrene thermal board insulation to absorb energy and subsequently enhance the overall dynamic resistance of the wall section.

The wall sections investigated were proposed by the National Concrete Masonry Association (NCMA). The full-scale dynamic testing of these sections was conducted by personnel at the Airbase Technologies Division of the Air Force Research Laboratory (AFRL). The challenge with test such as these, outside of the expense to conduct them, is the difficulty in collecting useful data. Even with the use of sophisticated high-speed cameras and gauges, recording the response of the wall is very difficult due to the debris and dust prevalent during an explosive test, and to the simple fact that the response takes less than one second to occur. Because of the problems and expense associated with full-scale testing, the use of finite element (FE) methods becomes necessary. FE models economically facilitate the investigation of the structural response of various wall geometries, as well as of dynamic material properties when the wall is subjected to a broad range of dynamic loads.

1.2 Objectives

The overall objective of this project was to develop methodology for use in predicting the dynamic flexural capacity of multi-wythe insulated masonry walls.

Therefore, it was necessary to identify whether or not the foam insulation enhances the overall resistance of the system.

1.3 Scope and Methodology

This effort included laboratory testing, full-scale dynamic testing, development of engineering-level (EL) models, and development of FE models. The laboratory testing included tests of the compressive strength of grout specimens, as well as tests of the stress-strain properties of foam insulation. The testing of the grout was conducted by technicians at AFRL. The testing of foam was conducted using facilities located within the Biomedical Engineering Department at the University of Alabama at Birmingham.

Development of EL models was performed using Microsoft Visual Basic in combination with Microsoft Excel. This choice of software packages provided a portable model that could easily be shared with other researchers on the project. All of the FE models were developed and analyzed using a combination of HyperWorks v7.0 developed by Altair Engineering, Inc., Finite Element Model Builder (FEMB v28.0) developed by Engineering Technology Associates, Inc., LS-PrePost developed by Livermore Software Technology Corporation (LSTC), and LS-DYNA v971 also developed by LSTC. Two tools were utilized from the HyperWorks suite: HyperMesh and HyperView. HyperMesh was used to generate the initial FE model. FEMB and LS-PrePost were then used to make further adjustments to the model. Once the model was finished, it was analyzed using LS-DYNA, which is an advanced general-purpose nonlinear FE program, capable of simulating complex mechanics problems, that is based on an explicit solution. Since LS-DYNA has a wide variety of material models and can

be used on multiple processors, it was deemed suitable for this project. Smaller models

were analyzed using a dual-processor workstation, while more sophisticated models were

analyzed using a 128-processor supercomputer using the Massively Parallel Processor

(MPP) version of LS-DYNA. The results were post-processed using HyperView and LS-

PrePost.

1.4 Report Organization

This report consists of six chapters. Chapter 1 describes the objectives, scope,

methodology, and organization of the report. Chapter 2 provides a review of the

technical background via relevant literature. Chapter 3 describes the testing conducted

throughout the course of the project. Chapter 4 describes the development of the FE

models and presents the FE analysis results. Chapter 5 discusses the use and

development of EL models and presents the EL analysis results. Chapter 6 summarizes

the report and presents conclusions; it also makes recommendations concerning future

work. The report concludes with a list of references and an appendix.

CHAPTER 2

TECHNICAL BACKGROUND

2.1 Overview

Due to the recent heightened emphasis on designing structures that are blast-resistant, many materials are being investigated so that their energy-absorbing abilities may be characterized. A very common type of construction procedure utilizes the multi-wythe (veneer) insulated concrete masonry wall section. This type of section typically consists of a loadbearing masonry wall on the interior side of the building (with the option of being fully grouted), includes some type of insulating material, and includes an exterior nonloadbearing masonry wythe that could be either concrete or clay masonry.

Because the flexural strength of concrete is extremely low, some type of reinforcement is necessary so that the full compressive strength of the concrete can be developed under lateral loads. Masonry walls are reinforced by placing reinforcing steel in the cells of the wall and then filling the cells with grout. Reinforcement can be placed in both the vertical and horizontal directions. If all of the cells are grouted, whether they have reinforcing steel or not, then the wall is said to be fully grouted. Because the mass of a structure in dynamic loading plays an important role in the overall resistance, fully grouted wall sections generally perform much better than ungrouted sections.

Over the years, a great deal of effort has gone into the study of the blast resistance of concrete and masonry walls. However, recent research has focused on more advanced

materials. In this report, the investigation is focused on the insulating material found in a typical masonry wall section. In most cases of multi-wythe wall construction, the insulation consists of extruded polystyrene (XEPS) thermal board insulation. One of the goals of the project was to determine if the foam insulation provides energy absorption to the system by distributing the total impulse over a longer time, thus lowering the value of the peak force applied to the interior wythe.

2.2 Blast Loading

The data collected during explosive testing is often very limited due to the large amounts of dust, debris, and vibration that are present during an explosion. However, typical data that can be collected with reasonable levels of risk to the testing equipment include deflection histories, reflected pressure histories, and high-speed video recordings. When this data is successfully collected, the analyst can gain an understanding of the response of the system.

A blast can be simply described as "the violent effect produced in the vicinity of an explosion;" in more technical terms, a blast "consists of a shock accompanied by an instantaneous increase in ambient atmospheric pressure followed by a monotonic decrease in pressure below the local atmospheric pressure" (Tedesco et al. 1999). Typically, a blast is the result of an explosion, which is defined as "a sudden expansion of some energy source" (Tedesco et al. 1999). An explosion can be caused by many different configurations ranging from handguns to nuclear bombs. The effectiveness of an explosion is dependent on the type of material used to generate it and is generally described in terms of the peak pressure and impulse. An explosive material's

effectiveness is generally expressed in terms of its trinitrotoluene (TNT) equivalence, which may be calculated using either volume or weight. The equation defining TNT equivalence is as follows:

$$W_E = \frac{H_{EXP}^d}{H_{TNT}^d} \cdot W_{EXP} \tag{2-1}$$

where W_E is the effective charge weight, W_{EXP} is the charge weight of the explosive, H_{EXP}^d is the heat of detonation of the explosive, and H_{TNT}^d is the heat of detonation of TNT.

In general, an explosion generates a circular shock front that propagates away from the origin of the charge. This shock front possesses an associated overpressure traveling with a unique velocity; the overpressure is the excess above atmospheric pressure. The shock front has a peak pressure p_{so} that decays with time. The overpressure starts out positive and decays nonlinearly until it is below atmospheric pressure. The loading that is above atmospheric pressure applies a compressive pressure to the structure and is known as the positive phase. The loading that is below atmospheric pressure applies a tensile pressure, or suction, to the structure and is known as the negative phase. In many structural design applications, the negative phase can be ignored. When the shock front strikes the plane of an object oriented normal to the direction the shock front is traveling, a reflected pressure is produced that is an instantaneous increase above the shock front (Biggs 1964). This reflected pressure is generally the pressure that the structure is designed to resist. Figure 2.1 shows the general nature of an arbitrary blast load applied to a structure. There are many resources pertaining to the calculation of this pressure, including the ones referenced here.
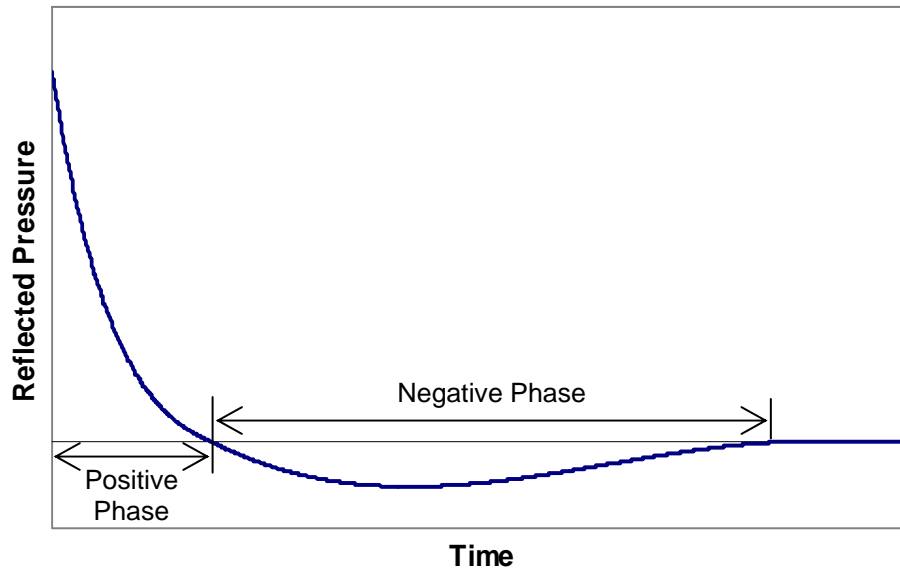
Fig. 2.1. Arbitrary blast load

2.3 Masonry Walls

Many single-story structures that must be designed for blast resistance are constructed using masonry walls. Through the use of multi-wythe wall sections with appropriate insulating materials, a resilient and comfortable structure can be built efficiently. Much research has already been performed on masonry walls subjected to impulse loads (U.S. Army et al. 1990). Oftentimes, prediction analyses are conducted using dynamic finite element (FE) methods.

An important factor in predicting the ultimate resistance of masonry walls is the variance in the constitutive properties of the materials. Eamon et al. (2004), after modeling grouted and ungrouted concrete masonry unit (CMU) walls with DYNA3D and comparing the FE results to test data, stated that models can "replicate experimental results if material parameters are set within [a] reasonably expected range of variation." They also pointed out that "the real value of a model is its ability to predict experimental

8

data," as opposed to mimicking pre-modeling test results. Their summary concluded that an accurate model using average material parameters is unlikely due to the high variations of such parameters. Therefore, since FE modeling can be computationally expensive, a simpler method for design purposes should be sought.

A more economical solution method for creating a practical design tool is the development of a single-degree-of-freedom (SDOF) approach like that described by John Biggs (1964) in his book *Introduction to Structural Dynamics*. This approach is very common, and the methodology is prevalent in most structural dynamics texts. Specific application of this method to different types of structures can be found in the manual jointly written by personnel at the Departments of the U.S. Army, Navy, and Air Force (1990) and titled *Structures to Resist the Effects of Accidental Explosions*. In the blast design community it is commonly referred to by its U.S. Army report number, TM 5-1300.

The presence or absence of reinforcing steel or grout dramatically alters the behavior of the system. For non-reinforced, ungrouted masonry walls subjected to blast loads, the failure will typically occur at the mortar joints (Dennis et al. 2002). In an effort to improve the Wall Analysis Code (WAC), which is a SDOF code used for blast design, Baylot et al. (2005) conducted testing on 1/4-scale models and achieved results which concurred with Dennis et al. They observed that WAC performed reasonably well for debris velocity predictions when resistance function data was available, thus supporting the need for clearly defined material properties.

Chapter 6 of TM 5-1300 addresses "special considerations in explosive facility design" and supplies design guidelines for masonry walls, precast elements, and

connections. TM 5-1300 states that the determination of the ultimate moment capacity of

a fully grouted masonry wall is based on the same methods as those used for standard

reinforced concrete (U.S. Army et al. 1990). While this simplifies the analysis of the

wall, it does not eliminate problems associated with accurate prediction of the response

caused by the variations in material properties. Therefore, safety factors are used so that

the lower bound of the strength of the material is sufficient to carry the design load.

Because the cost of a high-risk structure can become considerably large, research efforts

are focusing on learning more about advanced materials to help maintain economy in

design.

2.4 Foam Insulation

Virtually all buildings require insulation so that they can be economically heated

and cooled. Depending on the type of masonry wall under consideration (single- or

multi-wythe, partially or fully grouted), there are several insulation methods. Typical

forms of insulation that can be added to masonry walls are loose fill, foam fill, and rigid

board materials. Loose fill materials are a granular type of insulating material that must

be poured into the cells of an ungrouted masonry wall. Two types of granular fill that

have been used for this are vermiculite and perlite treated with water-repellent (Beall

1993). Rigid insulation materials can also be formed into shapes that can be inserted into

cells prior to construction, thus achieving the same effect as the loose fill insulation.

These two insulating methods allow a single-wythe wall to be exposed on both sides, and

at the same time, to possess extra insulation. The shortcoming of these methods is that

they cannot be used if the wall is fully grouted.

A masonry veneer with masonry backup and an air space between the masonry wythes is a very popular wall system. It offers many advantages including the ability to apply a wide variety of architectural treatments, excellent resistance to moisture penetration and wind-driven rain, as well as provision of a convenient location for insulation. This arrangement allows a layer of rigid board insulation to be placed between the wythes; it is fastened to the interior wall by adhesives or mechanical fasteners.

Rigid board insulation can be made of fibrous or cellular material. Fibrous insulation is comprised of materials such as wood or mineral fibers and is constructed using plastic binders. Cellular insulation, which is the type considered in this study, can be composed of materials such as polystyrene, polyurethane, and polyisocyanurate (Beall 1993). In this study, the rigid board insulation used is technically known as rigid closed-cell extruded polystyrene (XEPS) thermal board insulation.

The XEPS foam chosen, unlike many foams used for impact energy absorption, is initially stiff. That characteristic, along with its very low density, is beneficial during construction. However, for energy absorption, the initial stiffness is not necessarily beneficial. On the other hand, the ability of XEPS to compress to very high strains is beneficial. This trait of XEPS was anticipated to allow it to spread out the impulse generated by a blast, thus reducing the force imparted to the wall.

Similar research has been conducted to determine the ability of foam to reduce the force imparted to a system. Kostopoulos et al. (2002) conducted FE analyses on motorcycle safety helmets using LS-DYNA to study the energy absorption during an impact. The study included modeling of the expanded polystyrene (EPS) foam liner

11

inside the outer shell of the helmet. The authors made two major assumptions in the modeling of the EPS foam: 1) that the foam was isotropic, and 2) that the six stress components were uncoupled. The second assumption results in an x-component of strain only generating resistance in the x-direction, thus resulting in Poisson's ratio $v = 0$.

Chang et al. (1994) created a material model to describe the behavior of foams with low Poisson's ratios, which they referred to as slow-recovery foams. They reported that these types of materials would not expand laterally, even when compressive strains in the longitudinal direction were on the order of 70%. Chang et al. incorporated their material model into LS-DYNA's material library and compared FE results to laboratory testing.

Bielenberg and Reid (2004) modeled polystyrene foam using LS-DYNA for a study in which the foam was used as part of an energy-absorbing barrier for high-speed racetracks. They used one of the less robust foam material models, *MAT CRUSHABLE FOAM, available in LS-DYNA. This model allowed them to enter stress-versus-volumetric strain data consistent with the polystyrene foam. They reported issues with negative volume errors during simulation, as well as the subsequent steps taken to work around such problems. They found that when modeling foam that was to be severely crushed, it was best to use the fully integrated solid element formulation. They also found that LS-DYNA's *CONTACT INTERIOR option could be used by the analyst to control the peak loads (seen once the foam had reached its maximum compressive strain).

Another type of foam showing potential in the area of impact- and explosion-resistance is aluminum foam. Like typical plastic foams such as polystyrene, aluminum

foam can lower the induced force applied to a system by absorbing energy, effectively slowing the forcing object. Aluminum foams may be able to add the same resistance as plastic foams with much thinner sections. However, there are three reasons that aluminum foams may not be the better choice. First, aluminum is much more expensive than plastic; second, some form of thermal insulation could still be required; third, aluminum reacts chemically with the alkalis in the cement. These issues necessitate the investigation of both options so that the most efficient solution can be used for specific cases. Recently, research concerning aluminum foams has been conducted and documented by Hanssen et al. (2002), Schenker et al. (2005), and Ye and Ma (2007). The effort reported here, however, is one of the first to study the potential of plastic foams in the area of blast resistance.

It is likely that aluminum and plastic foams can be analyzed in the same fashion once the general methodology is understood. While the modeling approach taken by the previous researchers was sound, a different method was required for this project because the aforementioned investigators assumed that the supporting structure behaved elastically. Their work typically considered a steel section for the supporting structure. While it is possible for the supporting structure to remain elastic, it is not a practical assumption for reinforced masonry. Reinforced masonry performs well under impulse loads due to its large amount of mass in conjunction with the ductility provided by reinforcing steel. However, this type of resistance mechanism relies on the structure's ability to sustain large plastic deformations, which negates the use of an elastic solution. Complete details of the modeling methodology for this project are presented in Chapters 4 and 5.

13

CHAPTER 3

TESTING

3.1 Overview

One of the primary focuses of this project was to investigate the effect that the

extruded polystyrene (XEPS) insulation had on the overall dynamic resistance of the

system. Testing was conducted to quantify the constitutive properties of the foam. The

compressive strength of the grout used during construction was also tested. Finally, the

overall resistance of the system was investigated via full-scale dynamic tests. The

purpose of this chapter is to define the steps that were taken in carrying out each of these

investigations and to present the data collected from each respective investigation.

3.2 Static Testing

To facilitate accurate modeling of the wall sections, laboratory testing was

conducted so that the material properties of the component materials would be known

and understood. The results from the compressive strength tests of the grout specimens

will be presented first, followed by the results of the XEPS foam tests.

3.2.1 Grout Compressive Strength

When the wall sections were constructed, eight grout samples were made in the

form of cylinders. The cylinders were tested at approximately the same time that the

dynamic testing of the wall sections was conducted, so that their strengths would remain

reasonably close to that of the wall sections. Standard compressive tests were conducted

for all eight cylinders. The diameter of each cylinder was approximately 5.9 inches,

resulting in a cross-sectional area of 27.34 square inches. The results are shown in Table

3.1. The average compressive strength was approximately 4,700 psi.

Table 3.1. Grout compressive strengths

Specimen	Failure Load (lb)	Compressive Strength (psi)
1	130,100	4,760
2	125,400	4,590
3	140,500	5,140
4	156,900	5,740
5	119,700	4,380
6	122,700	4,490
7	132,500	4,850
8	102,500	3,750

3.2.2 XEPS Foam Static Testing

Samples were taken from three different manufacturers' products and were tested

in a laboratory. Although only one manufacturer's product was used in the construction

of the walls, different products were tested to identify any major differences in their

overall behavior. Figures 3.1 through 3.4 show the lab equipment that was used and the

testing sequence for one of the foam samples. Figures 3.5 through 3.7 graphically

present the data gathered from laboratory testing, and Table 3.2 summarizes the data. A

thorough description of this series of tests is presented in the report by Randall Jenkins

(2008). The data collected from this series of tests were implemented into numerical

15

models so that the energy absorption capabilities could be studied. This process is

described in detail in Chapters 4 and 5.

Fig. 3.1. Test equipment for foam

Fig. 3.2. Foam specimens

Fig. 3.3. Testing configuration for foam
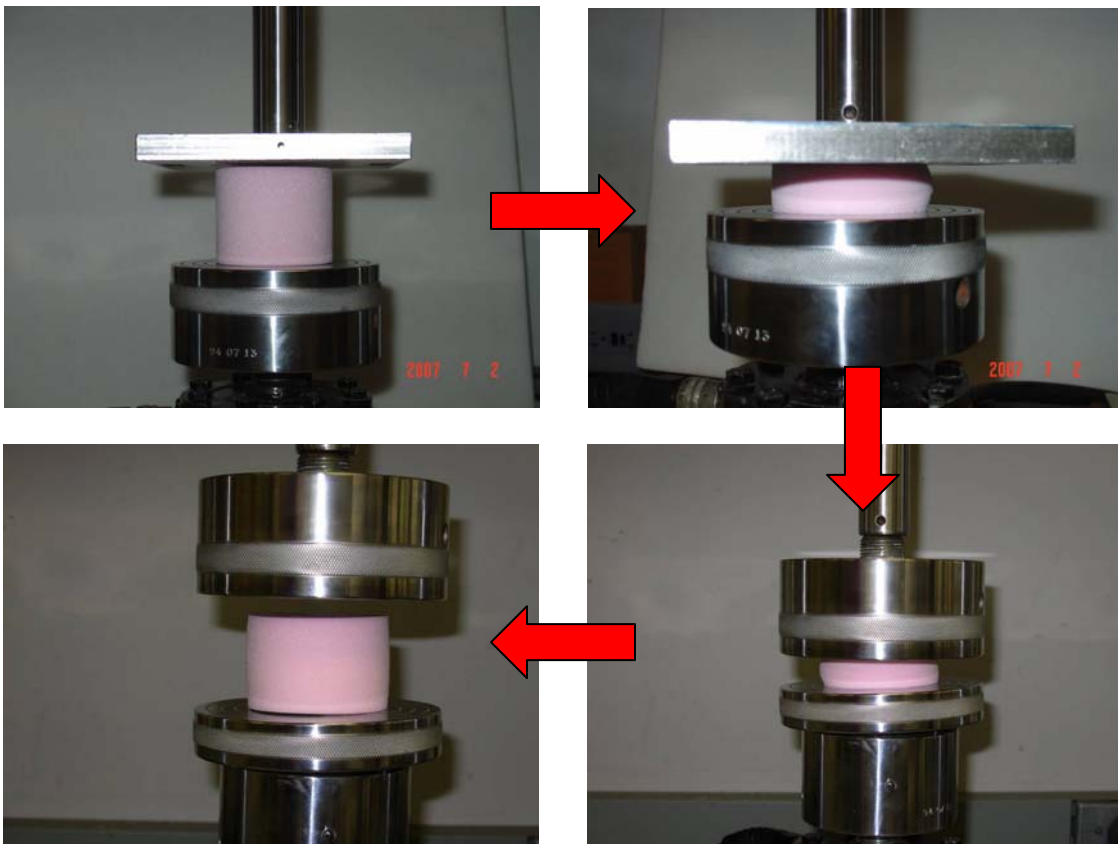
Fig. 3.4. Loading of a foam specimen

17
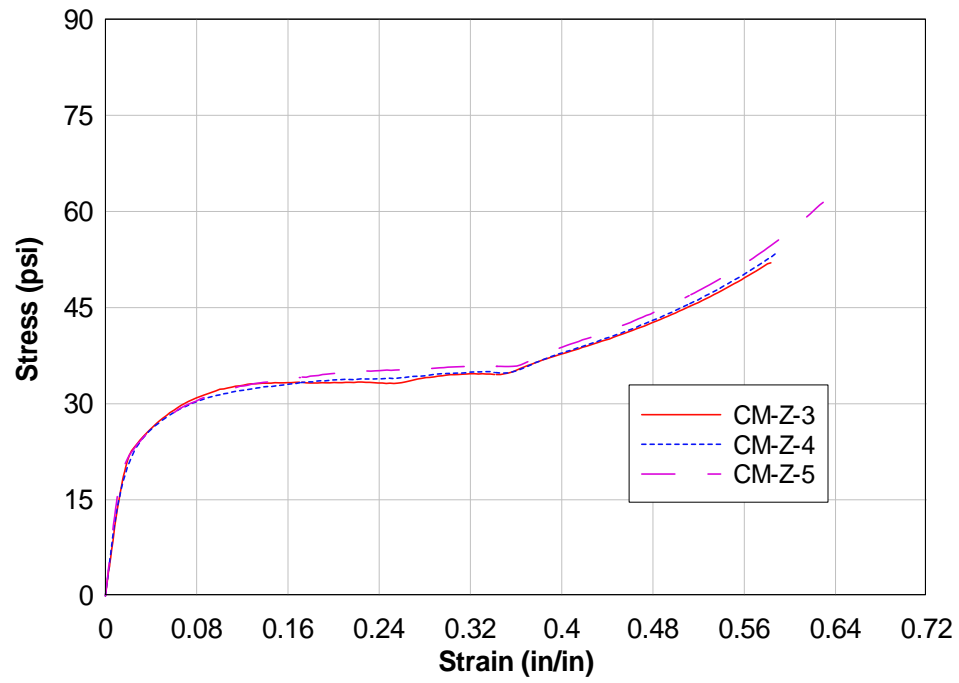
Fig. 3.5. Stress-strain behavior of Owens-Corning XEPS foam
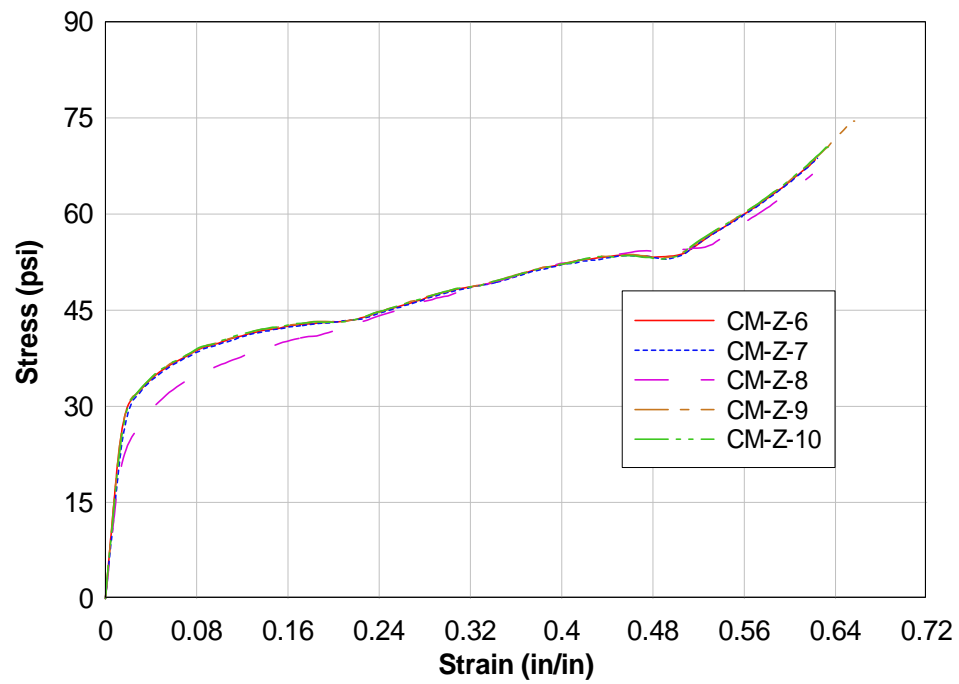
Fig. 3.6. Stress-strain behavior of Dow XEPS foam

18
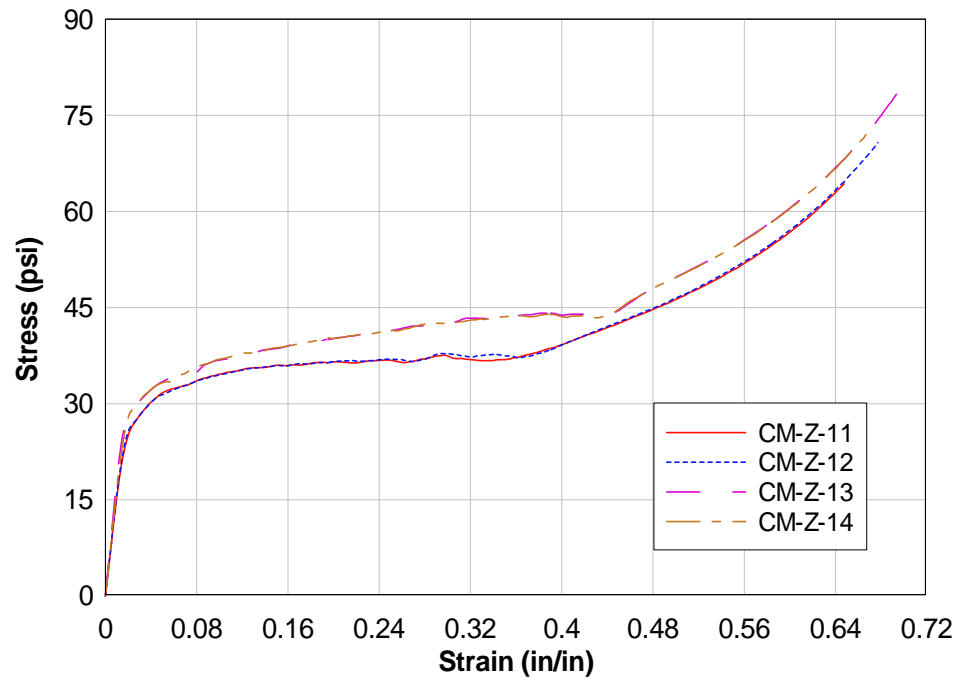
Fig. 3.7. Stress-strain behavior of Pactiv XEPS foam

Table 3.2. Summary of test results for XEPS foam

Manufacturer	Specimen	Nominal Gage Section (in)	Density (lb/ft^3)	Elastic Modulus (ksi)	Compressive Strength (psi)
Owens-Corning	CM-Z-3	2.50 dia x 2.0	1.507	1.31	32
Owens-Corning	CM-Z-4	2.50 dia x 2.0	1.511	1.43	31
Owens-Corning	CM-Z-5	2.50 dia x 2.0	1.502	1.55	32
Dow	CM-Z-6	2.50 dia x 2.0	1.707	2.00	40
Dow	CM-Z-7	2.50 dia x 2.0	1.708	1.74	40
Dow	CM-Z-8	2.50 dia x 2.0	1.695	1.66	36
Dow	CM-Z-9	2.50 dia x 2.0	1.704	1.99	40
Dow	CM-Z-10	2.50 dia x 2.0	1.709	1.89	40
Pactiv Corp	CM-Z-11	2.50 dia x 1.75	1.824	1.56	35
Pactiv Corp	CM-Z-12	2.50 dia x 1.75	1.824	1.59	35
Pactiv Corp	CM-Z-13	2.50 dia x 1.75	1.847	1.83	37
Pactiv Corp	CM-Z-14	2.50 dia x 1.75	1.846	1.69	37

Table 3.3. Summary of XEPS foam material properties

	Owens-Corning		Dow		Pactiv Corp	
	Average	Std. Dev.	Average	Std. Dev.	Average	Std. Dev.
Density (lb/ft^3)	1.507	0.0045	1.705	0.0058	1.835	0.0131
Elastic Modulus (ksi)	1.43	0.12	1.86	0.15	1.67	0.12
Compressive Strength (psi)	32	1	39	2	36	1

3.3 Dynamic Testing of Wall Sections

NCMA proposed five wall sections for full-scale dynamic testing. The first was a control wall which was a fully grouted, single-wythe concrete masonry unit (CMU) wall. Three of the sections consisted of a fully grouted CMU wythe with an exterior brick veneer. The remaining section was a fully grouted, double-wythe CMU wall. The four multi-wythe sections contained a 1-inch air gap and 2 inches of XEPS rigid board insulation between the interior and exterior wythes. Figures 3.8 through 3.12 present the details of each wall section. The sections shown in Figues 3.9 and 3.10, labeled as Wall 2 and Wall 3, are identical in terms of design strength. They differ because Wall 2 is constructed using standard CMUs, whereas Wall 3 is constructed using A-block CMUs. An A-block CMU is simply a standard CMU minus one of the end webs, thus forming an "A" shape. A-block construction allows the reinforcement to be placed early on, and therefore more easily, which reduces construction costs.

The walls were to be constructed such that the interior surface of each wall would be flush with the face of the supporting channel. In typical construction, these types of

walls may be constructed on top of a foundation with the floor slab already cast, or the floor slab may be cast after the walls are finished. In the first case, the reinforcement must carry all the wall shear force, whereas in the latter case the floor slab would substantially increase the wall shear capacity. This issue will be discussed further in the section on full-scale dynamic testing. The following specifications were provided by NCMA.

- Geometry of Walls: 96-in-wide by 128-in-tall for 97-in-wide by 120-in-tall test frame opening

- Concrete Masonry Units: standard 1900-psi lightweight/medium weight (density of 105 pcf) ASTM C 90 units

- Clay Brick: standard 4-inch facing brick ASTM C 216

- Mortar: type S masonry cement mortar per ASTM C 270

- Grout: 3000-psi coarse grout in accordance with ASTM C 476

- Reinforcing Steel: grade 60 No. 4 and No. 5 reinforcement

- Eye and Pintle Ties: W2.8 in accordance with ASTM A 82 and hot dipped galvanized in accordance with ASTM A 153, ties spaced 16 inches on centers horizontally and vertically

- Foam Insulation: rigid closed cell XEPS thermal board insulation complying with ASTM C 578-95 Type X, minimum density of 1.35 pcf, minimum compressive strength of 15 psi (ASTM D 1621-94)

No. 4 (M#13) lifting hooks in end cells (24 in. (610 mm) embedment)

No. 5 (M#16) continuous

Open bottom bond beam unit

No. 5 (M# 16) at 25 in. (635 mm) spliced with vertical reinforcement 3 places

12 in. (305 mm) CMU grouted solid with face shell-thick head joints

9 gage joint reinforcement at 16 in. (406 mm) o.c.

Vertical No. 5 (M#16) in each end cell of panel and one midway between (three total) (bars offset in wall as shown)

No. 5 (M#16) 25 in. (635 mm) welded to steel channel at bottom (3 places) (locate in center of wall)

No. 5 (M#16) continuous

Open bottom bond beam unit

Steel channel section flush CMU with wall this side

3¾ in. (95 mm)

Fig. 3.8. 12-inch, solid-grouted control section (Wall 1)

22

No. 4 (M#13) lifting hooks in end cells (24 in. (610 mm) embedment)

No. 5 (M#16) continuous

Open bottom bond beam unit

2 in. (51 mm) extruded polystyrene rigid board insulation

8 in. (203 mm) CMU grouted solid with face shell-thick head joints

Joint reinforcement/ adjustable tie assembly at 16 in. (406 mm) o.c.

One vertical No. 5 (M#16) in each end cell of panel and one midway between (bars to be centered in CMU wall)

No. 5 (M#16) continuous

Open bottom bond beam unit

Steel channel section flush CMU side of wall

Adjustable ties 16 in. (406 mm) o.c. each way

No. 5 (M# 16) standard hook with 25 in. (635 mm) lap spliced with vertical reinforcement 8 places

4 in. (102 mm) clay facing brick masonry veneer

1 in. (25 mm) air space

No. 5 (M# 16) standard hook with 25 in. (635 mm) lap welded to steel channel at bottom (3 places)

5½ in. (140 mm)

Fig. 3.9. Conventional 110-mph Exposure C veneer section (Wall 2)

23

No. 4 (M#13) lifting hooks in end cells (24 in. (610 mm) embedment)

No. 5 (M#16) continuous

Open bottom bond beam unit

2 in. (51 mm) extruded polystyrene rigid board insulation

8 in. (203 mm) A-block CMU grouted solid

Joint reinforcement/ adjustable tie assembly at 16 in. (406 mm) o.c.

Vertical No. 5 (M#16) in each end cell of panel and one midway between (three total) (bars to be centered in wall)

No. 5 (M#16) continuous

Open bottom bond beam unit

Steel channel section flush CMU side of wall

Adjustable ties 16 in. (406 mm) o.c. each way

No. 5 (M# 16) standard hook with 25 in. (635 mm) lap at each vertical bar

4 in. (102 mm) clay facing brick masonry veneer

1 in. (25 mm) air space

No. 5 (M# 16) standard hook with 25 in. (635 mm) lap welded to steel channel at bottom at ends of panel and near center (3 places)

$5\frac{1}{2}$ in. (140 mm)

Fig. 3.10. A-block section with veneer (Wall 3)

24

No. 4 (M#13) lifting hooks in end cells (24 in. (610 mm) embedment)

No. 4 (M#13) continuous

Open bottom bond beam unit

2 in. (51 mm) extruded polystyrene rigid board insulation

8 in. (203 mm) CMU grouted solid

Joint reinforcement/ adjustable tie assembly at 16 in. (406 mm) o.c.

No. 4 (M#13) at 8 in. (203 mm) o.c. each way

Adjustable ties 16 in. (406 mm) o.c. each way

No. 4 (M# 13) standard hook with 24 in. (610 mm) lap

4 in. (102 mm) clay facing brick masonry veneer

1 in. (25 mm) air space

No. 4 (M# 13) at 24 in. (610 mm) o.c. max with 24 in. (610 mm) lap welded to steel channel

No. 4 (M#13) continuous

Open bottom bond beam unit

Steel channel section flush with CMU side of wall

5½ in. (140 mm)

Fig. 3.11. Prison wall section (Wall 4)

25

No. 4 (M#13) lifting hooks in end cells (24 in. (610 mm) embedment)

2 in. (51 mm) polystyrene rigid board insulation

6 in. (152 mm) CMU each wythe grouted solid and fully mortared head joints

No. 4 (M#13) standard hook with 24 in. (610 mm) lap, each wythe (typ.)

No. 4 (M#13) at 16 in. (406 mm) on center each way for each wythe

Box tie at 16 in. (406 mm) on center

No. 4 (M#13) at 24 in. (610 mm) max. welded to steel channel, each wythe (typ.)

1 in. (25 mm) air space

Steel channel section flush one side of wall

Fig. 3.12. Double-wythe reinforced cavity section (Wall 5)

3.3.1 Wall Construction

The following figures show photographs that were taken during the construction of Walls 1, 2, and 3. These walls were chosen for testing because Walls 2 and 3 are more common in construction and Wall 1 was chosen as the control wall for comparison purposes.

Fig. 3.13. Support channels for walls

Fig. 3.14. Beginning of Wall 1 construction

Fig. 3.15. Layout of blocks

Fig. 3.16. Bond beam before grouting

Fig. 3.17. Wall 2 construction

Fig. 3.18. Wall 2 nearing completion

31

3.3.2 Test Preparation

A prediction analysis was performed to identify an appropriate standoff distance for the first detonation charge. The goal was to locate the charge such that the blast load would significantly damage the wall but would not completely fail it to the extent that no data would be collected. A simplified analysis was performed using software provided by the U.S. Army Corps of Engineers (USACE) Protective Design Center (PDC). A detailed description of the methodology used in the simplified analysis is presented in Chapter 5, which also includes the predicted results for the chosen load cases.

After reviewing the results of the prediction analyses, the engineers on the project selected a charge weight and initial standoff distance for the first detonation. Since Wall 2 was the section considered in the prediction analysis, the first detonation included Wall 2 and Wall 1. The walls tested in the following detonations were then selected: the second detonation included Wall 1 and Wall 3, and the third detonation included Wall 2 and Wall 3.

After preparation of the reaction structure was finished, Wall 1 was moved to the test range using a mobile crane, as shown in Figures 3.19 and 3.20. When it came time to move Wall 2, preventative measures were taken to ensure the safe transport of the wall to the test range. Wooden wedges were driven between the foam and the brick on the exposed sides and top of the walls, as shown in Figure 3.21. Two straps were wrapped around the wall – one at mid-height and one approximately one foot below the top of the wall (Figure 3.22). Wall 2 was then transported in the same fashion as Wall 1 (Figure 3.23).

Fig. 3.19. Transporting Wall 1 to test range

Fig. 3.20. Bringing Wall 1 onto test range

Fig. 3.21. Wooden wedges driven between foam and brick veneer
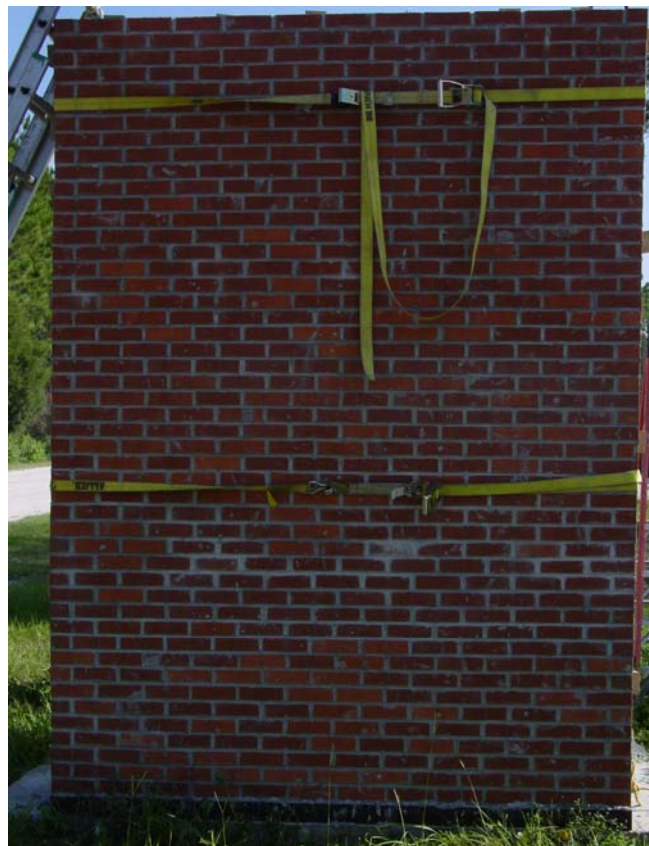
Fig. 3.22. Straps supporting brick veneer

Fig. 3.23. Transporting Wall 2 to test range

Once the walls were on the test range, they had to be placed in the reaction structure. The reaction structure can accommodate 10-ft-, 20-ft-, or 30-ft-tall panels. For testing the shorter panels, large clearing panels are inserted into the front of the reaction structure that block off the top portion. Each clearing panel blocks out a 10-ft-tall section, so for testing 10-ft-tall wall sections, two clearing panels must be inserted. The large height of the reaction structure did not allow the crane to place the walls using the same configuration that was used in transporting the walls. Therefore, the configuration shown in Figure 3.24 was used to place the walls in the reaction structure. A long nylon sling was attached to each lifting point on the top of the wall. The other end of each sling was attached to the hook on the crane. This allowed the crane to boom out far enough so

35

that the hook was above the top of the reaction structure, thus allowing the wall to be

placed appropriately (Figure 3.24).

Fig. 3.24. Placing Wall 2 in reaction structure

At the base of each wall, the interior and exterior sides were supported by pieces of angle iron that were bolted to the floor of the reaction structure. The interior base angle was bolted down with two lines of bolts in standard holes, while the exterior base angle was bolted down with a single line of bolts in slotted holes. This configuration provided a way of allowing rotation so that simple support conditions could be used in the modeling. Figure 3.25 shows one of the interior angles prior to bolting it into place. The top interior side of each wall was supported by the inserted clearing panel. The top exterior of each wall was held in place by a rectangular steel tube. Rounded wooden shims were placed between the tube and the wall in order to apply as little resistance to rotation as possible. Figure 3.26 shows a side view of the exterior top support.

Fig. 3.25. Interior base angle

Fig. 3.26. Top exterior support for Wall 2

After the walls were placed, the final instrumentation was installed. Reflective pressure gauges were installed on the front of the structure, and deflection gauges were attached to the rear side of each wall section. The location of these gauges is shown in Figure 3.27. Figure 3.28 shows an interior view of Wall 2 with the deflection gauges installed. High-speed cameras were placed as shown in Figure 3.29 – one directly behind each wall and one exterior camera at a safe distance from the detonation. Figure 3.30 shows the mounting system used for one of the interior cameras. The exterior camera was positioned so that it could capture a front view of the response, as well as the progression of the shock wave.
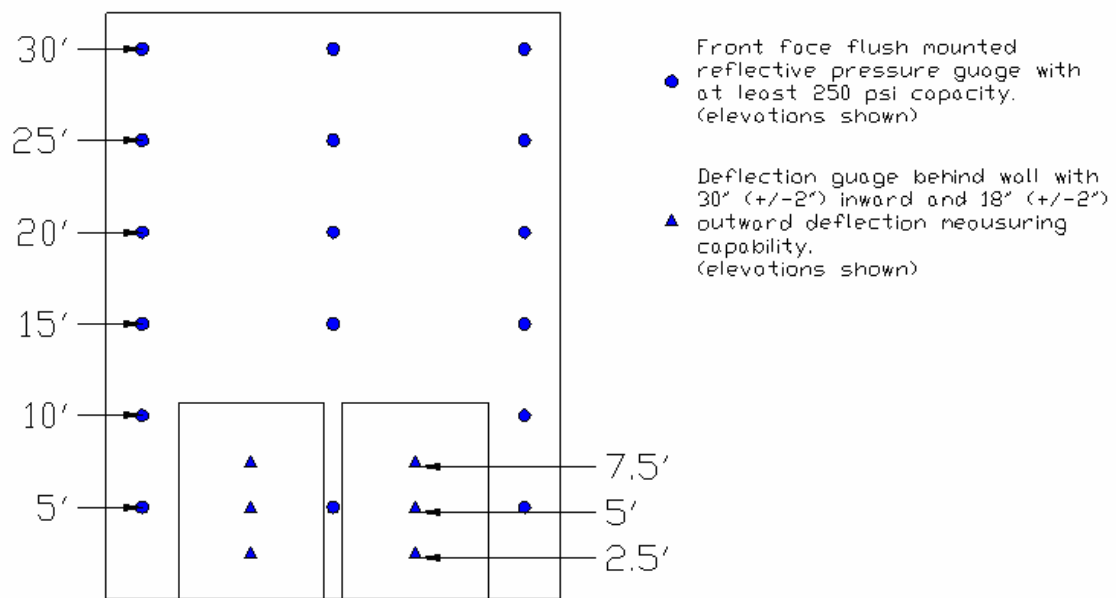
Fig. 3.27. Pressure and deflection gauge locations

Fig. 3.28. Deflection gauges on Wall 2

High Speed (min. 1,000 fps) and Spy Cameras capturing full height and width of each

High Speed (min. 1,000 fps) capturing oblique view of full height and width of the two walls
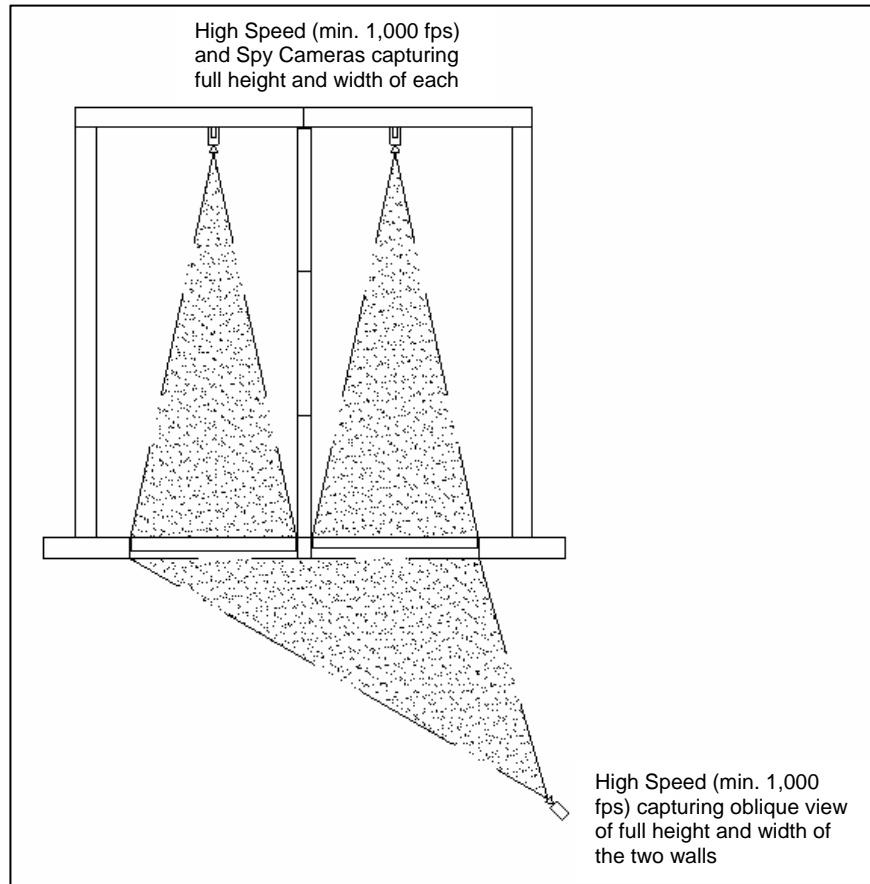
Fig. 3.29. High-speed camera placement

Fig. 3.30. Mounting of an interior camera

On the day of each test, all gauges were checked and the grounds were cleared of loose debris. The location of the charge was then marked, and the explosives were unloaded and placed on an elevated platform. Two views of the structure prior to detonation are shown in Figures 3.31 and 3.32.

Fig. 3.31. Oblique view of walls prior to detonation

Fig. 3.32. Overall oblique view of reaction structure prior to detonation

3.3.3 Dynamic Response of Wall Sections

In this section, the response results of the wall sections are presented for the three detonations. The results include deflection histories along with post-test photographs. Problems encountered during testing and the respective solutions are also described.

3.3.3.1 Detonation 1

During the first test, no gauges were damaged, and the response of both walls yielded useful data. Neither wall was unstable after Detonation 1. Figures 3.33 and 3.34 present the deflection histories of Walls 1 and 2, respectively. Each plot includes the respective quarter points and mid-height deflections.

Figures 3.35 and 3.36 show exterior views of Wall 1 and Wall 2 after Detonation 1, respectively. Figure 3.37 shows a side view of Wall 2 after Detonation 1. There was no indication that the foam made significant contact with the brick. Figure 3.38 and 3.39 show closer views of the interior and exterior sides of Wall 2 after Detonation 1. Notice the horizontal cracks near mid-height, indicating the formation of a plastic hinge.
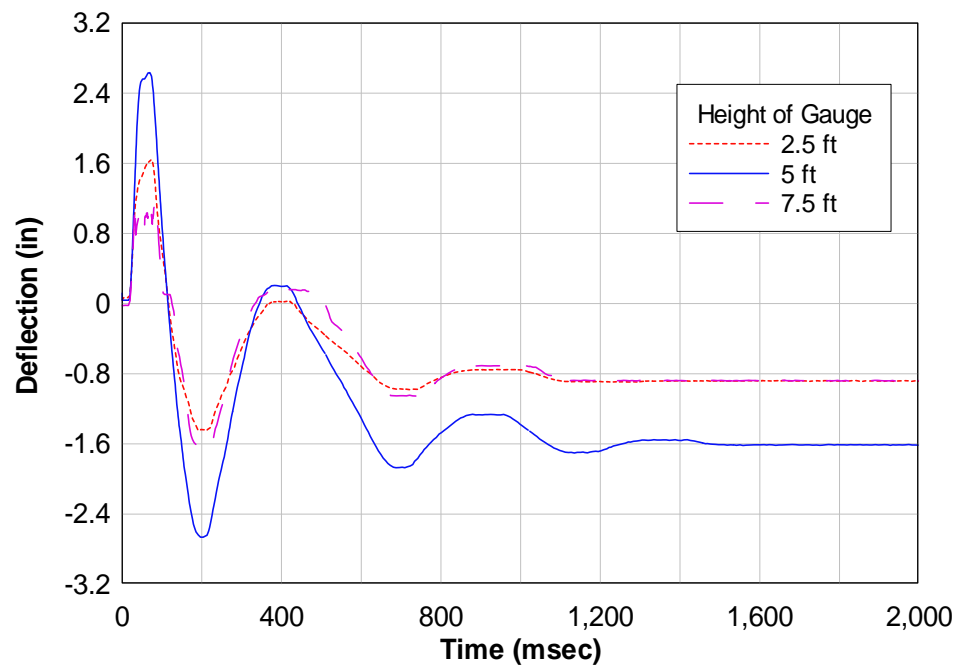
Fig. 3.33. Detonation 1, Wall 1 deflection history
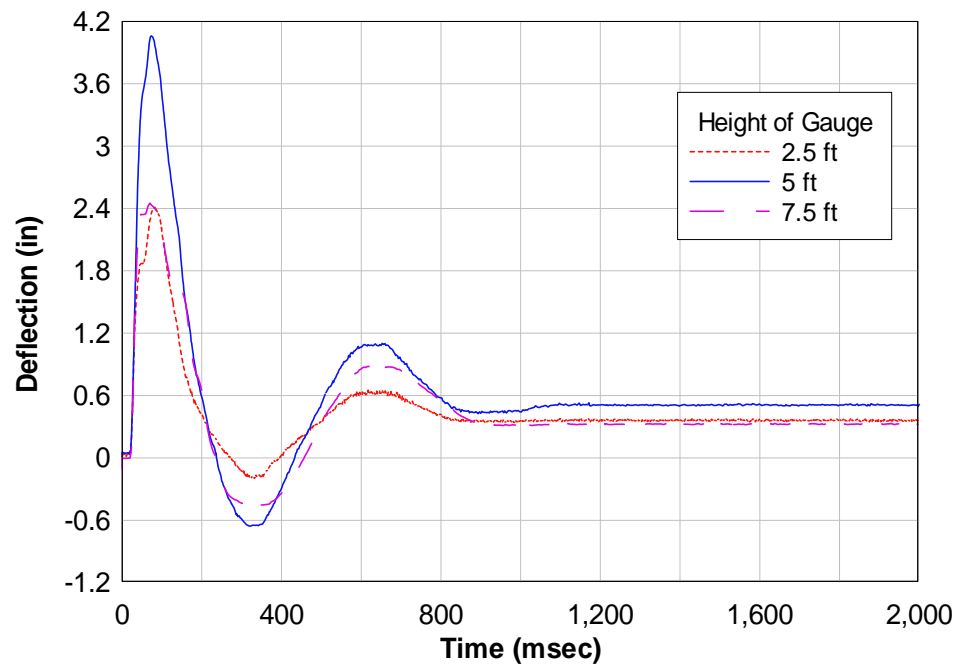
Fig. 3.34. Detonation 1, Wall 2 deflection history

Fig. 3.35. Exterior view of Wall 1 after Detonation 1

44

Fig. 3.36. Exterior view of Wall 2 after Detonation 1

Fig. 3.37. Side view of Wall 2 after Detonation 1

Fig. 3.38. Interior view of Wall 2 after Detonation 1

Fig. 3.39. Close-up exterior view of Wall 2 after Detonation 1

Review of the test results showed that the deflection of Wall 1 was much less than the prediction. Post-test measurement revealed that the vertical reinforcement had been placed closer to the interior side rather than the exterior, thus resulting in a higher moment capacity than specified by the construction details. In order to provide a wall with a similar amount of mass and the same structural capacity as Wall 2, the reinforcement was placed off-center to result in the same effective depth, d. However, the wall was essentially in the frame backwards, resulting in an effective depth approximately twice as large as specified. Figure 3.40 shows the depth of the reinforcement in Wall 1.

Fig. 3.40. Detonation 1, Wall 1 reinforcement location

48

3.3.3.2 Detonation 2

Based on pre-test calculations, the unfactored static shear capacity of the lower connection, consisting of three No. 5 reinforcement dowels welded to the base channel, was 33.5 kips. The dynamic flexural strength of the CMU wythe was calculated based on the equations provided by the methodology manual for SBEDS (USACE PDC 2006). A masonry compressive strength of 2,200 psi was assumed. The dynamic moment capacity of the section was computed to be 262,000 lb-in. A uniformly distributed load resulting in a mid-span moment equal to the flexural capacity, assuming a span of 120 inches, was calculated to be 146 lb/in. This uniform load would result in a base shear of 8.76 kips; only 26% of the capacity of the connection. Therefore, the walls were tested with the bottom support consisting of only the shear capacity of the reinforcement dowels. This was the case for both Detonation 1 and Detonation 2.

In Detonation 2, the charge was moved closer to the walls to increase the reflected pressure and impulse. This resulted in a shear failure of the dowels of both Wall 1 and Wall 3. This connection failure prevented acquisition of any flexural response data. The interaction of the foam between the veneer and CMU wythe was still studied since it could have become loaded prior to failure of the connection. Further discussion of the shear failure can be found in Section 3.3.4. The deflection histories for Wall 1 and Wall 3 are shown in Figures 3.41 and 3.42, respectively.

When the lower supports of Wall 3 failed, the panel shifted such that the vertical sides became wedged against the reaction structure. This resulted in two-way bending. Figures 3.43 and 3.44 show post-test views of Wall 3. Notice the vertical cracks indicating two-way bending and the movement of the entire wall over the base angle.
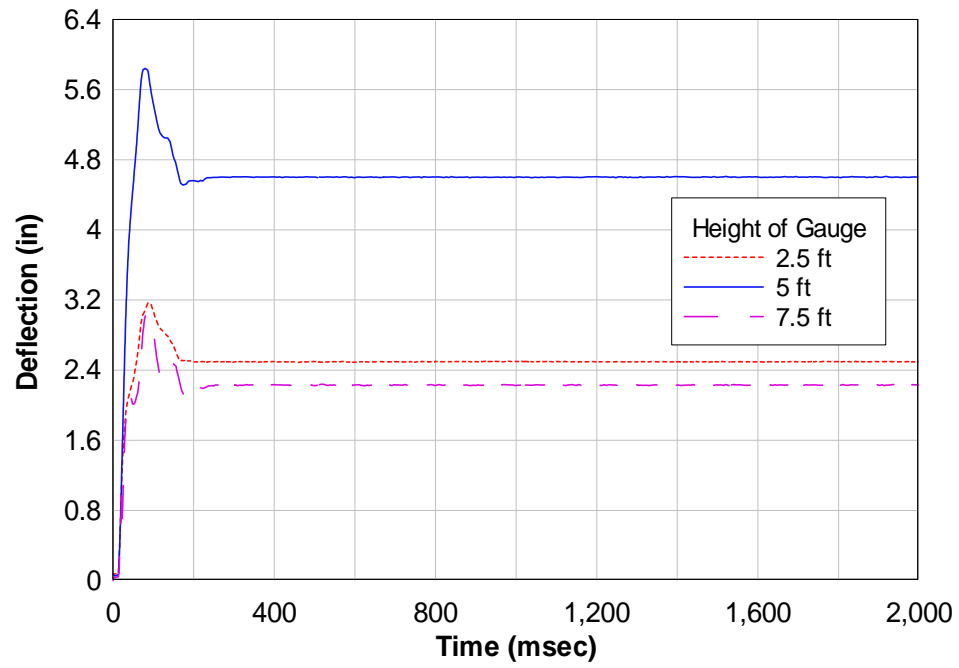
Fig. 3.41. Detonation 2, Wall 1 deflection history
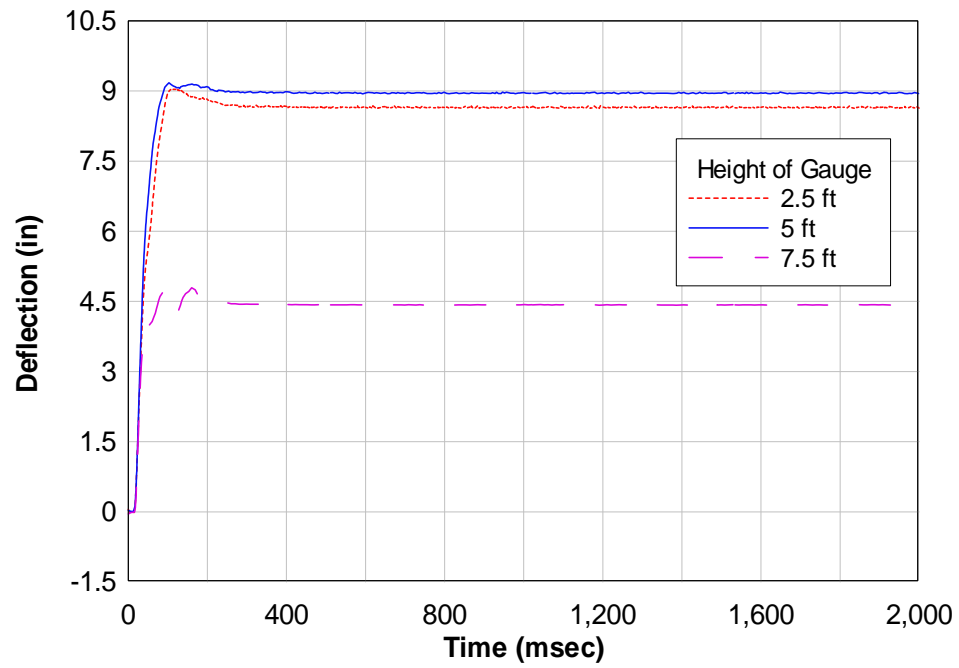
Fig. 3.42. Detonation 2, Wall 3 deflection history

50

Fig. 3.43. Exterior and interior views of Wall 3 after Detonation 2

Fig. 3.44. Bottom support failure of Wall 3 in Detonation 2

When the lower supports of Wall 1 failed, unlike Wall 3, the wall did not shift within the reaction structure. Therefore, Wall 1 did not show signs of two-way bending, but did have the expected plastic hinge just above mid-height. It is believed that the supports failed early in the response due to the extremely high shear forces that are caused by the peak reflected pressure. Figure 3.45 shows an exterior and an interior view of Wall 1 after Detonation 2.

Fig. 3.45. Exterior and interior views of Wall 1 after Detonation 2

3.3.3.3 Detonation 3

After the connection failure in Detonation 2, the lower supports were strengthened before proceeding with Detonation 3. The height of the vertical leg of the interior base angle was increased so that the shear would occur through the masonry rather than at the interface between the masonry and the steel channel where only the welded dowels were available to take the shear. Steel plate was welded to the base angle to make it taller, as shown in Figure 3.46. This modification provided adequate support for Detonation 3.

Fig. 3.46. Modification of base support for Detonation 3

In Detonation 3 the charge was once again moved closer, providing the highest threat of any of the detonations. Large deflections occurred in both Wall 2 and Wall 3; however, there was no indication that the foam ever came into contact with the brick veneer. The deflection of Wall 3 was less in Detonation 3 than it was in Detonation 2; however, that was simply due to the support failure in Detonation 2. Although the connection used in Detonations 1 and 2 rarely occurs in masonry construction, the failure

in Detonation 2 does emphasize the importance of adequate connections. The deflection histories of Wall 2 and Wall 3 are presented in Figures 3.47 and 3.48, respectively.

In Detonation 3, both wall responses resembled a typical flexural response. There was much more cracking prevalent in the brick veneers after this detonation, as can be seen in Figures 3.49 through 3.51. Interior post-test views of the walls are shown in Figures 3.52 through 3.54.
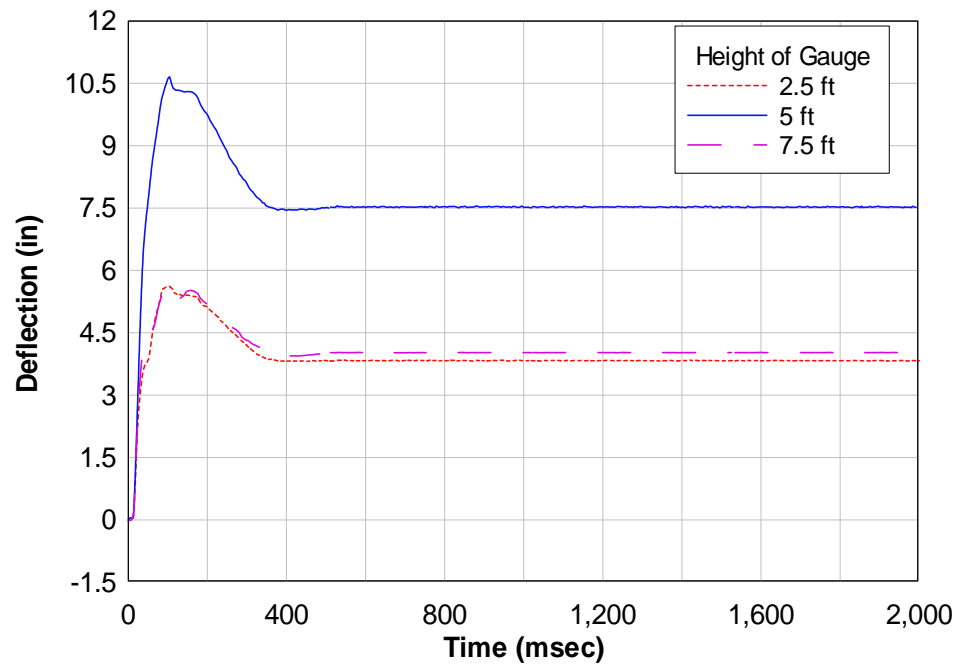
Fig. 3.47. Detonation 3, Wall 2 deflection history
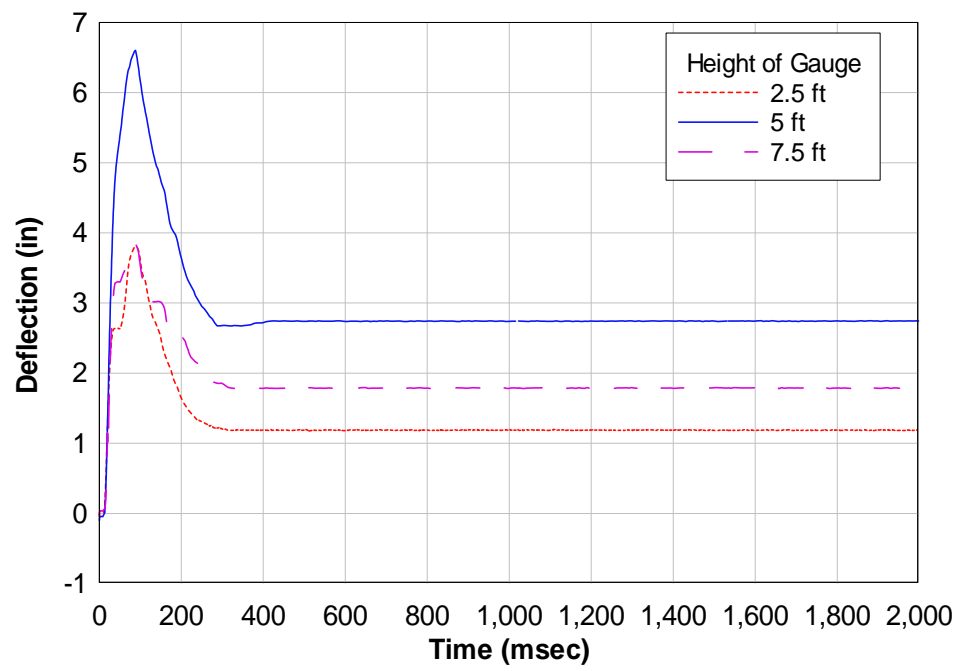
Fig. 3.48. Detonation 3, Wall 3 deflection history

Fig. 3.49. Exterior view of Wall 2 after Detonation 3

Fig. 3.50. Exterior view of Wall 3 after Detonation 3

Fig. 3.51. Side view of Wall 2 after Detonation 3

Fig. 3.52. Interior view of Wall 2 after Detonation 3

Fig. 3.53. Base angle after Detonation 3

Fig. 3.54. Interior view of Wall 3 after Detonation 3

3.3.4 Forensics

After each test was completed, the damaged wall sections were moved to a
location where forensic analysis could be safely performed. Some of the walls received
more damage during removal than during the actual testing. This was primarily true of
Wall 3 after Detonation 2 because the brick veneer began to fall off when the wall was
lifted out of the test bay. This also happened to the Detonation 3 walls, although not to
the same extent; there was still enough brick on these walls to be representative of the
response.

The location of the reinforcement was verified in each section. It was found that
the reinforcement in Wall 1, Detonation 1 was deeper (farther from the exterior face) than
the reinforcement in Wall 1, Detonation 2. The center reinforcement for Wall 1,

Detonation 1 was never located due to disassembly difficulties. It was deemed less

critical once the reinforcement depth on the sides was known. The following table shows

the depths of the reinforcement, measured from the exterior face, for Wall 1 in

Detonations 1 and 2.

Table 3.4. Wall 1 reinforcement depths* (in)

Placement	Detonation 1	Detonation 2
Left	7.5625	3.625
Center	n/a	3.1875
Right	6.375	3.875

*measured to the nearest 1/16 of an inch

Because of the variances in reinforcement depth in Wall 1, the reinforcement

depths in the other walls were also checked. The reinforcement depths for Wall 2 and

Wall 3, measured from the exterior face of the CMU wythe, are presented in Table 3.5

and Table 3.6, respectively. Although the reinforcement depths for Walls 2 and 3 were

not uniform, the deviations are less than those for Wall 1.

Table 3.5. Wall 2 reinforcement depths* (in)

Placement	Detonation 1	Detonation 3
Left	4.4375	3.1875
Center	3.5625	3.5625
Right	3.9375	3.0625

*measured to the nearest 1/16 of an inch

Table 3.6. Wall 3 reinforcement depths* (in)

Placement	Detonation 2	Detonation 3
Left	3.8125	3.8125
Center	4.5625	4.1875
Right	4.1875	4

*measured to the nearest 1/16 of an inch

In all the brick veneer wall sections, there was no indication of global crushing of the foam. There was evidence of minor local damage caused by penetration of the mortar overhangs. The local damage would not have been as noticeable if more care had been taken during construction to keep the back of the brick veneer clean. However, if this had been done it would not have been as representative of typical construction methods.

Based on post-test observations, the blast pressure instantaneously loaded the structural CMU wythe of each wall section. Therefore, the timing of the deflection of the two walls in each detonation should be almost identical if this was the case. A pair of mid-point deflection histories is shown in each of the following three figures. Observation of the following figures reveals that Walls 2 and 3 had a slower initial response than Wall 1 in Detonations 1 and 2, but in Detonation 3 the timing of the response of Walls 2 and 3 was essentially the same. The differences noticed in the first two detonations are small. This response indicates that the foam did not receive significant load, and that the load traveled through the brick, then through the metal ties, and finally into the CMU wythe. Because of the stiffness of the connections between these components, the shock from the blast would propagate through the system very quickly. Conversely, if the load had been transmitted through the foam, then a delayed response should have been much more pronounced. A calculation was performed to show that the metal ties were capable of transferring the entire load to the CMU wythe. This calculation can be found in Section 5.7.
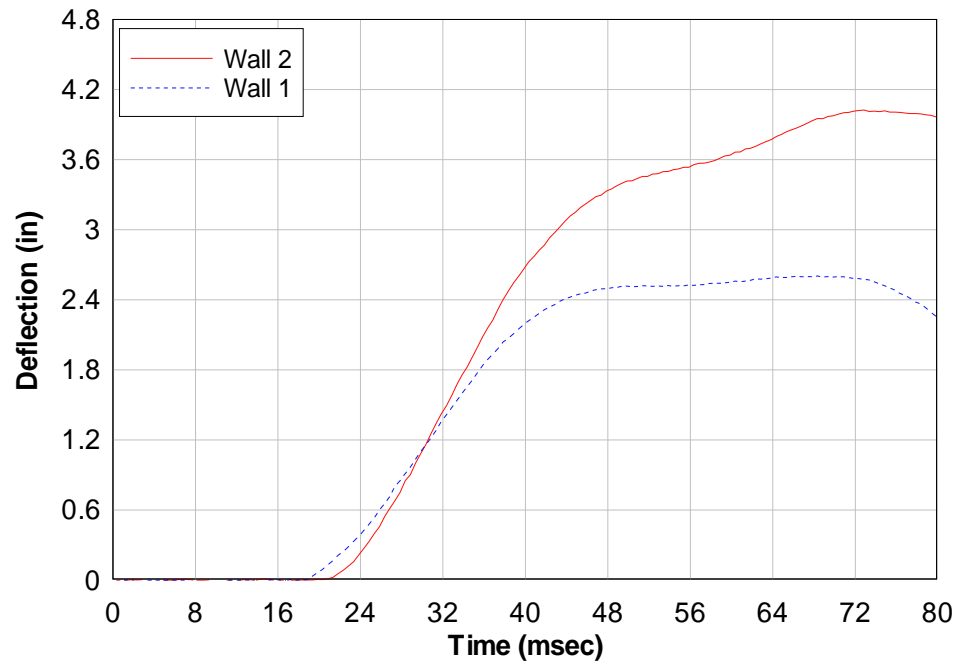
Fig. 3.55. Detonation 1 midpoint deflection comparison
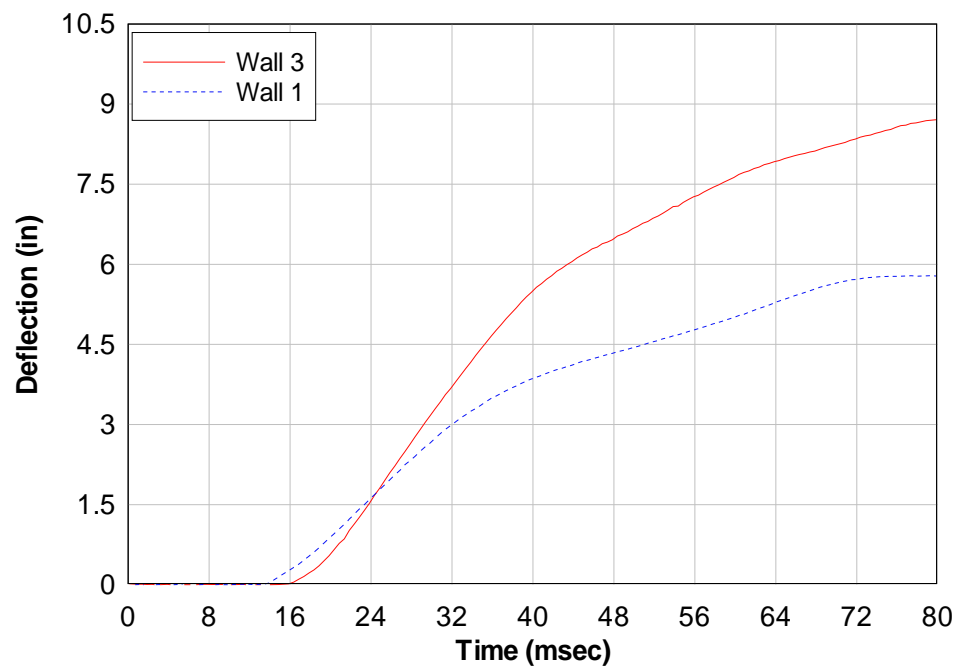
Fig. 3.56. Detonation 2 midpoint deflection comparison
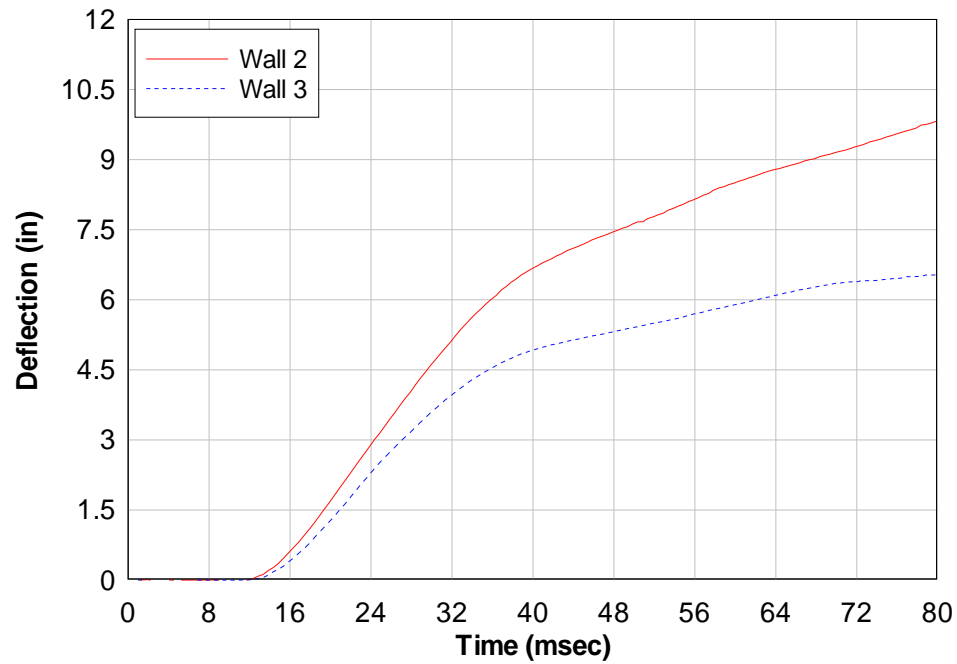
Fig. 3.57. Detonation 3 midpoint deflection comparison

3.3.5 Reflected Pressure Results

In this section, the reflected pressure histories collected during each detonation are presented, along with the respective impulses. Some of these pressure histories were used as load input for modeling purposes; more details about this procedure can be found in Chapter 5. As previously described in Figure 3.27, reflective pressures were recorded on the right and left sides and in the center of the front face of the reaction structure at a height of 5 ft off the ground. The impulse was then obtained by integrating the pressure with respect to time. The following figures present the pressures and impulses for each detonation. Pressure in the center for Detonations 2 and 3 was not recorded due to damage of the gauge during Detonation 2.
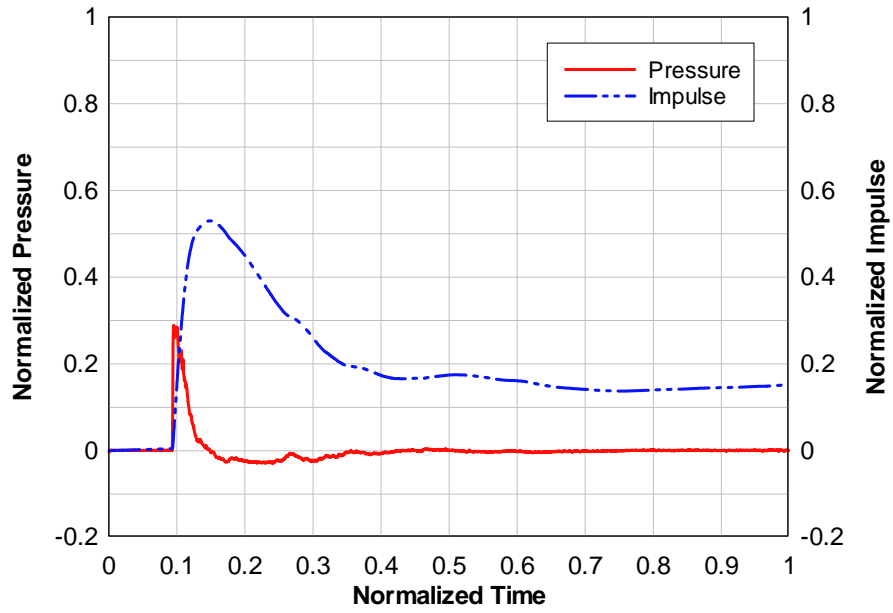
Fig. 3.58. Pressure and impulse on left side for Detonation 1
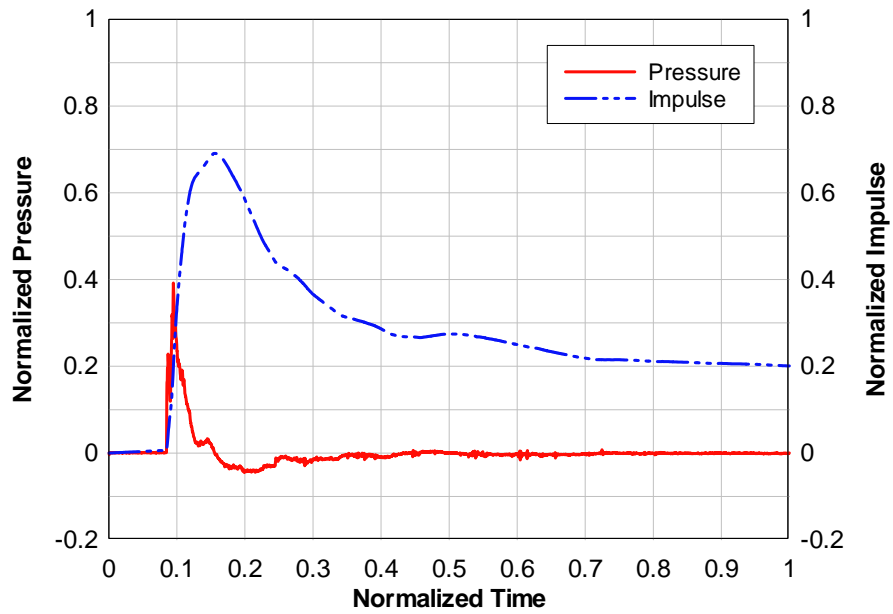
Fig. 3.59. Pressure and impulse in center for Detonation 1
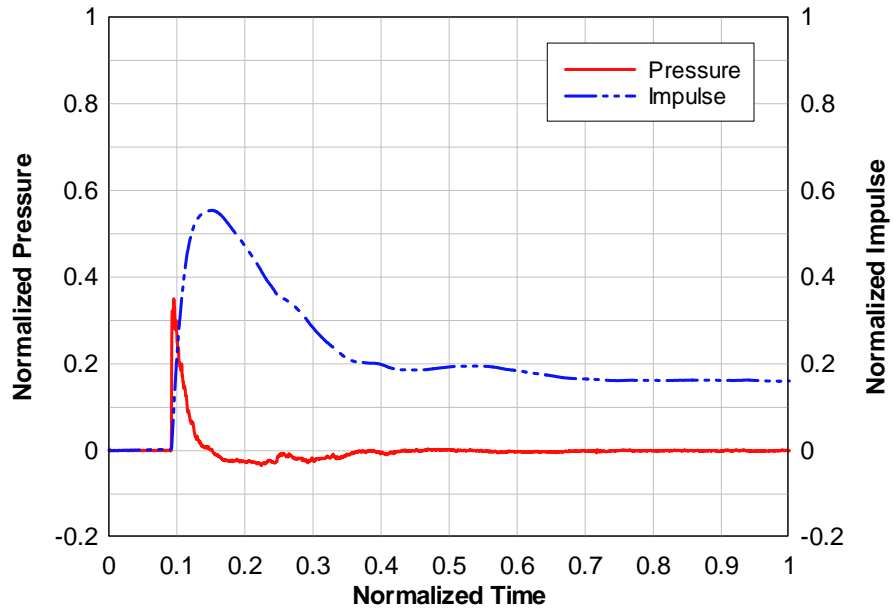
Fig. 3.60. Pressure and impulse on right side for Detonation 1
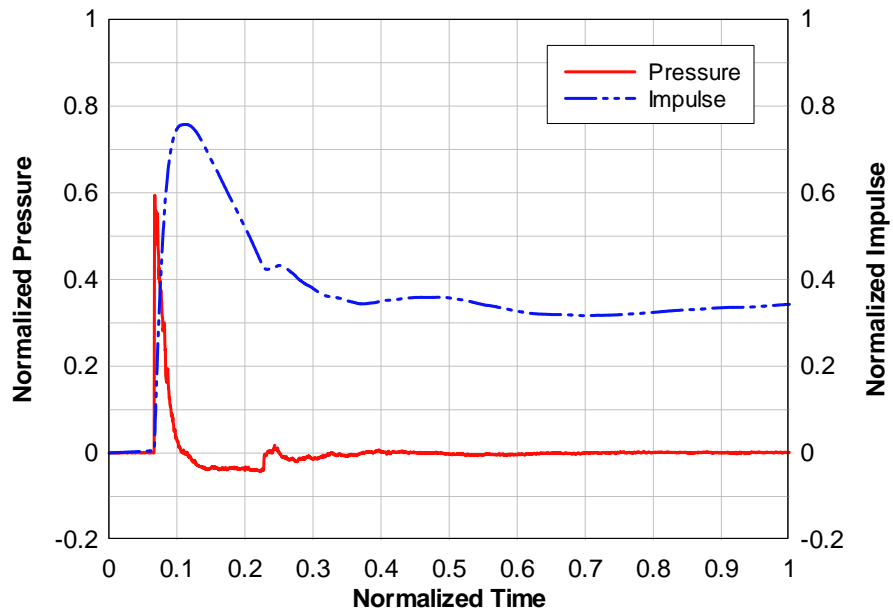
Fig. 3.61. Pressure and impulse on left side for Detonation 2

66
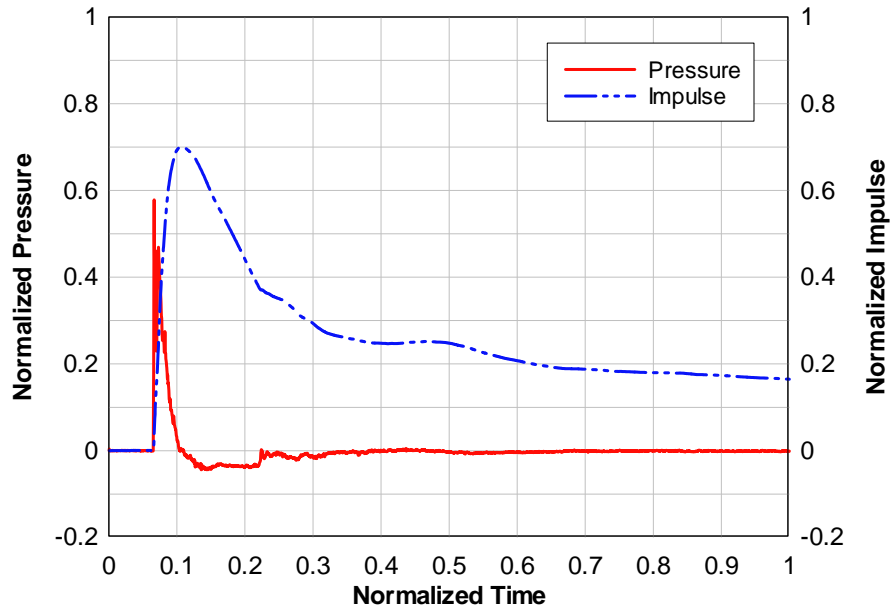
Fig. 3.62. Pressure and impulse on right side for Detonation 2
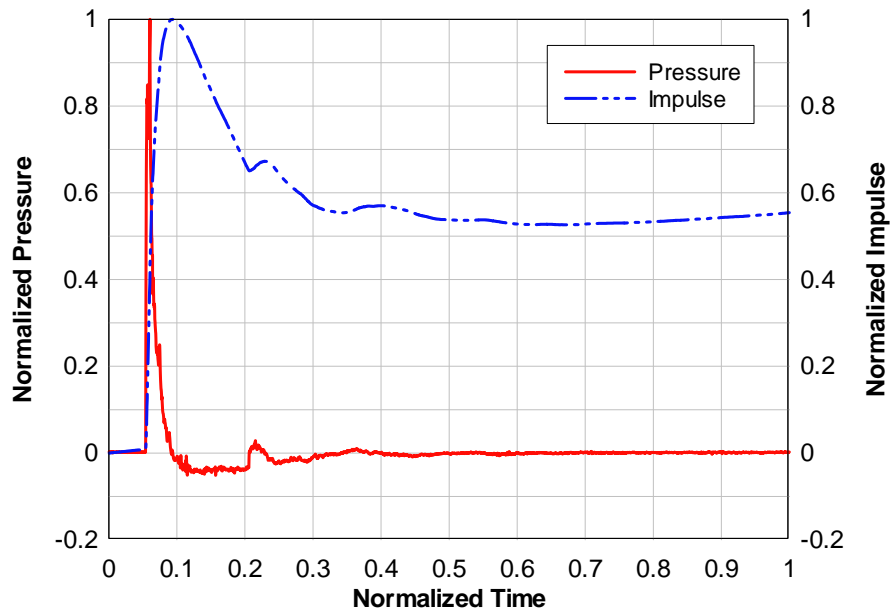
Fig. 3.63. Pressure and impulse on left side for Detonation 3

67
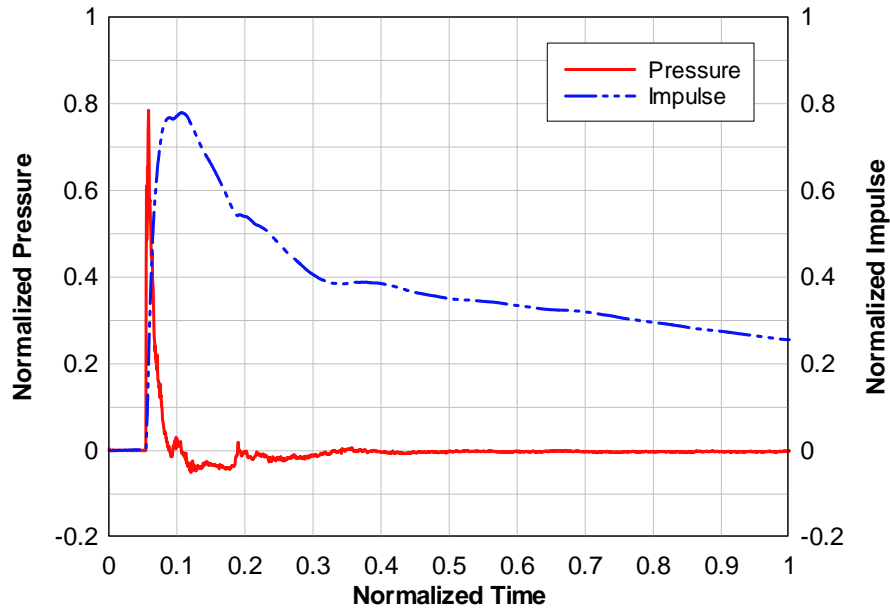
Fig. 3.64. Pressure and impulse on right side for Detonation 3

The percent difference between peak pressure on the right and left (with the right side taken as the basis for comparison) for Detonations 1, 2 and 3 was 17.3%, -2.9%, and -27.4%, respectively. Note that, the higher pressure observed on the left in Detonation 3 corresponds with the larger deflection recorded for Wall 2.

The ConWep weapons effect program was used to estimate the predicted peak pressure and impulse distributions for each detonation; these distributions are shown in Figures 3.65 through 3.70. The predicted values were then compared to the peak values recorded during testing. Comparisons for Detonations 1, 2, and 3 are presented in Tables 3.7, 3.8, and 3.9, respectively.
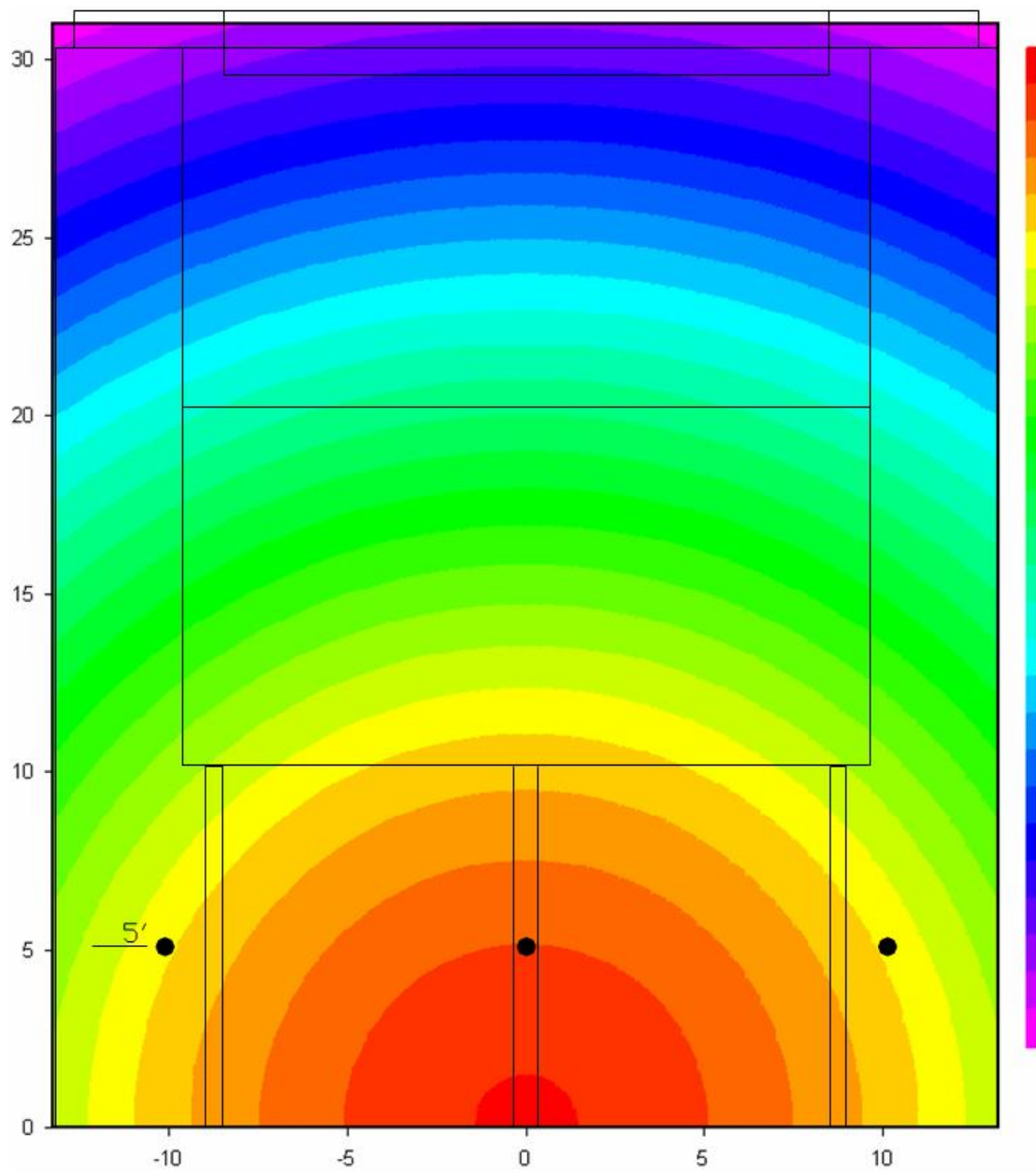
Fig. 3.65. ConWep peak pressure distribution for Detonation 1
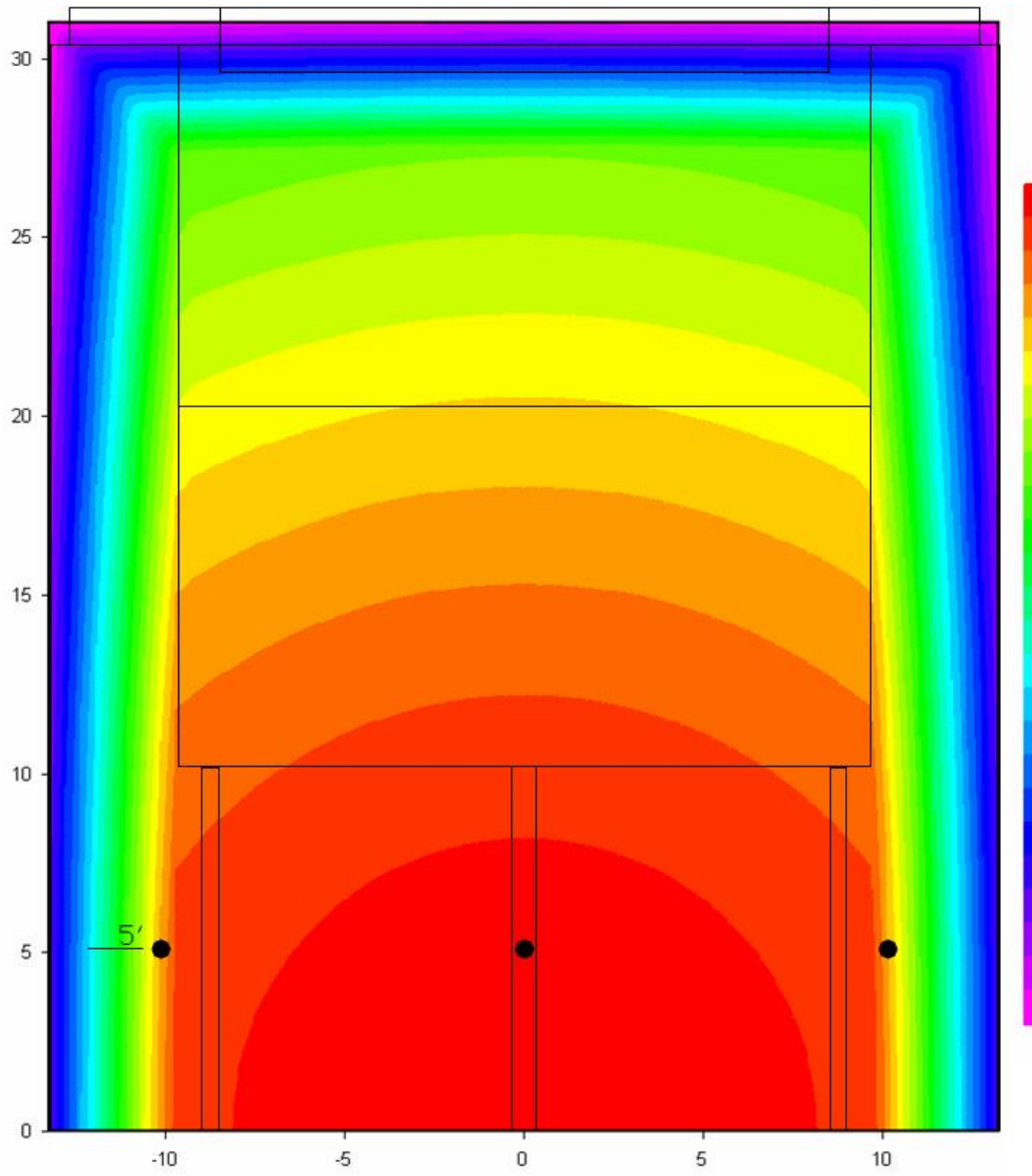
Fig. 3.66. ConWep peak impulse distribution for Detonation 1
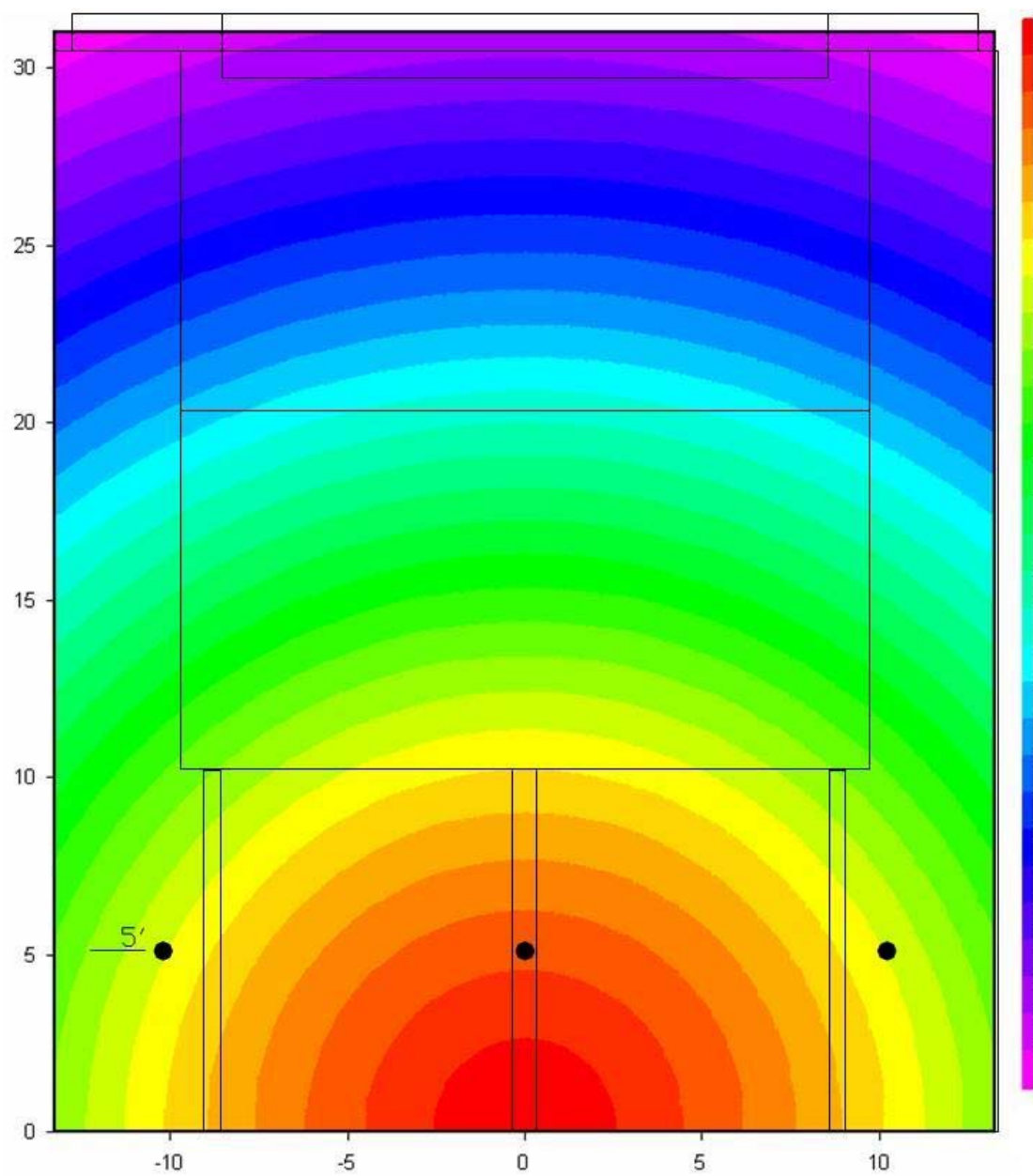
Fig. 3.67. ConWep peak pressure distribution for Detonation 2
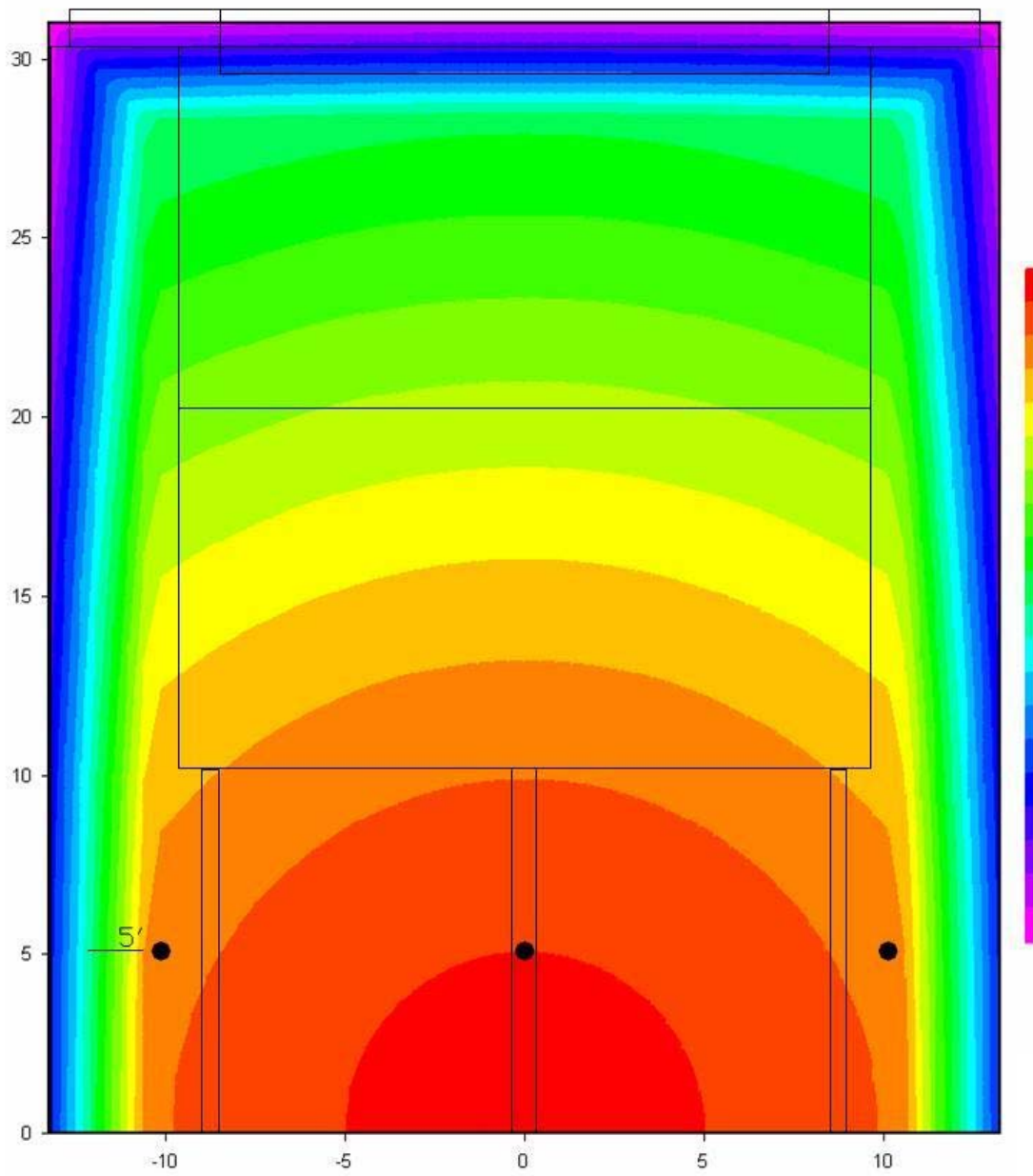
Fig. 3.68. ConWep peak impulse distribution for Detonation 2
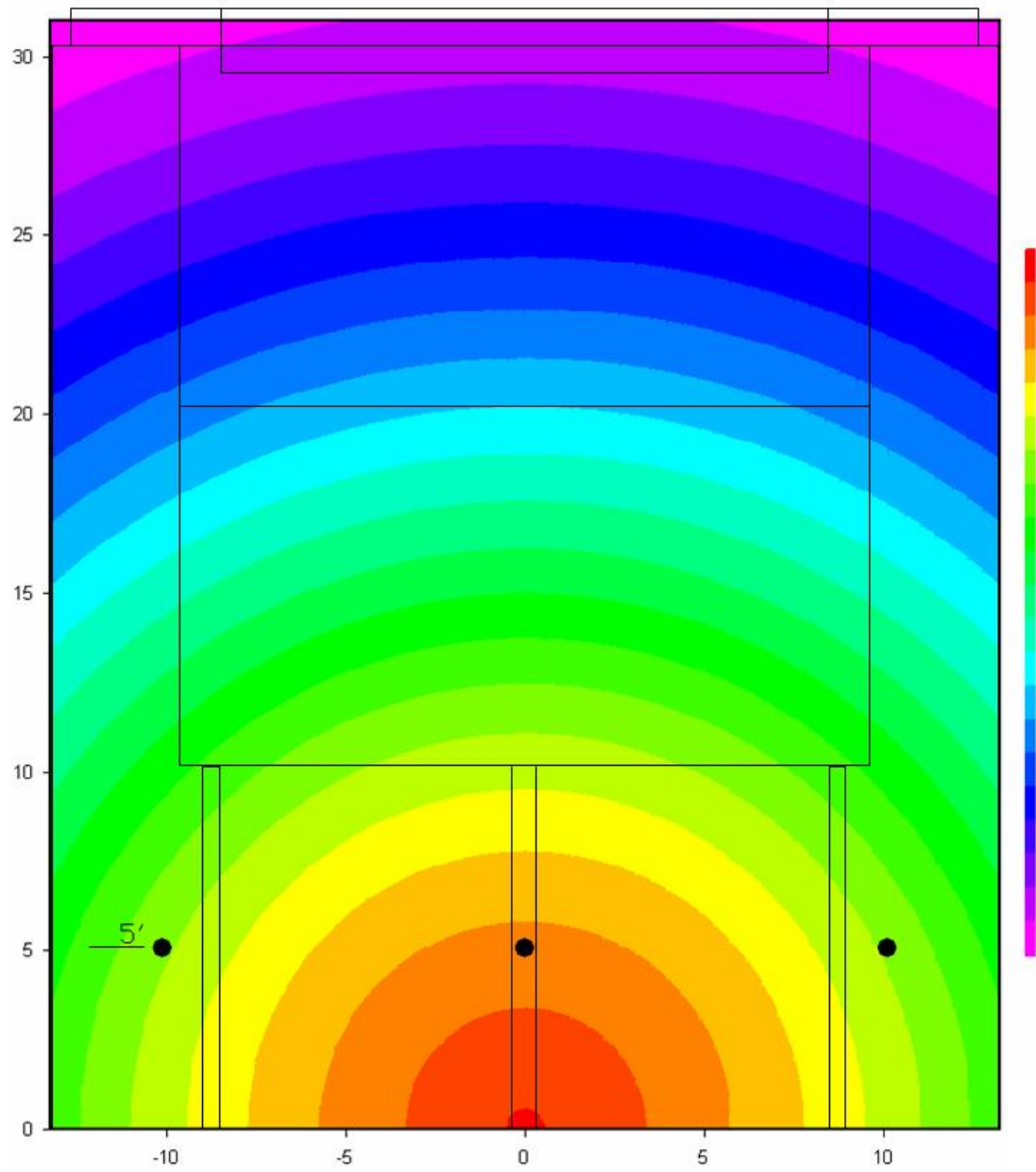
Fig. 3.69. ConWep peak pressure distribution for Detonation 3
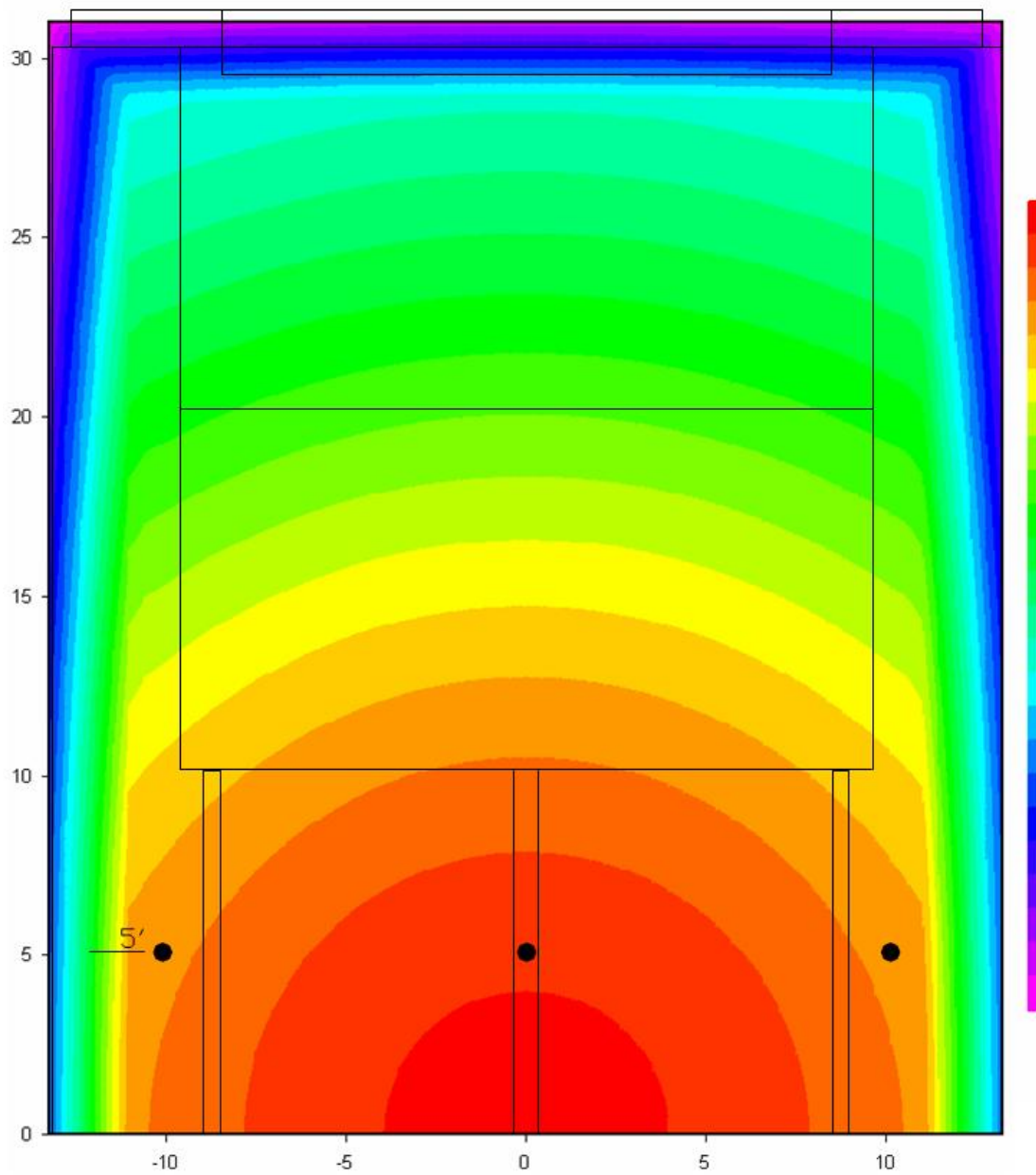
Fig. 3.70. ConWep peak impulse distribution for Detonation 3

74

Table 3.7. Comparison of test data to ConWep prediction for Detonation 1

Gauge	Peak Pressure Percent Difference	Peak Impulse Percent Difference
Left	-26.1%	-16.4%
Center	-3.9%	-0.6%
Right	-10.6%	-12.6%

Table 3.8. Comparison of test data to ConWep prediction for Detonation 2

Gauge	Peak Pressure Percent Difference	Peak Impulse Percent Difference
Left	-5.4%	-6.7%
Center	-	-
Right	-7.9%	-14%

Table 3.9. Comparison of test data to ConWep prediction for Detonation 3

Gauge	Peak Pressure Percent Difference	Peak Impulse Percent Difference
Left	10.6%	6.2%
Center	-	-
Right	-13.1%	-17.2%

Tables 3.7 and 3.8 show that ConWep provided conservative predictions for
Detonations 1 and 2 by predicting higher pressures than those seen in the tests. In
Detonation 3, however, the pressure recorded on the left side was higher than the
ConWep prediction while on the right side it was lower than ConWep. This suggests that
Detonation 3 produced an uneven pressure distribution with higher pressure on the left
side of the reaction structure. This would explain the significant difference in deflection
response between Wall 2 and Wall 3 that was seen in Detonation 3.

CHAPTER 4

FINITE ELEMENT MODELS

4.1 Overview

Because of the nonlinearity of the system under consideration, this project was

well suited for the application of advanced finite element (FE) modeling. FE models are

not easily created, and, in many cases, can be expensive to verify. However, once a

model has been validated by testing, it becomes extremely valuable to the analyst. FE

models can be used to vary many different parameters that would be too expensive to test

in reality.

For this project, FE models were created using the pre-processor HyperMesh that

is part of the HyperWorks suite distributed by Altair Engineering, Inc. Altair's

HyperView was used for post-processing the results of each model. The FE solver LS-

DYNA was used to analyze the models. LS-DYNA is an advanced general-purpose

nonlinear FE program that is capable of solving complex dynamic mechanics problems.

The following sections present the details of the models, along with the respective results.

4.2 Unit System

The U.S. customary unit system was implemented. Table 4.1 shows the units

used for all of the models. Note that while seconds were used as the measure of time in

the FE models, many of the results will be shown in terms of milliseconds (msec) as this is more commonly used for impulse loads.

Table 4.1. Unit system

Property	Measurement Unit
Time	second (s)
Length	inch (in)
Force	pound (lbf)
Velocity	in/s
Mass	$\text{lbf-s}^2/\text{in}$
Stress	lbf/in^2 (psi)
Energy	lbf-in

4.3 Model Geometry

Methodology was developed based on Wall 2. The methodology presented here also applies to Wall 3 because no distinction is made between conventional concrete masonry units (CMUs) and A-block CMUs. Wall 2 was chosen as the modeling focus because it was included in the full-scale dynamic tests and is representative of a common section used in construction. The geometric details of each component for Wall 2 are described in the following section.

4.3.1 Wall 2 – CMU and Grout

The CMUs used in Wall 2 were standard double-corner 8-inch blocks (actual thickness of 7.625 inches) grouted solid with head joints mortared to the thickness of the face shells. The wall was 96 inches wide by 128 inches tall. The vertical reinforcement was spaced at 48 inches on center on one side and 40 inches on center on the other side. This placed vertical reinforcing steel on the left side, the right side, and in the

approximate center of the wall. For modeling purposes, a strip of wall was analyzed

assuming a 48 inch tributary width. The model dimensions of the wall were then 48

inches wide, by 128 inches tall, by 7.625 inches thick. The bond between the grout and

the CMUs was assumed to be perfect; therefore, the grout and CMUs were modeled as a

single unit. This simplified the system and allowed it to be treated as a reinforced

concrete slab. Discussion of the material properties of the CMU wythe can be found in

Section 4.4.

4.3.2 Wall 2 – Reinforcement

Because the horizontal reinforcement in simply supported masonry panel walls

plays only a small part in the resistance to out-of-plane bending, no horizontal

reinforcement was included in the model. Wall 2 has only three pieces of vertical

reinforcement that are continuous for the entire height of the wall with each piece located

at mid-depth of the wall. The other vertical reinforcing steel, that did not extend over the

entire height of the wall, is located 5½ inches from the interior face of the CMU wythe,

giving it a d value of 2.125 inches. Because this reinforcement is close to the

compression face, it does not contribute significantly to the flexural capacity of the wall.

It also has little effect on the inelastic response since it is not present in the hinging

region (mid-span). Therefore, the discontinuous vertical reinforcement was not included

in the FE model. With the wall modeled as a 48-inch-wide strip, a single piece of vertical

reinforcement was placed at the centroid of the cross-section. The vertical reinforcement

was specified as Grade 60, No. 5 reinforcement, with a cross-sectional area of 0.31 in^2.

4.3.3 Wall 2 – XEPS Foam Insulation

The insulation used during construction was manufactured by Dow and is commonly referred to as blue board insulation. The dimensions of the foam in the full-scale dynamic tests were 96 inches wide, by 128 inches tall, by 2 inches thick. To study the effect of thickness on the resistance of the foam, three separate FE models were created. These models represented wall sections containing foam insulation with thicknesses of 2 inches, 4 inches, or 8 inches. These values were chosen so that the thicknesses remained practical with respect to testing, while also providing a range broad enough that potential behavioral patterns could be identified.

4.3.4 Wall 2 – Brick Veneer and Mortar

In blast design, the primary benefit of a brick veneer is that it adds significant mass to the system. For this system, it was hypothesized that upon being subjected to an impulse load, the brick would be given a momentum and would impact the foam insulation, thus imparting the momentum to the resisting structure. Due to the presence of the ties, it was assumed that the brick would not rebound off of the foam but would, essentially, stay in contact with the foam. Because an unreinforced veneer will crack at the bed joints under very low lateral pressures, it was assumed that the flexural stiffness provided by the veneer was negligible. Therefore, the brick veneer was included as non-structural mass by adding mass to the exterior nodes of the foam. The nominal thickness of a brick is 4 inches and the brick veneer in the model covered a surface area with dimensions 48 inches wide by 128 inches tall. Using the density of the brick along with

these dimensions, the necessary nodal mass was calculated and applied to the respective

nodes.

4.3.5 Wall 2 – Supports and Constraints

Regardless of the support condition specified in practice, simple supports result in

the greatest deflection. The constraints provided by the reaction structure (described in

Chapter 3) ensured that the wall was stable and would not fall out of the reaction

structure upon rebound. The constraints were also configured so that rotation was

allowed at the top and bottom of the wall. The boundary conditions for the FE model

were to allow free rotation at both ends. To ensure this, no supports were placed on the

exterior side of the model, which was acceptable since the primary focus was to predict

maximum deflection, and there was no need for the rebound response. The supports in

the FE model were comprised of rigid plates at the top and bottom, respectively, as

shown in Fig. 4.1. The plates were positioned so that a 0.05-inch crack existed between

the plate and interior surface of the CMU wythe. Each plate was 0.25 inch thick and 2

inches tall, providing a clear span of 124 inches. The actual clear span used in testing

was approximately 116 inches. This resulted in the FE model being slightly more

flexible due to a larger clear span.
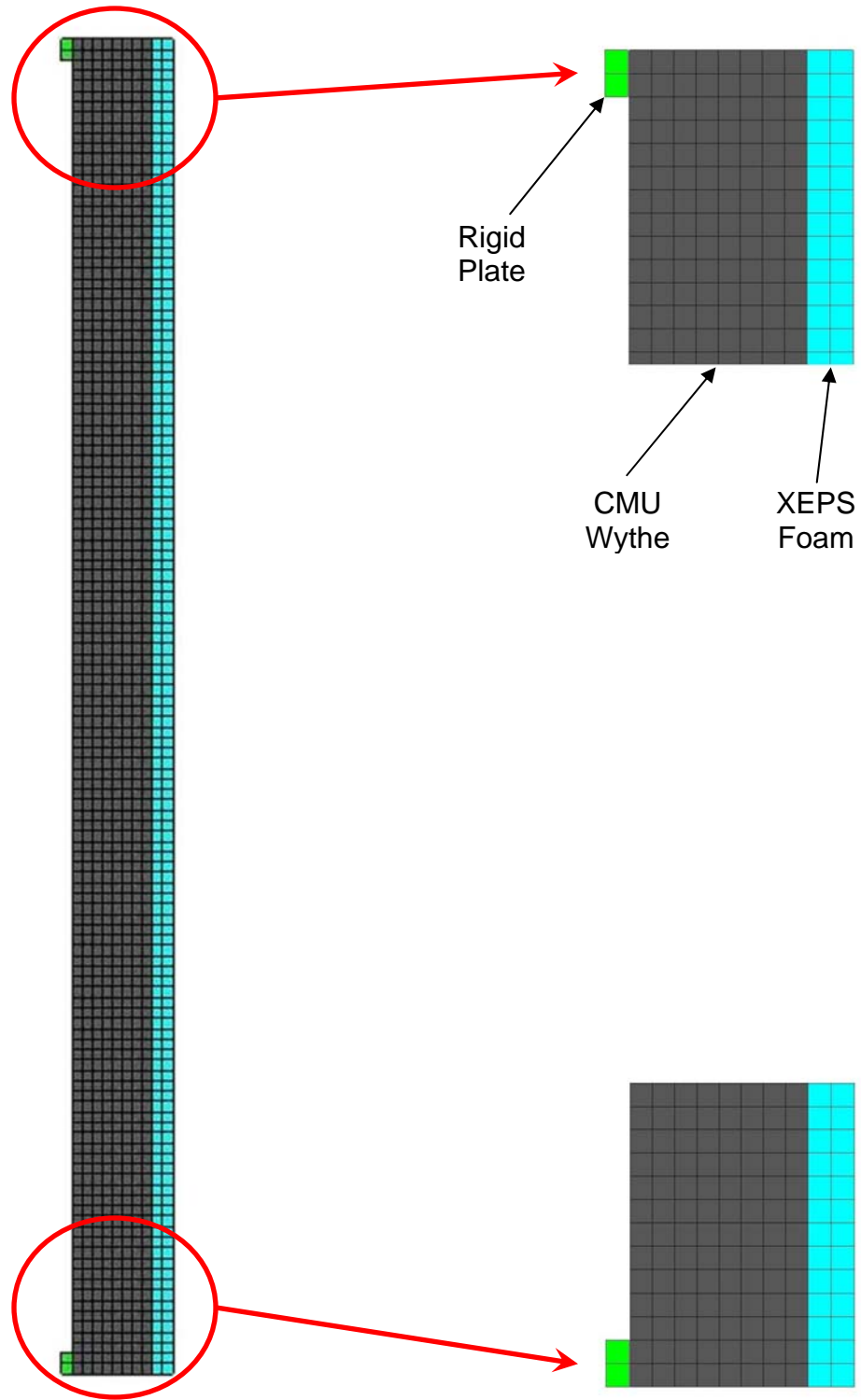
Fig. 4.1. Boundary conditions for finite element models

4.4 Material Modeling

LS-DYNA has a variety of material cards that can be used to model a vast array of materials. The material cards used for this project were known to have produced favorable results for recent similar work. This section describes the material cards chosen for each respective material.

4.4.1 Boundary Material

The material used to model the support plates was a perfectly rigid material model. This prevented the boundaries from being subject to stress and strain. LS-DYNA material #20, *MAT RIGID, is a material card specifically formulated to model materials that are assumed to be rigid. The card also allows any combination of the global degrees of freedom of the material to be fixed. In this way, the plates were constrained from all translations as well as rotations. The following display shows the input for the *MAT RIGID card for the rigid plate supports:

```
*MAT_RIGID_TITLE
BOUNDARY_20
$       MID        RO         E        PR         N     COUPLE         M       ALIAS
          5 0.0007339  3.00E+07      0.30       0.0       0.0       0.0
$       CMO       CON1      CON2
          1.0       7.0       7.0
$LCO_OR_A1        A2        A3        V1        V2        V3
          0.0       0.0       0.0       0.0       0.0       0.0
```

where RO = mass density, E = Young's modulus, PR = Poisson's ratio, N = MADYMO3D 5.4 (not CAL3D) coupling flag, COUPLE = coupling option if applicable, M = MADYMO3D 5.4 / CAL3D coupling option, ALIAS = VDA surface alias name, CMO = center of mass constraint option, CON1 = first constraint parameter, CON2 =

82

second constraint parameter, LCO = local coordinate system number for output, and A1 –

V3 = alternative method for specifying local system (N/A).

4.4.2 Reinforcing Steel

The reinforcing steel was assumed to behave as a linear-elastic-perfectly-plastic

material. This behavior was modeled using LS-DYNA material #3, *MAT PLASTIC

KINEMATIC, which is capable of modeling isotropic and kinematic hardening plasticity.

The density of the reinforcement was 490 lb/ft^3, the modulus of elasticity was 29,000,000

psi, Poisson's ratio was 0.29, and the yield stress was 60,000 psi. The following shows

the input for the *MAT PLASTIC KINEMATIC card for steel:

```
*MAT_PLASTIC_KINEMATIC_TITLE
STEEL_3
$      MID         RO          E         PR       SIGY       ETAN       BETA
         2  0.0007339   2.90E+07       0.29    60000.0        0.0        0.0
$      SRC        SRP         FS         VP
       0.0        0.0        0.0        0.0
```

where RO = mass density, E = Young's modulus, PR = Poisson's ratio, SIGY = yield

stress, ETAN = tangent modulus, BETA = hardening parameter, SRC = strain rate

parameter C, SRP = strain rate parameter P, FS = failure strain for eroding elements, and

VP = formulation for rate effects. Notice that the value for ETAN (the slope of the

stress-strain curve after yield) is set equal to zero, which causes the material to behave as

a linear-elastic-perfectly-plastic material.

4.4.3 Concrete

LS-DYNA material #96, *MAT BRITTLE DAMAGE, was selected as the material card for concrete. This material card is an anisotropic brittle damage model that produces smeared cracks due to tensile loading. Tensile and shear strengths are progressively decreased across the smeared cracks. It also includes the option of accounting for reinforcement via area percentages. This option was not used because the reinforcement was modeled explicitly using beam elements. There are several material cards available in LS-DYNA that can be used to model a brittle material such as concrete; however, many of them require stress-strain input, which is not easily obtained for a fully grouted masonry wall.

Since the grout and CMUs possessed different compressive strengths, but in the model were not distinguished separately, an average compressive strength was calculated for a single grout-filled CMU. The compressive strength of the CMU was taken as 1,350 psi based on the recommended values found in the SBEDS manual. From the results of grout testing presented in Chapter 3, the grout compressive strength was taken as 4,700 psi. A conservative average compressive strength was found by performing the simple calculation shown in Fig. 4.2. From this calculation, an average strength of the cross section was found to be 3,169 psi. The supplier of the CMUs claimed that the CMU strength was 2,200 psi. Therefore, a compromised value of 2,500 psi was used for modeling. Note that, unlike standard design calculations where the strength of the CMU governs the capacity, here it is important to also account for energy absorbed through cracking of the entire cross section.
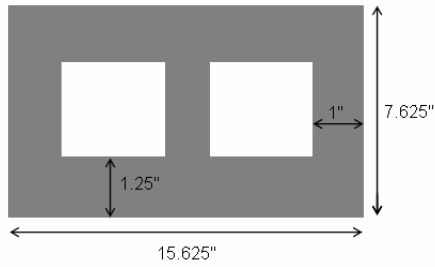
	f_c' (psi)	Area (in^2)	f_c' x Area
CMU	1,350	54.44	73,494
Grout	4,700	64.70	304,090
	Totals →	119.14	377,584

Average Strength = 3,169 psi

Conservatively used Strength = 2,500 psi

1"

1.25"

7.625"

15.625"

Fig. 4.2. Grouted CMU average strength calculation

Once a value for the compressive strength was established, it was used to obtain other necessary input parameters such as the tensile strength, the modulus of elasticity, as well as some terms that are specific to the LS-DYNA material card. The following shows the input for the *MAT BRITTLE DAMAGE card for concrete:

```
*MAT_BRITTLE_DAMAGE_TITLE

CONCRETE_96

$      MID         RO          E         PR     TLIMIT     SLIMIT     FTOUGH     SRETEN

        1 0.0001797   2.169E+6       0.20      375.0     1250.0       0.80      0.030

$     VISC     FRA_RF       E_RF      YS_RF      EH_RF      FS_RF       SIGY

     104.0        0.0        0.0        0.0        0.0        0.0     2500.0
```

where RO = mass density, E = Young's modulus, PR = Poisson's ratio, TLIMIT = tensile limit, SLIMIT = shear limit, FTOUGH = fracture toughness, SRETEN = shear retention, VISC = viscosity, FRA_RF – FS_RF = reinforcement parameters (not used), and SIGY = compressive yield stress of brittle material.

4.4.4 XEPS Foam

The material properties of XEPS foam were collected via laboratory testing. The material data collection process was described in Chapter 3. Several challenges arose while attempting to simulate the dynamic behavior of the foam. Despite the local issues

encountered during the simulations, the global challenge of modeling foam stems from its relatively low stiffness, ultimate strength, and density in comparison to its neighboring components. Foam is also inherently irregular because its density will increase during compression due to the presence of air pockets. As foam crushes, it is initially stiff but then reaches a plateau stress. At this point, the foam loses most of its stiffness until it begins to lock up during extreme compressive strain. Another nonlinearity that foam possesses is viscoelastic behavior, which means that its stress-strain response is not just dependent upon the material, but also upon the rate of loading (or strain rate). Therefore, under a very rapid loading, its stiffness will be greater than if the same amount of load was applied very slowly. This strain rate dependency not only affects the stiffness, but also the ultimate capacity of the material. Because of these inherent properties, the stress-strain relationship for foam is extremely nonlinear.

The laboratory testing discussed in Chapter 3 did not include an investigation of strain rate effects of foam. The average stress-strain curves for the three different brands of foam discussed in Chapter 3 showed that there are minor variations between brands. Because of this, and because the foam used in the full-scale dynamic testing was produced by Dow, the stress-strain definition used for modeling the foam was the average quasi-static Dow curve. Since foams can be produced that are either stiffer or softer than the one used in testing, and since strain rate effects could stiffen the foam, the effects of the stress-strain properties of the foam on the overall resistance of the system were studied by scaling the average stress-strain Dow curve. The Dow curve was scaled by 0.5 and by 2. The three curves used in the FE modeling are shown in Fig. 4.3.

LS-DYNA includes several options of material cards for modeling foam. Some are tailored to certain types of foam such as polyurethane. Some of the material cards considered for modeling the foam included material #5 (*MAT SOIL AND FOAM), material #63 (*MAT CRUSHABLE FOAM), and material #83 (*MAT FU CHANG FOAM). *MAT CRUSHABLE FOAM proved to be the most practical for this project. It is a very simple foam model that is ideal for simulating the global behavior of the foam insulation. By definition, the model essentially assumes Poisson's ratio to be zero. After running several simple models of foam in uniaxial compression, it was found that in order to avoid negative volume errors, Poisson's ratio had to be explicitly set equal to zero in the material card. Although the assumption that Poisson's ratio equals zero
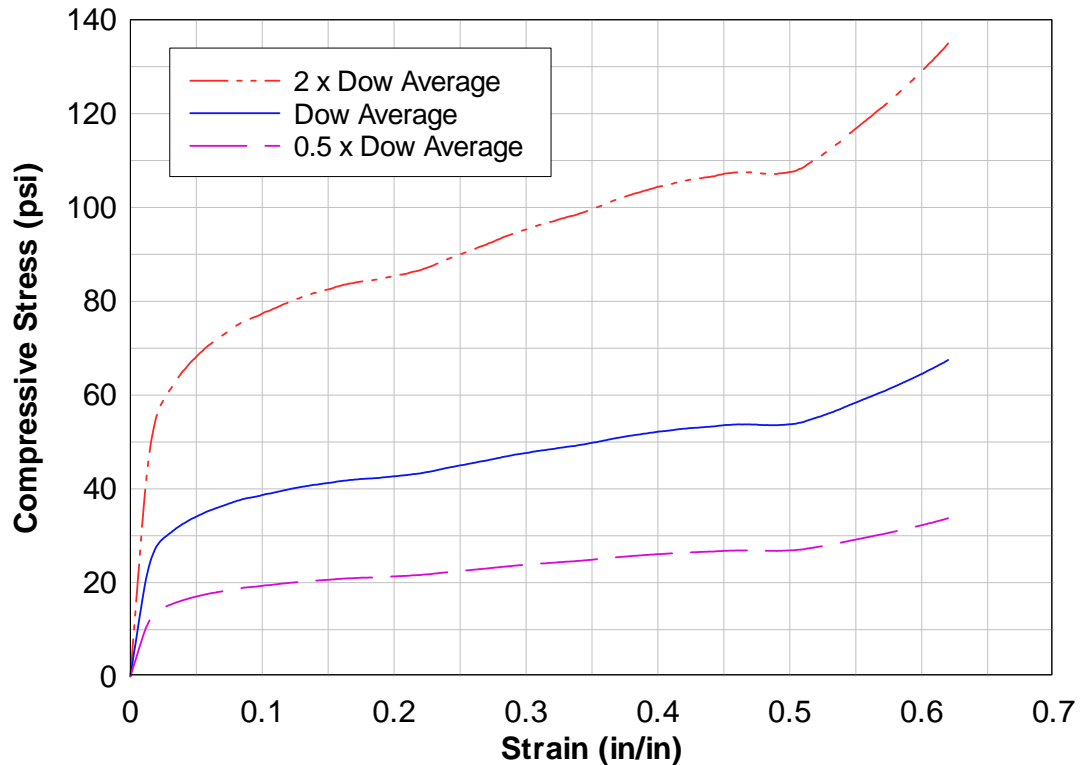
Fig. 4.3. Stress-strain curves for XEPS foam

becomes less accurate under larger strains, it is an acceptable assumption due to the geometry of the system. The following display shows the input for the *MAT CRUSHABLE FOAM card for the unscaled average Dow foam:

```
*MAT_CRUSHABLE_FOAM_TITLE
DOW_AVG_63
$      MID        RO        E        PR      LCID       TSC       DAMP
         3 2.5527E-6   1790.00       0.0         3     50.00       0.10
```

where RO = mass density, E = Young's modulus, PR = Poisson's ratio, LCID = load curve ID defining yield stress versus volumetric strain, TSC = tensile stress cutoff, and DAMP = rate sensitivity via damping coefficient (0.05 < recommended value < 0.50).

4.5 Element Selection

Beam elements were used to model the steel reinforcement, and solid elements were used to model all of the other components. There are several options for the definition of beam elements. Truss elements can be used if only axial loading is to be considered. In order to account for all of the reinforcement's energy absorption capability, the Hughes-Liu beam element formulation was chosen. The card for the beam element also includes the cross section definition of the beam. The values of TS1 and TS2 in the card define the diameter of the reinforcement. An element definition for the No. 5 reinforcement is as follows:

```
*SECTION_BEAM_TITLE
No_5_REBAR
$     SECID     ELFORM      SHRF    QR/IRID       CST     SCOOR       NSM
          3          1       1.0        2.0       1.0
$      TS1        TS2       TT1        TT2     NSLOC     NTLOC
       0.625      0.625
```

where ELFORM = element formulation option, SHRF = shear factor, QR/IRID = quadrature rule or rule number for user-defined rule, CST = cross section type, SCOOR = location of triad for tracking the rotation of the discrete beam element, NSM = nonstructural mass per unit length, TS1 = beam thickness or outer diameter in s direction at node n1, TS2 = beam thickness or outer diameter in s direction at node n2, TT1 = beam thickness or inner diameter in t direction at node n1, TT2 = beam thickness or inner diameter in t direction at node n2, NSLOC = location of reference surface normal to s axis, and NTLOC = location of reference surface normal to t axis.

Two different formulations of solid elements were used in the FE model. Eight-node hexahedral solid elements were used to mesh the concrete, the foam, and the rigid boundaries. To conserve computation time, the constant stress solid element was used for the concrete and the rigid boundaries. A fully integrated solid element was used for the foam to eliminate hourglassing. The following shows the element definitions for the constant stress and the fully integrated hexahedral solid elements, respectively:

```
*SECTION_SOLID_TITLE
CONSTANT_STRESS_HEX
$     SECID     ELFORM        AET
          1          1


*SECTION_SOLID_TITLE
FULLY_INTEGRATED_HEX
$     SECID     ELFORM        AET
          2          2
```

where ELFORM = element formulation option, and AET = ambient element type.

4.6 Contact Surfaces

Contact surfaces can be created in LS-DYNA using *SET SEGMENT cards, which represent particular surfaces that will be in contact with other surfaces that have their own independent *SET SEGMENT cards. Once the surfaces are defined, the contact definitions are created using the *CONTACT card. LS-DYNA has many options for defining contact relationships. A straightforward approach is the *CONTACT AUTOMATIC SURFACE TO SURFACE card. For this type of simulation, the only necessary input data were the static and dynamic coefficients of friction for the respective interface. The coefficients of friction were estimated based on recommended values (these values have little impact because sliding energy is very small when compared to internal or kinetic energy). Based on the assumption that the metal ties would hold the brick against the foam throughout the response, the foam needed to be permanently attached to the CMU wythe to ensure that mass was conserved. Since using a contact definition is a computationally intense way to permanently attach two components to each other, the coincident nodes of the foam and concrete were merged. This made the simulation more economical by reducing the number of contact interfaces to only the interface between the CMU wythe and the support plates. The contact definition used in the model was defined as follows:

```
*CONTACT_AUTOMATIC_SURFACE_TO_SURFACE_ID
$ CID   HEADING
         1
$ SSID   MSID   SSTYP   MSTYP   SBOXID   MBOXID   SPR   MPR
         1   2   0   0
$ FS   FD   DC   VC   VDC   PENCHK   BT   DT
       0.8   0.60   0.0   0.0   0.0   0   0.0 1.00E+20
```

where SSID = slave segment set ID, MSID = master segment set ID, SSTYP = slave

segment set type, MSTYP = master segment set type, SBOXID – MPR = unused

parameters, FS = static coefficient of friction, FD = dynamic coefficient of friction, DC –

PENCHK = unused parameters, BT = birth time, and DT = death time.


## 4.7 Loading

To minimize computation time, one full-scale dynamic test case was chosen to

compare with the FE model results. Detonation 3 was selected because it possessed the

largest deflections of the two most successful detonations. However, since reliable

pressure data was not retrieved from Detonation 3, the load used in the FE models was

predicted using SBEDS (SBEDS is described in Chapter 5). Fig. 4.4 shows a plot of the

pressure history used in the FE models along with its respective impulse.

Many studies of this nature might use the *LOAD BLAST card to apply the

pressure. This would produce overly conservative deflection results due to the omission

of the negative phase. While this could be acceptable for design, it would still be very

expensive due to over-designed members. The load predicted by SBEDS was applied as

two individual loads. The positive phase was applied to the exterior surface of the wall

(i.e. the exposed surface of the foam). The negative phase was applied to the interior

surface of the wall section (i.e. the exposed surface of the CMU wythe). This was done

so that the entire mass of the wall would receive load in a compressive manner rather

than subjecting the foam to tensile loads during the negative phase.
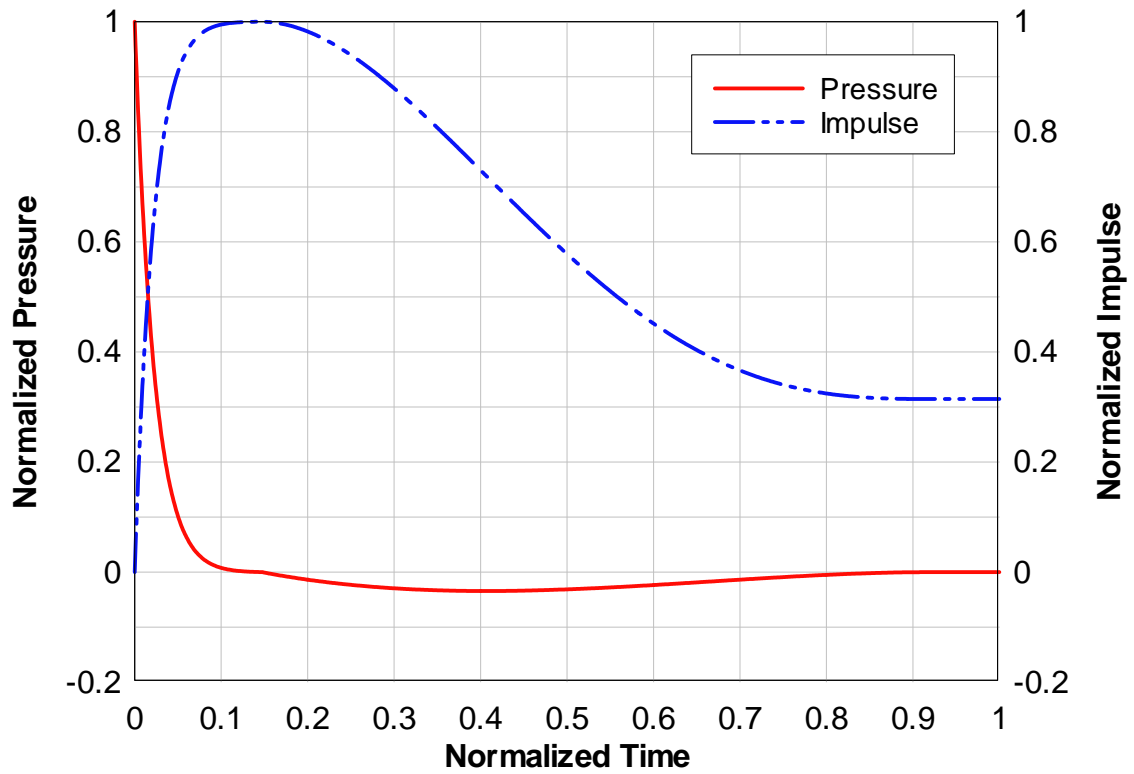
**Fig. 4.4.** SBEDS predicted load for Detonation 3

## 4.8 Finite Element Results

Before the FE modeling results are presented, a summary of the parameters varied

and the subsequent cases evaluated is presented. A benchmark case was run that

consisted of the CMU wythe without any foam on the exterior. The mass of the brick

veneer was included by adding mass to the exterior face of the CMU wythe. This

benchmark case will be referred to as FE-BM. Nine independent models that included

the foam were created. These were necessary to study the effects of both thickness and

stress-strain properties on the resistance provided by the foam. A summary showing the

names of each case is presented in Table 4.2.

**Table 4.2.** Summary of parameters varied and names for each respective case

| Foam Definition | 2-inch Thick | 4-inch Thick | 8-inch Thick |
|---|---|---|---|
| 0.5 x Dow Avg. Stiffness | 0.5Dow-2 | 0.5Dow-4 | 0.5Dow-8 |
| Dow Avg. Stiffness | Dow-2 | Dow-4 | Dow-8 |
| 2 x Dow Avg. Stiffness | 2Dow-2 | 2Dow-4 | 2Dow-8 |

### 4.8.1 Energy Plots

For each case, the total energy in the system was checked against the global

internal, kinetic, sliding, and hourglass energy to ensure the validity of the results. For

each case, the sum of the individual energies should equal the total energy for any point

in the response history. Also, hourglass energy should be kept to a minimum. If

hourglass energy is contributing significantly to the total energy of a model, then there is

unrealistic distortion in the elements, and the model must be refined. A typical rule of

thumb is to limit hourglass energy to less than 5% of the total energy. The following

figures present the global energy histories for each case.
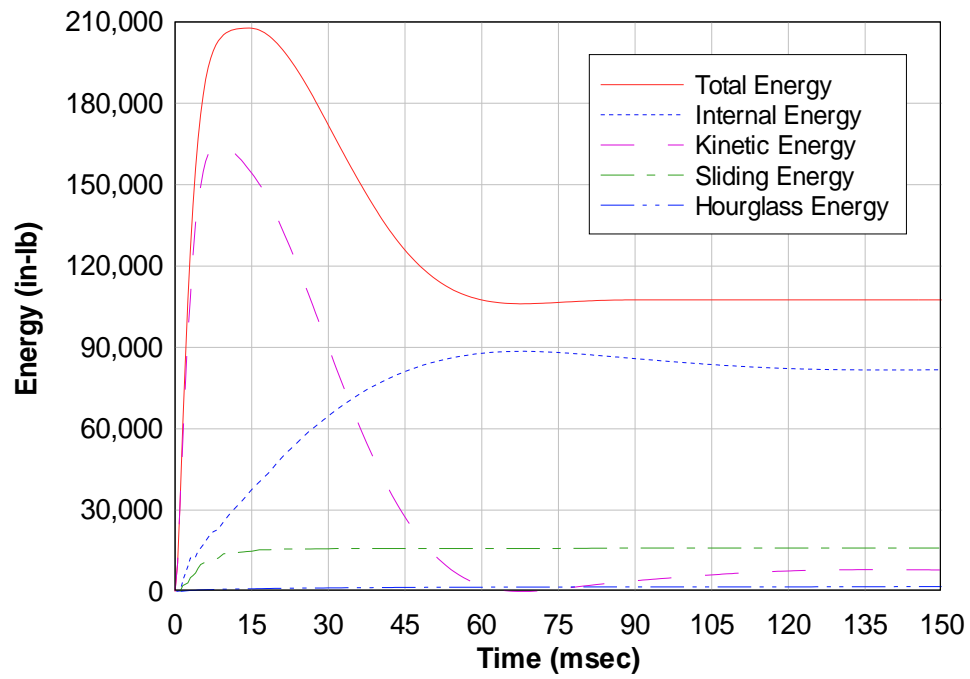
**Fig. 4.5.** FE-BM global energy history
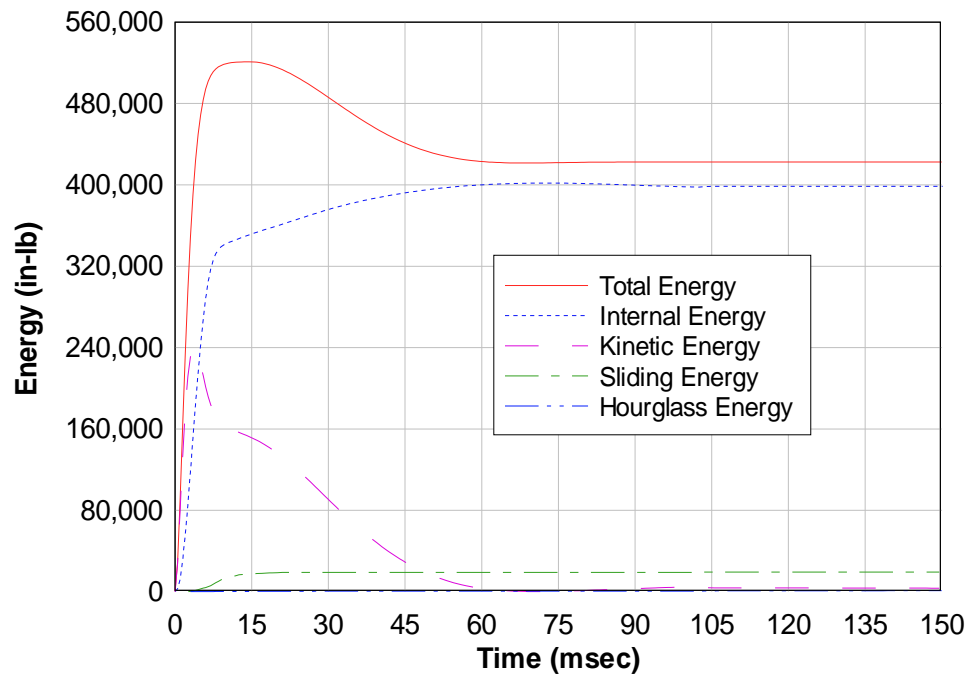


**Fig. 4.6.** 0.5Dow-2 global energy history

94
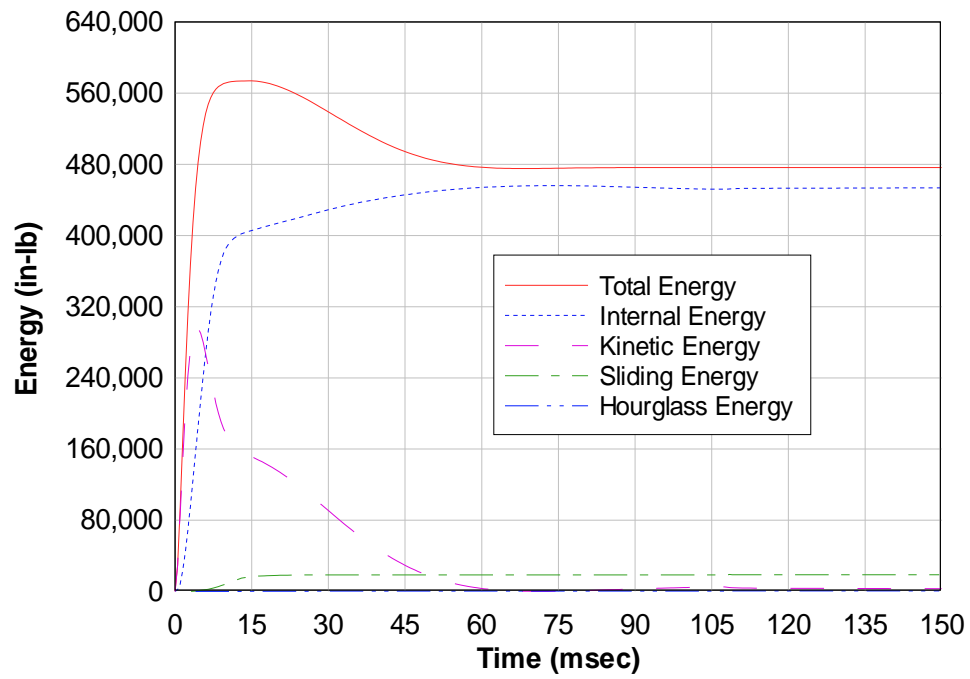
**Fig. 4.7.** 0.5Dow-4 global energy history



**Fig. 4.8.** 0.5Dow-8 global energy history

95

**Fig. 4.9.** Dow-2 global energy history



**Fig. 4.10.** Dow-4 global energy history

96

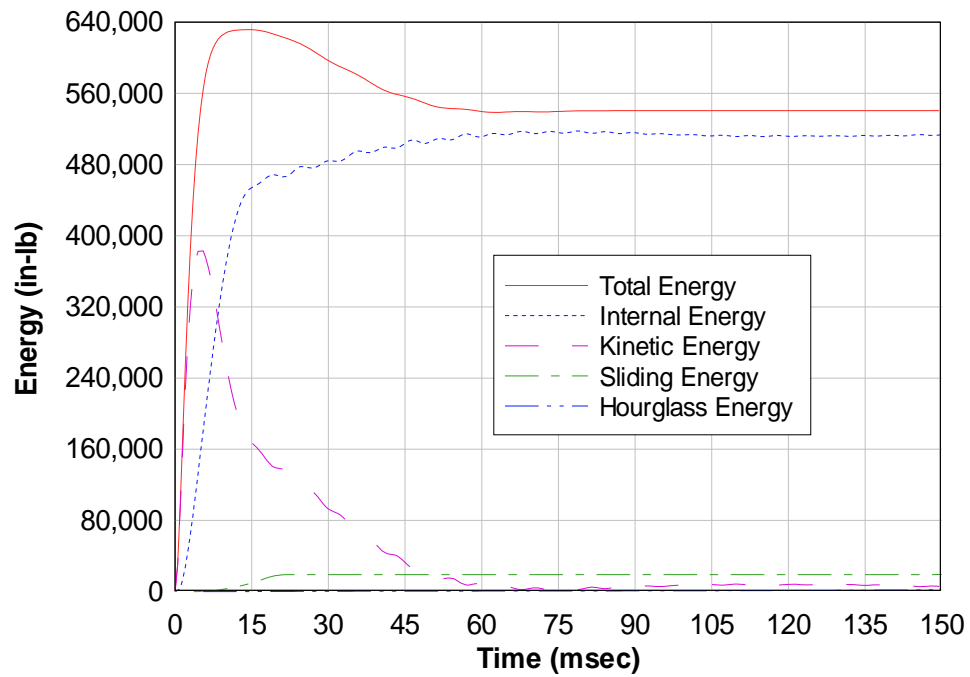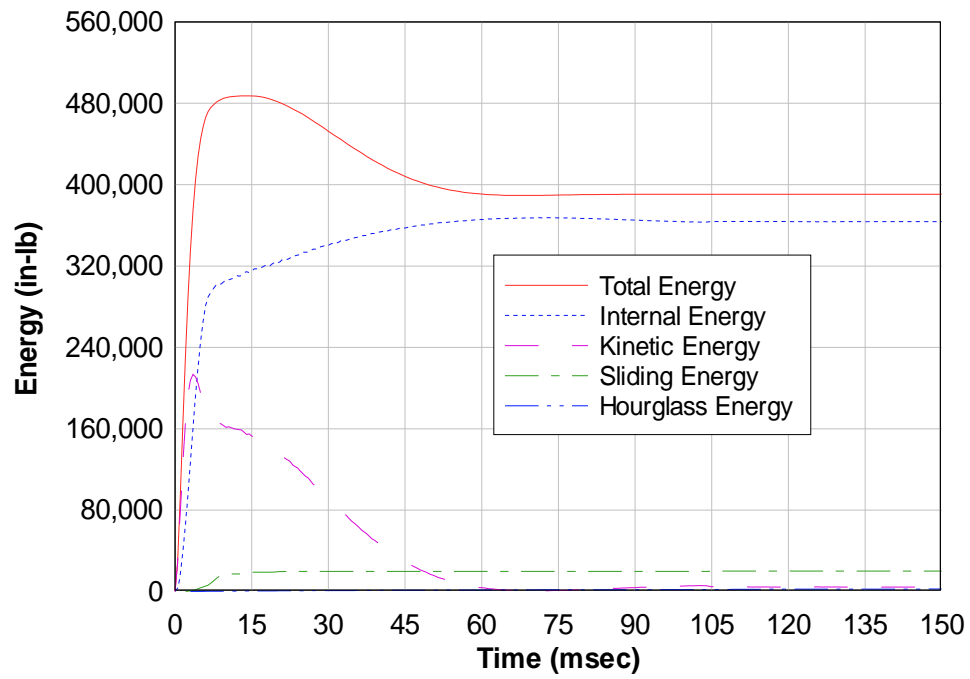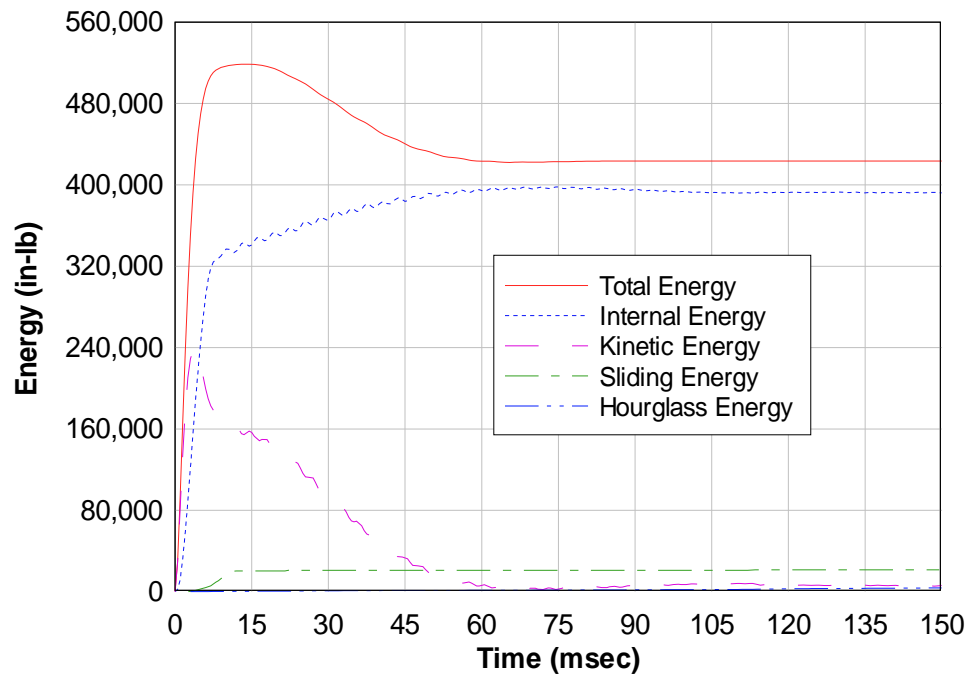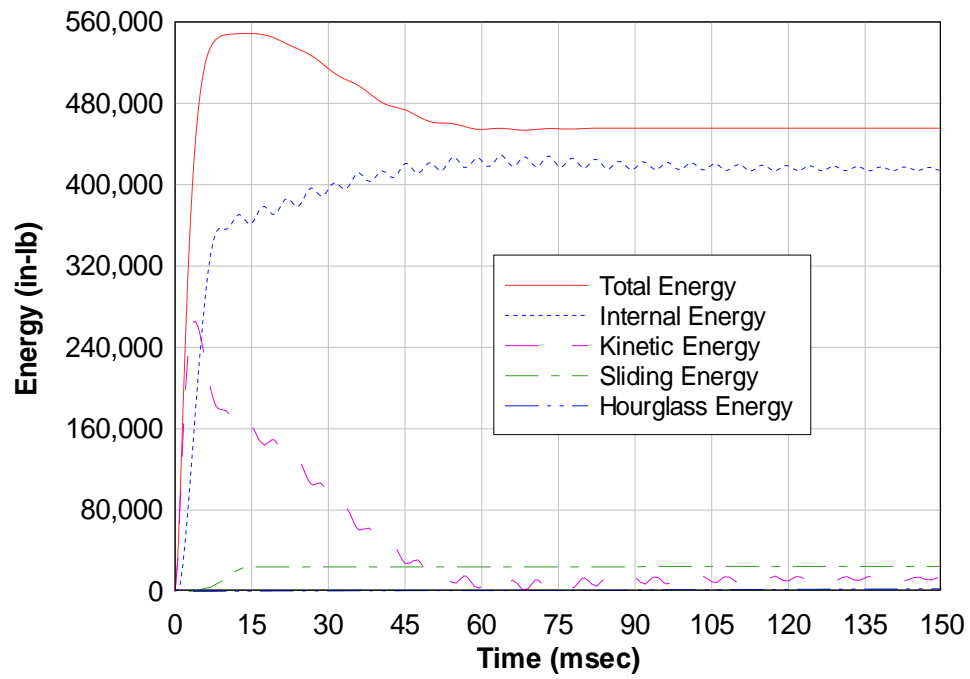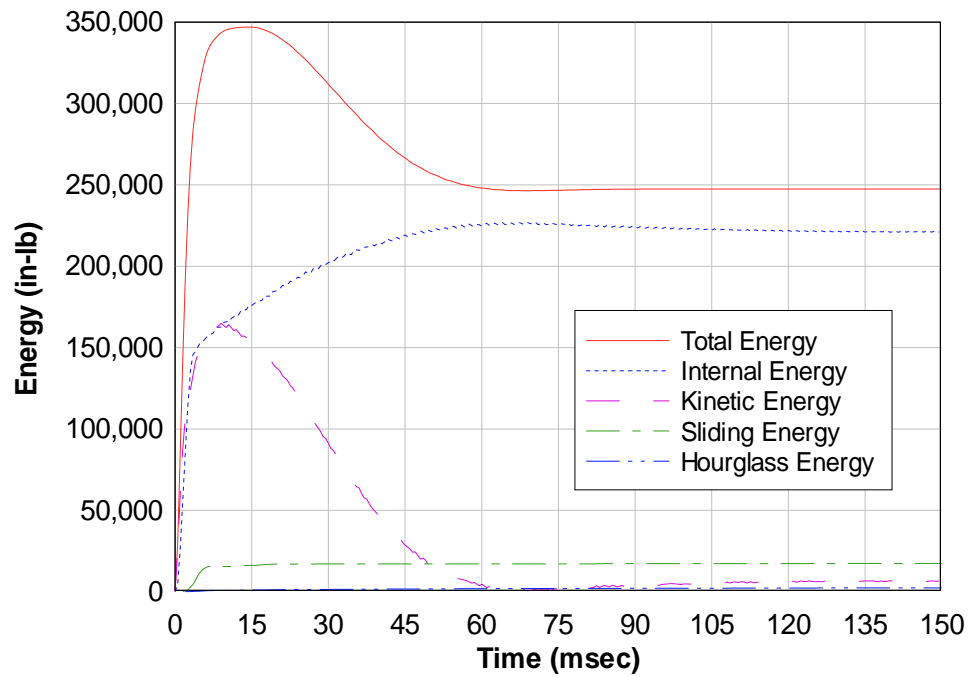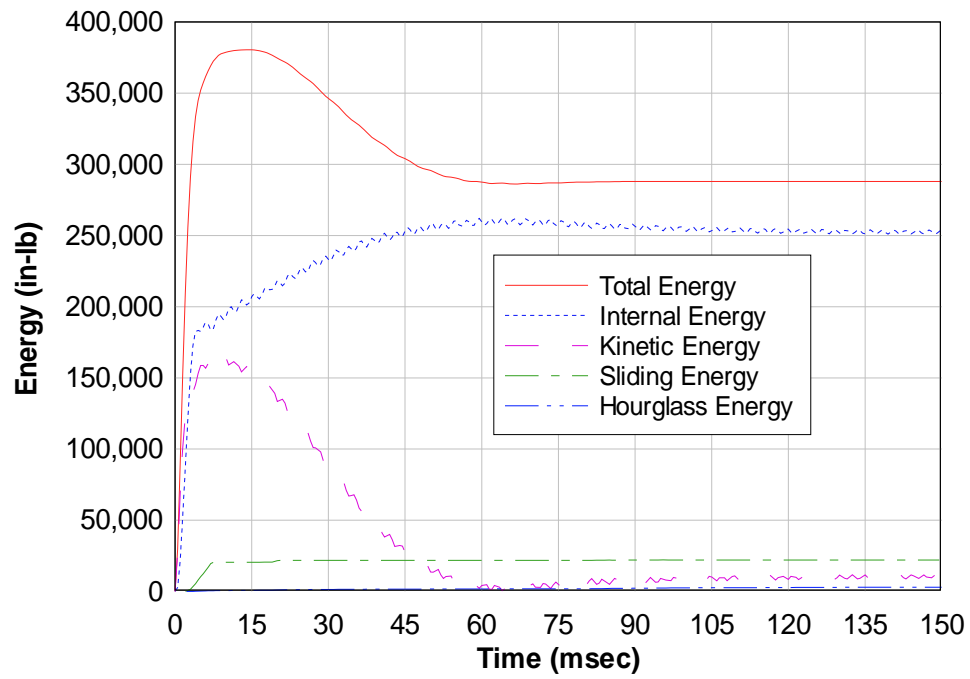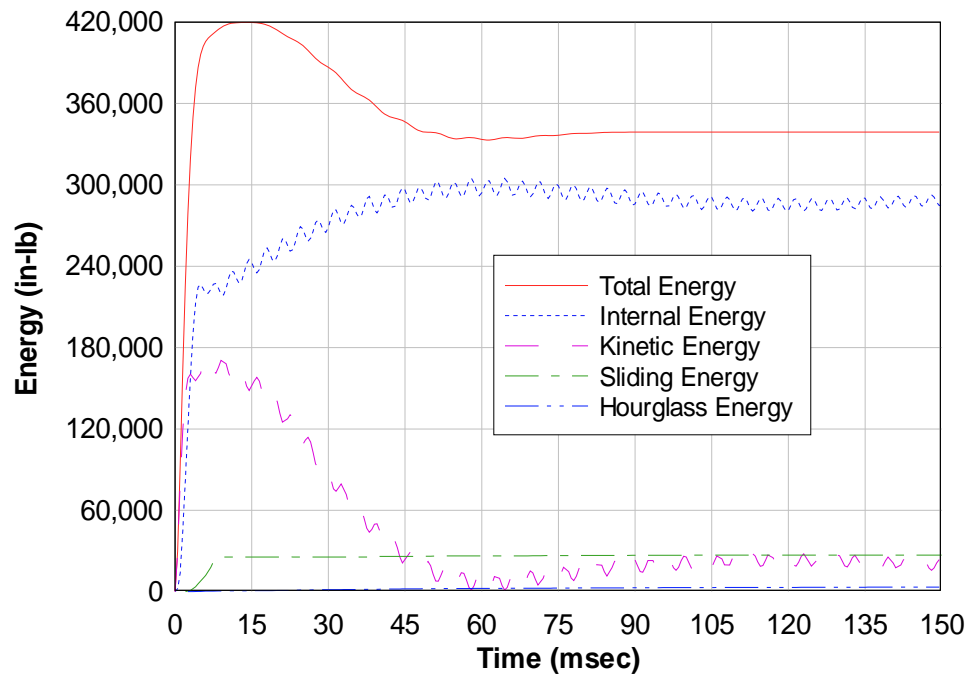**Fig. 4.11.** Dow-8 global energy history



**Fig. 4.12.** 2Dow-2 global energy history

**Fig. 4.13.** 2Dow-4 global energy history



**Fig. 4.14.** 2Dow-8 global energy history

98

From the previous figures it can be seen that the hourglass energy represents a very small percentage of the total energy of the system. It can also be seen that if the individual energies are summed, values identical to the total energy are produced. Therefore, these models were found to be adequate for further analysis.

The global energies shown in the previous plots can each be subdivided according to their respective material cards. An investigation of the local internal energies helps provide an understanding of how much each component contributes to the overall resistance of the system in relation to the other components. In many cases, plotting the internal energy can also provide insight into the timing of the event. This exercise can be used to determine the limits associated with certain resistance mechanisms by relating the timing of the energy to the timing of a specific deflection value. Figures 4.15 through 4.24 show the internal energies of each component for each analysis case. From these plots it can be seen that the foam absorbs a large amount of strain energy very quickly at the beginning of the response. It can also be observed that the peak internal energy in the concrete is lower in the cases where foam is present than in the case where there is no foam (the FE-BM case). This shows that the foam is adding resistance to the system by reducing the amount of energy the concrete must absorb. To show this more clearly, the internal energies of the concrete for each foam type were compared to the internal concrete energy seen in the benchmark simulation. Similar comparisons were also made for the reinforcement internal energies. These comparisons are shown in Figures 4.25 through 4.30.
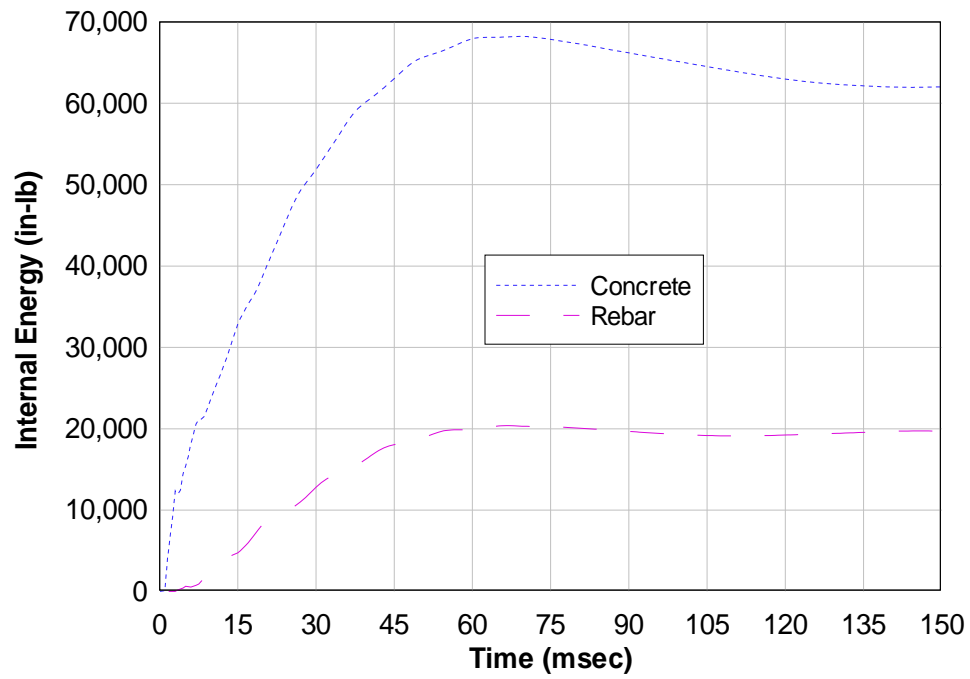
**Fig. 4.15.** FE-BM local internal energy history
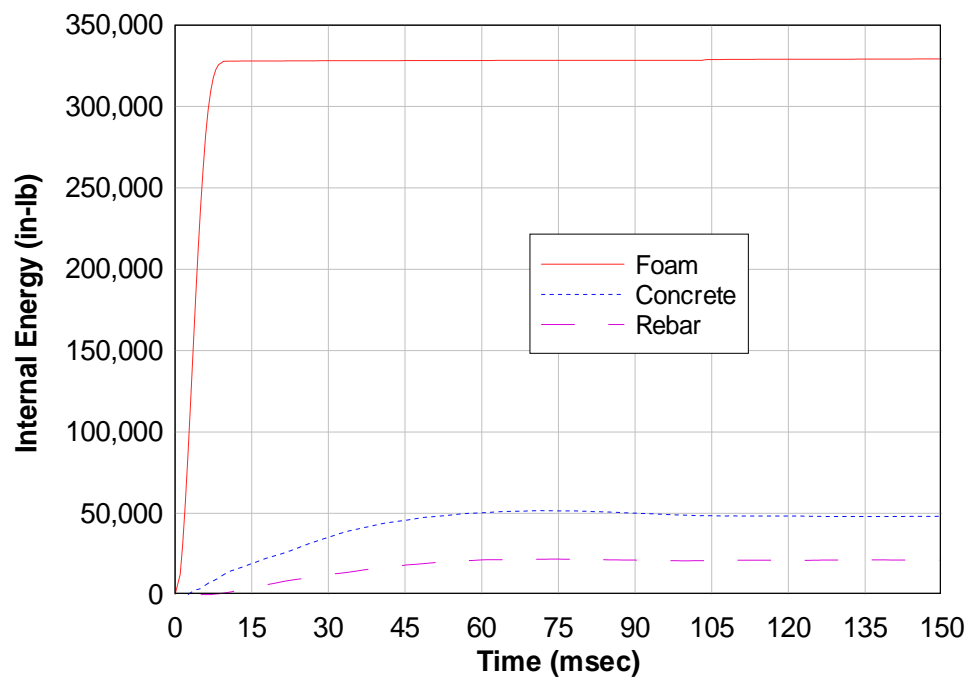


**Fig. 4.16.** 0.5Dow-2 local internal energy history

100
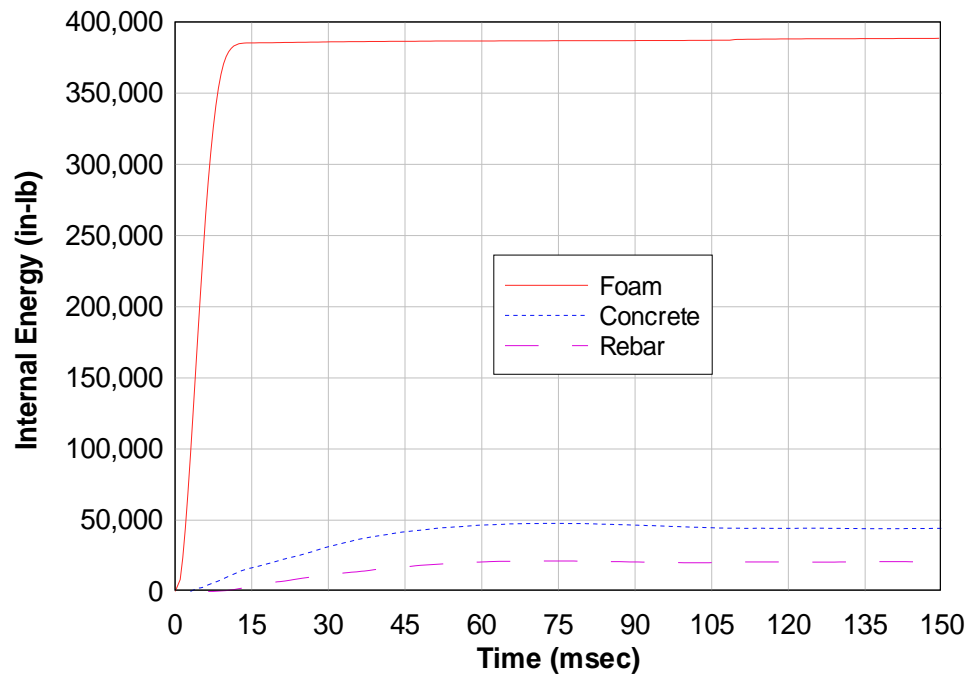
**Fig. 4.17.** 0.5Dow-4 local internal energy history
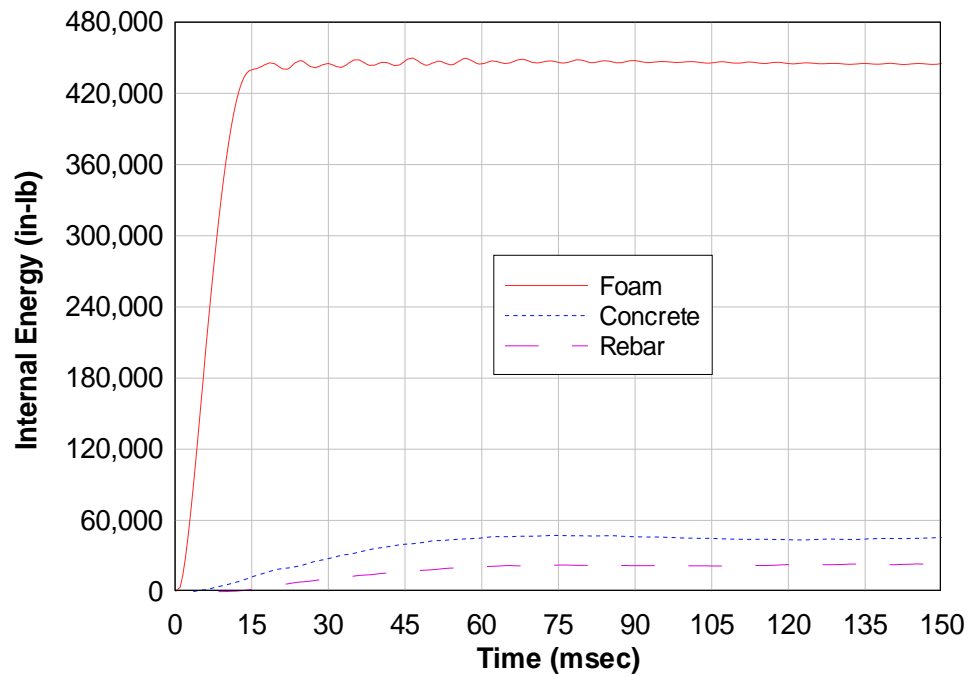


**Fig. 4.18.** 0.5Dow-8 local internal energy history

101
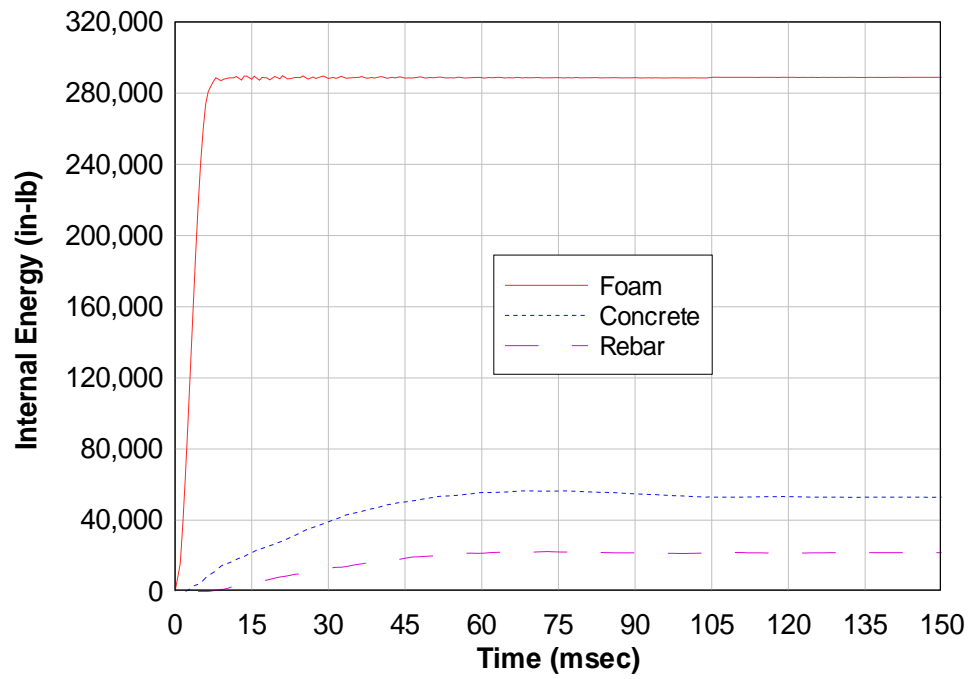
**Fig. 4.19.** Dow-2 local internal energy history
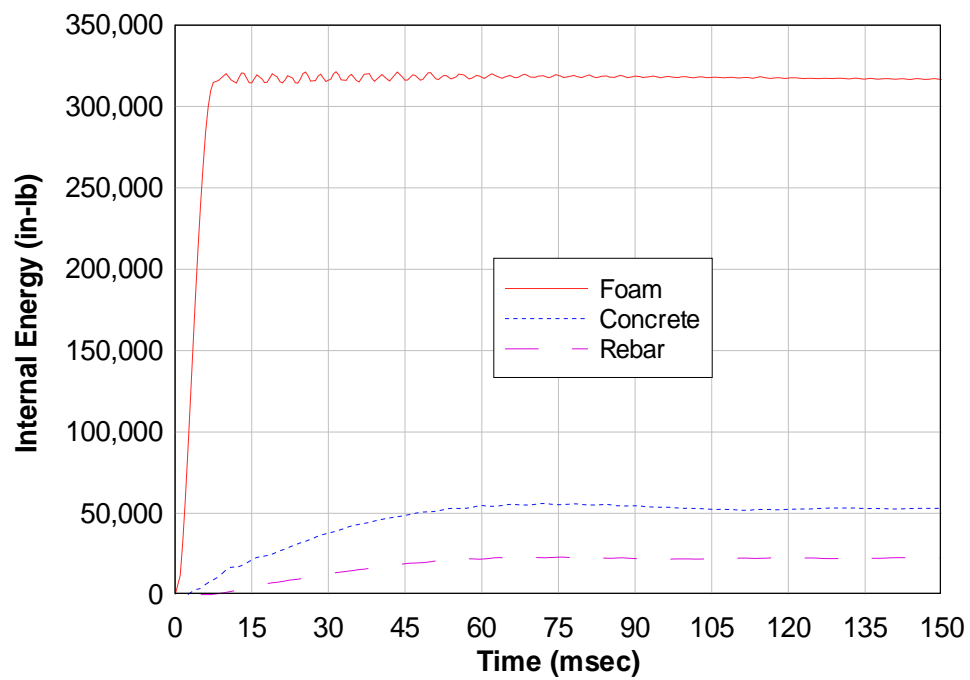


**Fig. 4.20.** Dow-4 local internal energy history

102
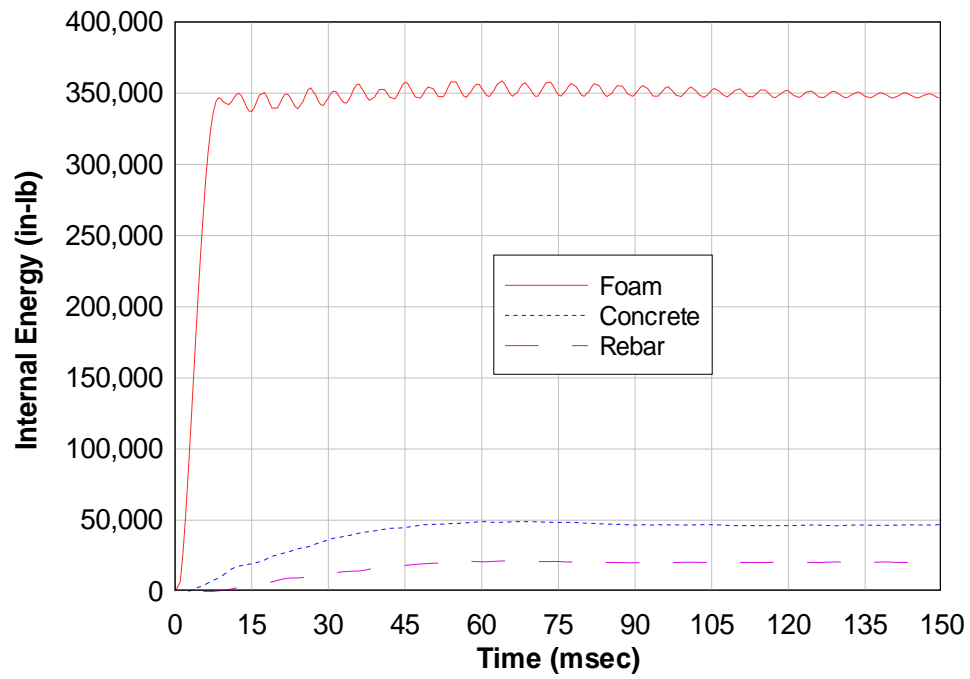
**Fig. 4.21.** Dow-8 local internal energy history
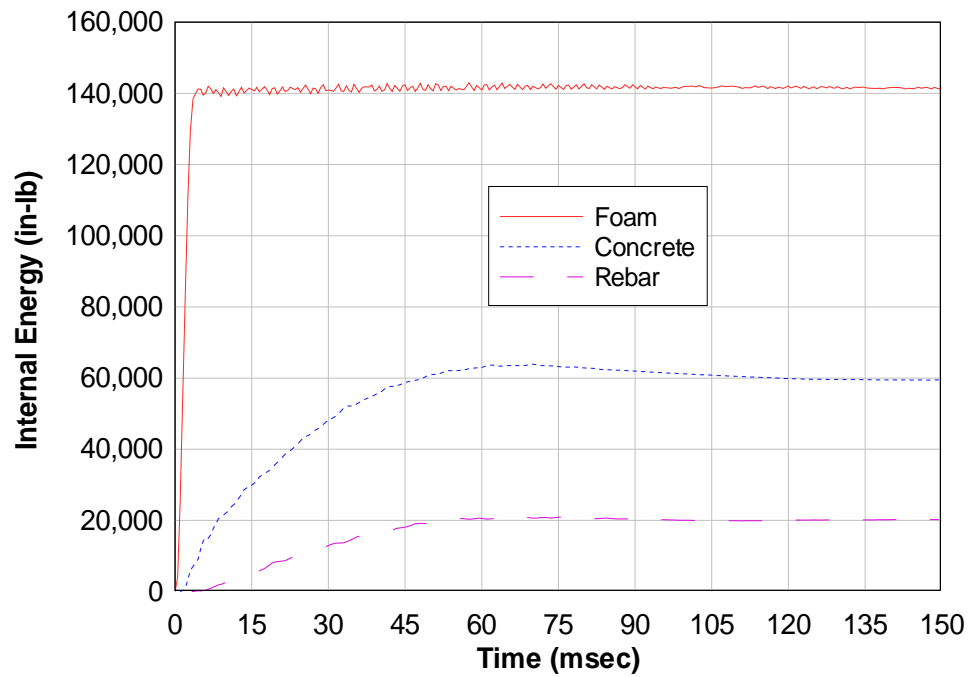


**Fig. 4.22.** 2Dow-2 local internal energy history

103
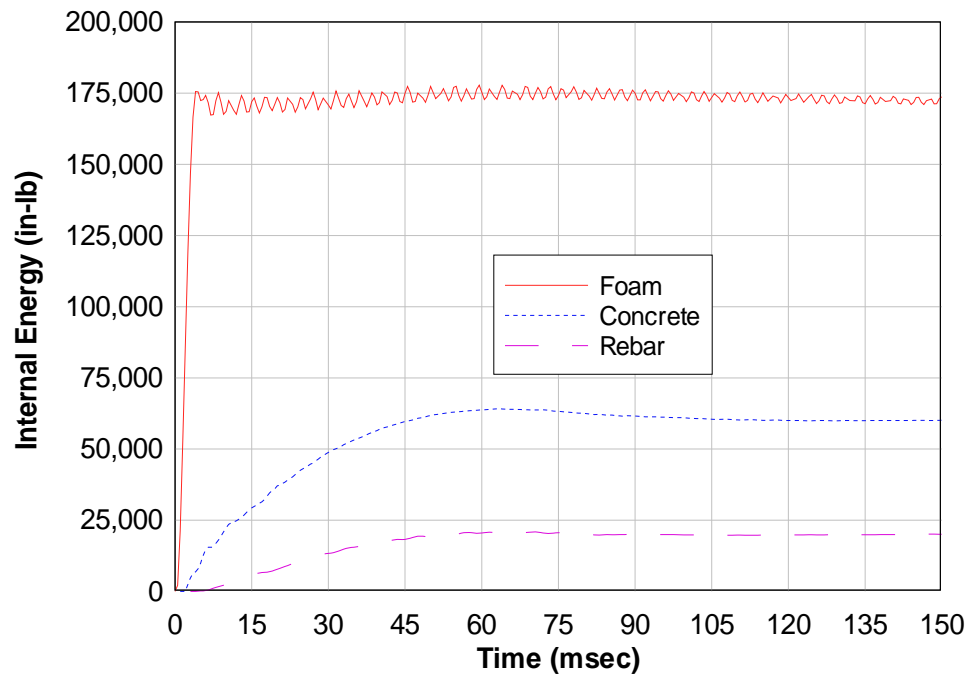
**Fig. 4.23.** 2Dow-4 local internal energy history
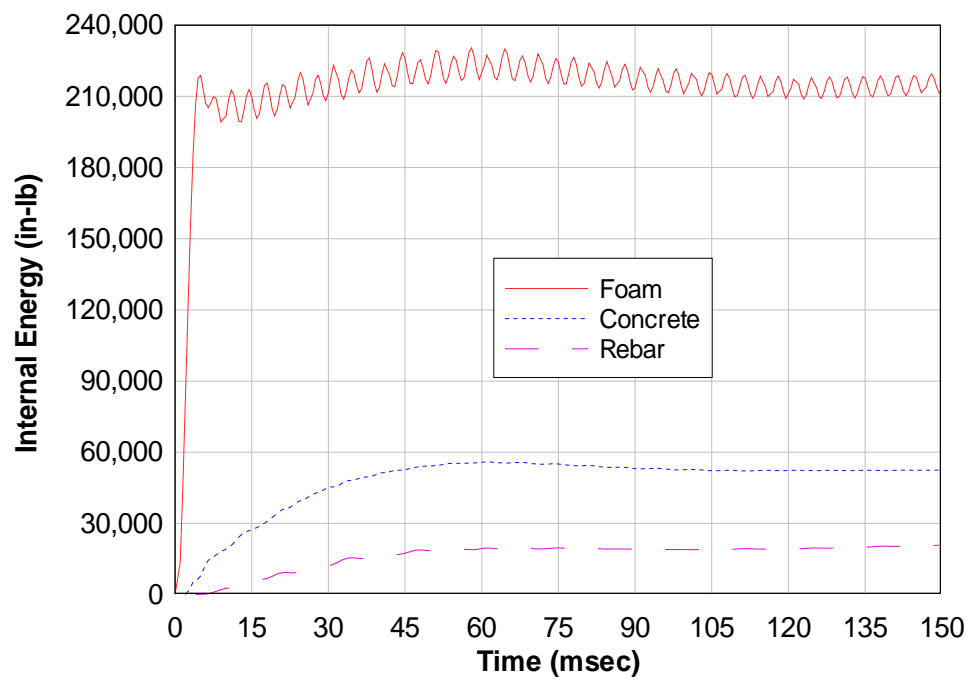


**Fig. 4.24.** 2Dow-8 local internal energy history
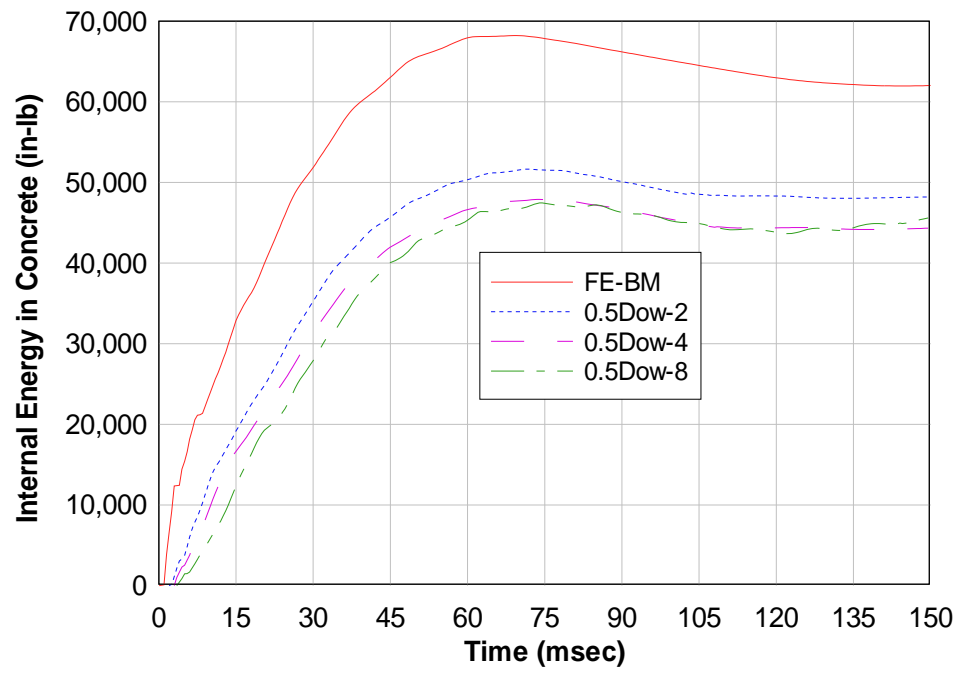
**Fig. 4.25.** 0.5Dow concrete energy compared to FE-BM concrete energy
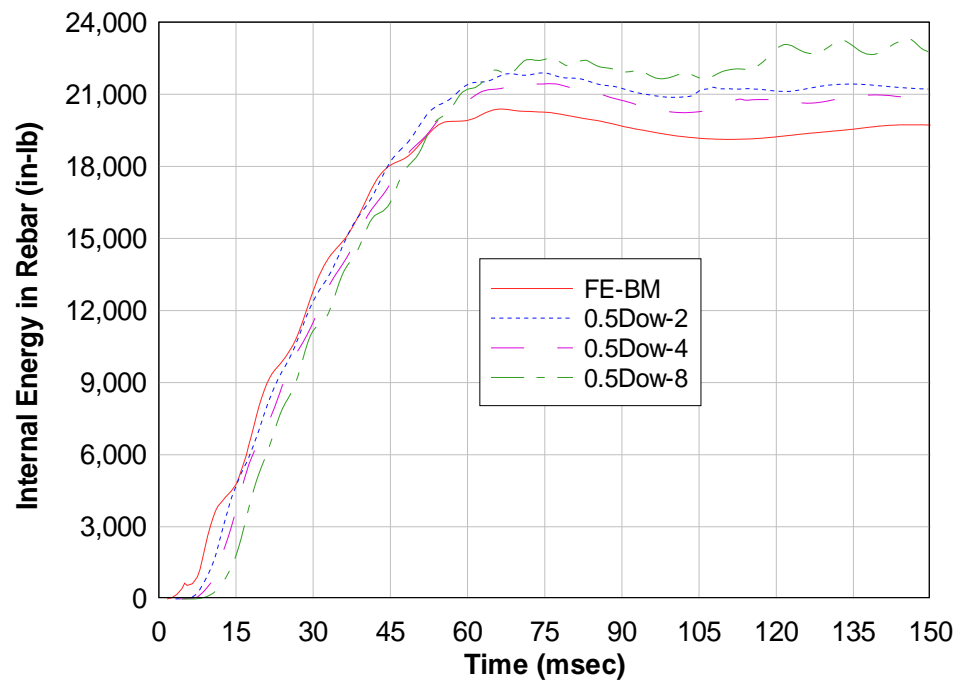


**Fig. 4.26.** 0.5Dow reinforcement energy compared to FE-BM reinforcement energy

105
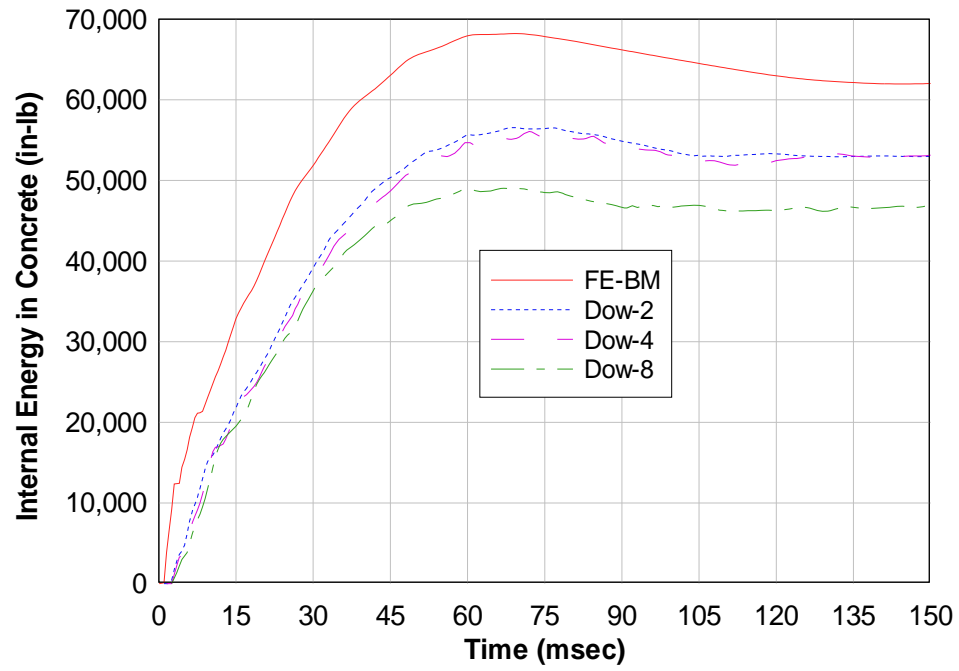
**Fig. 4.27.** Dow concrete energy compared to FE-BM concrete energy
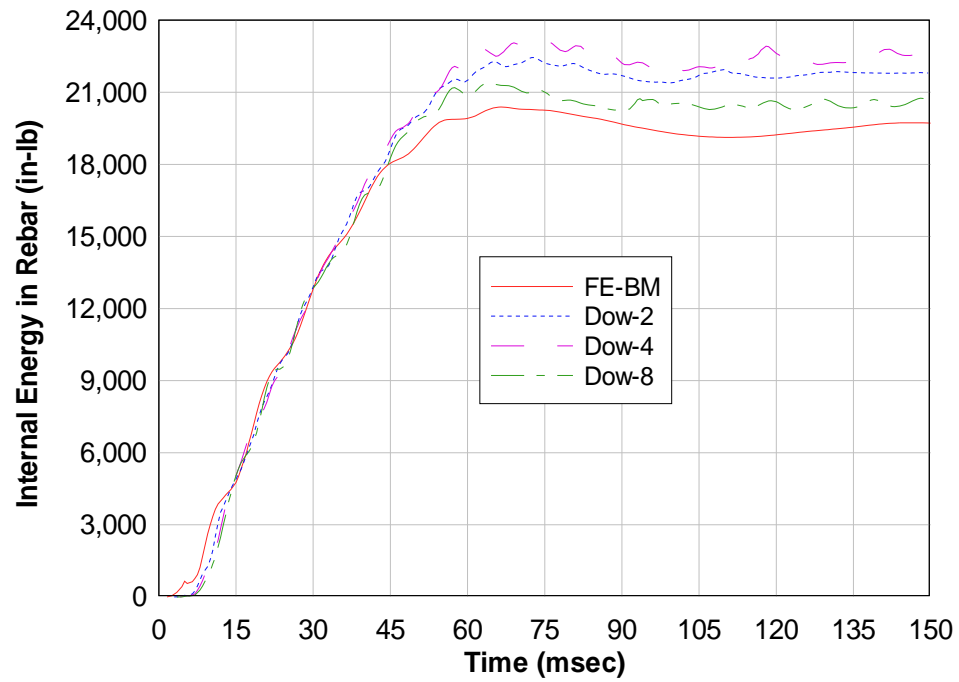


**Fig. 4.28.** Dow reinforcement energy compared to FE-BM reinforcement energy
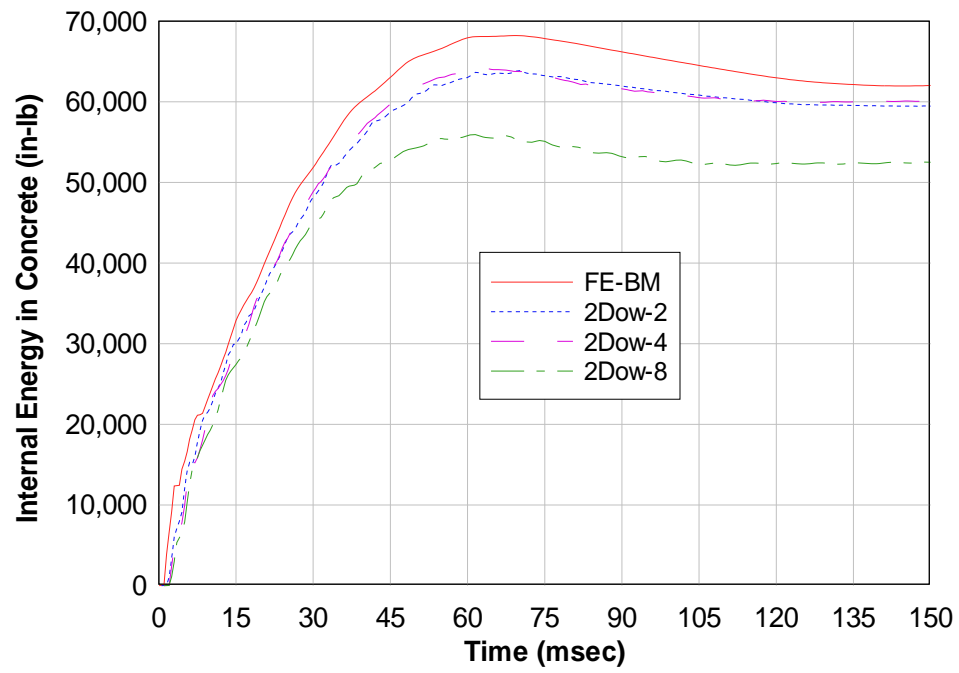
**Fig. 4.29.** 2Dow concrete energy compared to FE-BM concrete energy
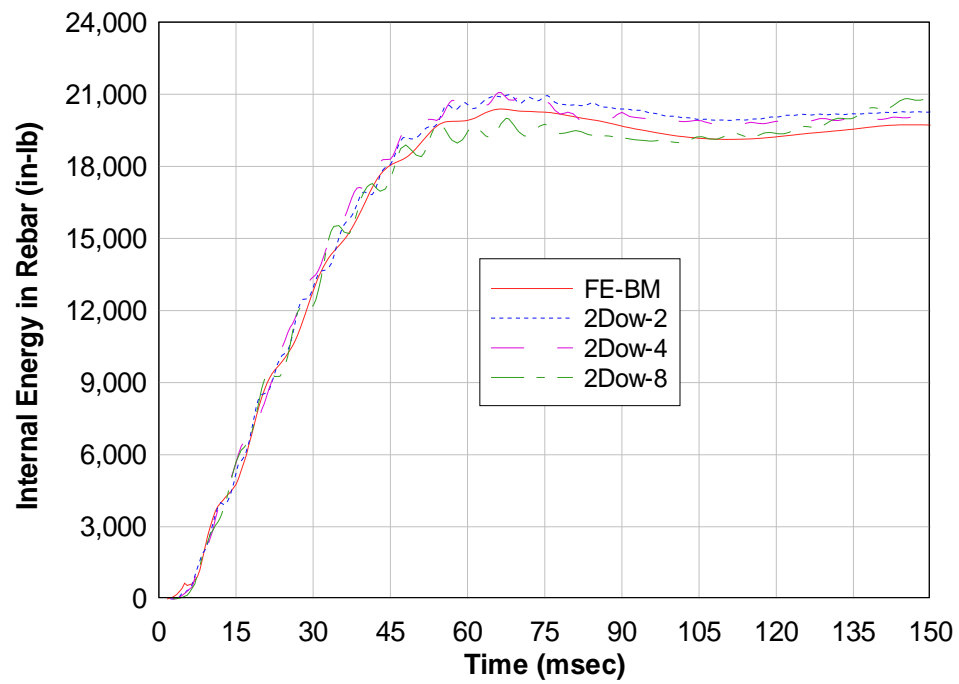


**Fig. 4.30.** 2Dow reinforcement energy compared to FE-BM reinforcement energy

The previous plots demonstrate that when the foam was present, the internal energy in the concrete decreased while in the reinforcement it increased. However, if the peak internal energies in the concrete and reinforcement are summed for each FE model, then it is clear that the total energy in the reinforced masonry wythe is less when the foam is present. These plots also show that the reduction in the internal energy of the CMU wythe becomes more pronounced as the foam becomes softer. Intuitively, this is appropriate because as the foam gets softer, the pressure that the CMU wythe is subjected to will be less until the foam begins to stiffen as it locks up.

### 4.8.2 Contour Plots

For each case, distributions of stress and strain throughout the system were studied. Three distributions were studied, as follows: 1) stress distribution in reinforcement, 2) strain distribution in reinforcement, and 3) longitudinal strain distribution in concrete. The distributions of stress in the concrete were also inspected but are not included since the critical tensile stress is carried by the longitudinal steel reinforcement.

A common reference point in time was chosen for all of the contour plots. The time at which the maximum mid-span displacement of each wall occurred was used as the common reference point. Figures 4.31 through 4.50 present the stress distributions and strain distributions in the reinforcement for each case. Because contour plots are difficult to read for beam elements, the distributions for the reinforcement are shown in a graphical form by plotting the intensity along the length of the reinforcement.
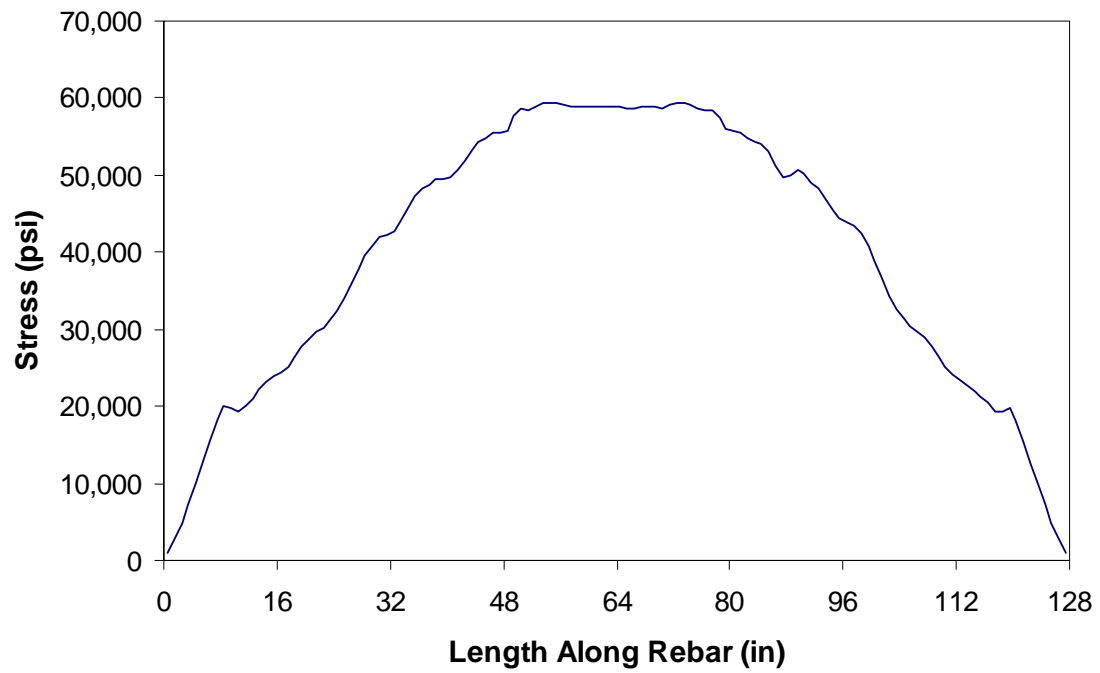
**Fig. 4.31.** Reinforcement stress distribution for FE-BM
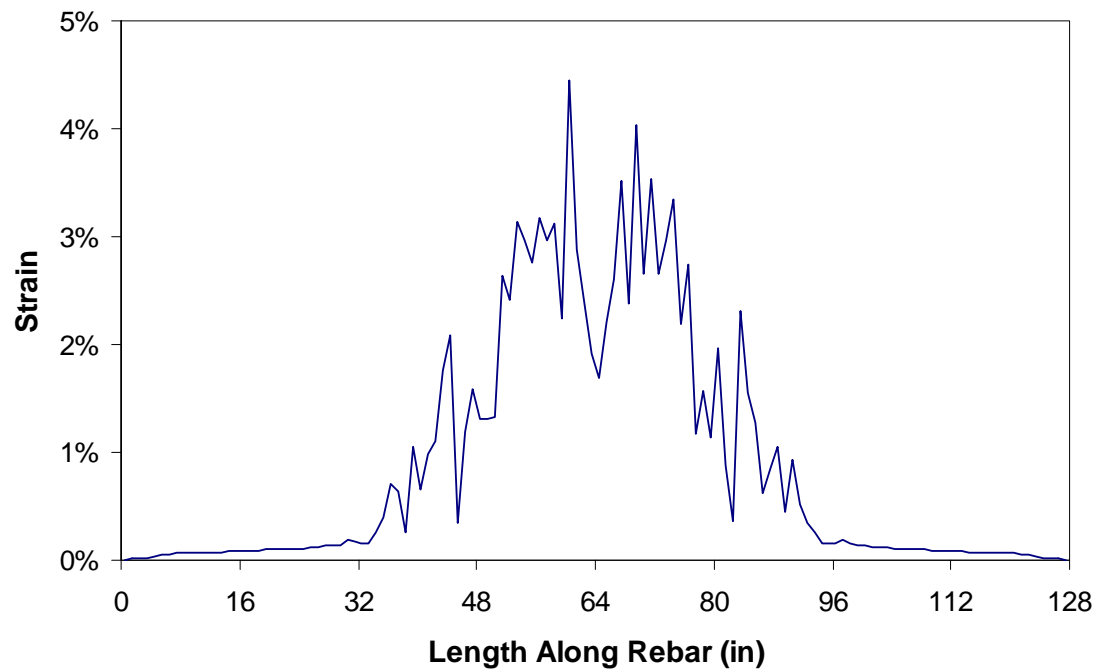


**Fig. 4.32.** Reinforcement strain distribution for FE-BM

109
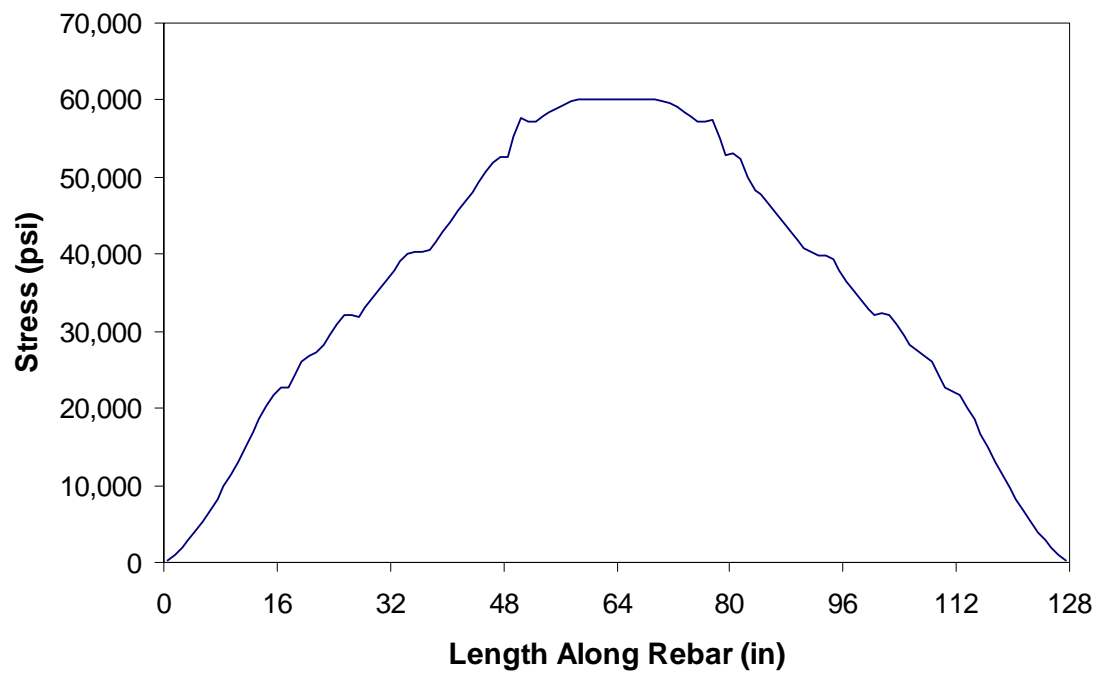
**Fig. 4.33.** Reinforcement stress distribution for 0.5Dow-2
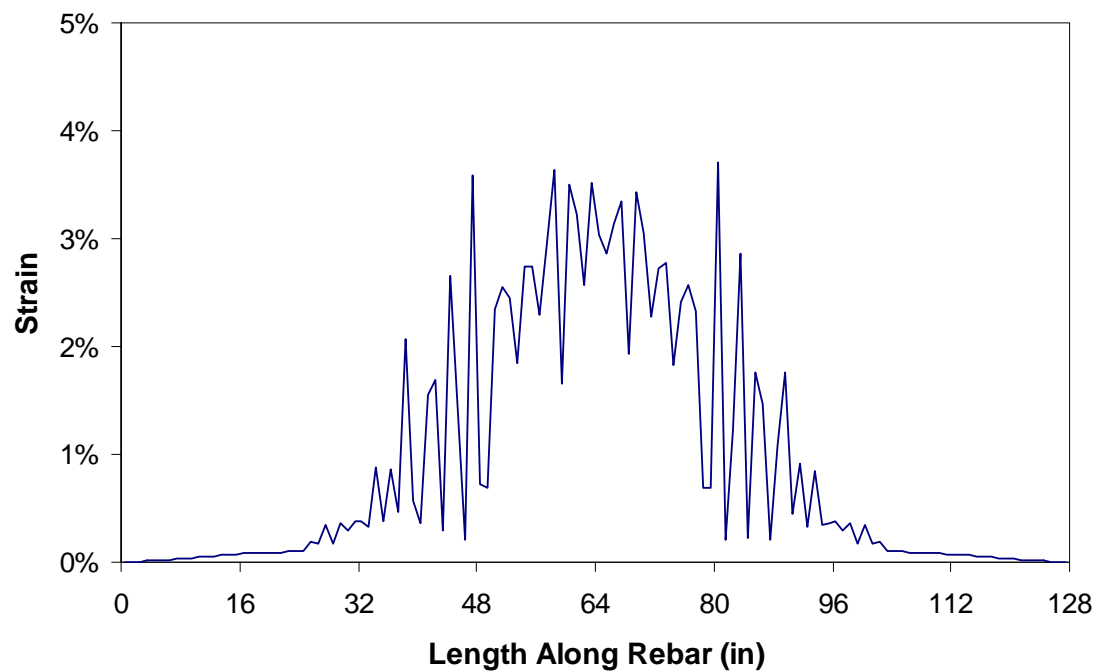


**Fig. 4.34.** Reinforcement strain distribution for 0.5Dow-2

110
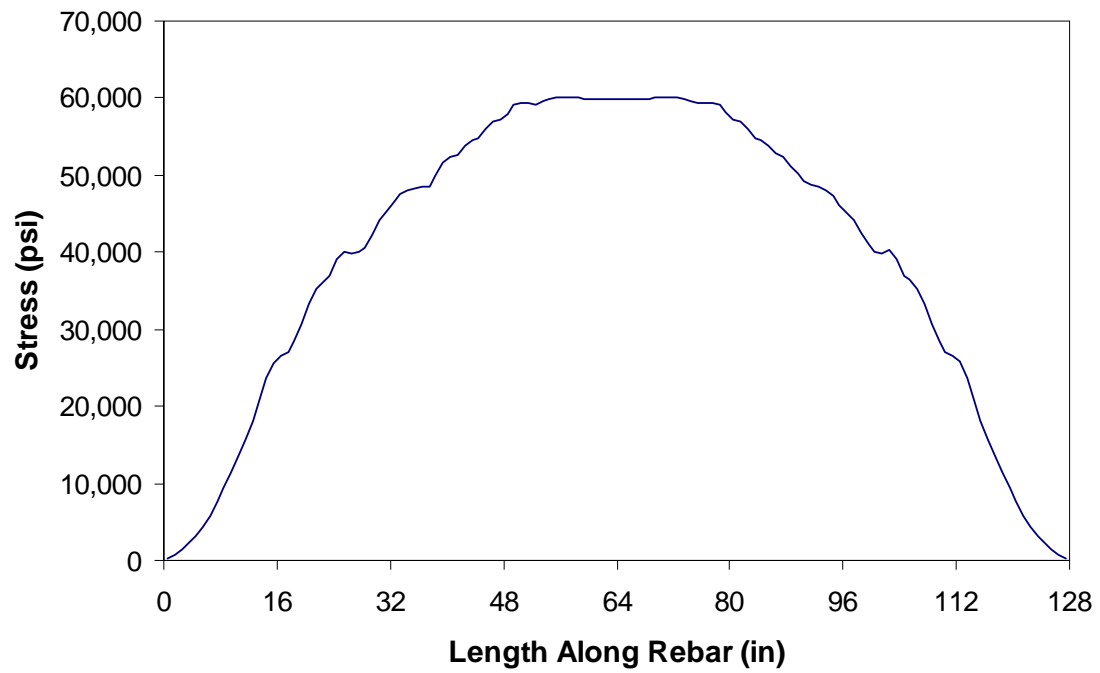
**Fig. 4.35.** Reinforcement stress distribution for 0.5Dow-4
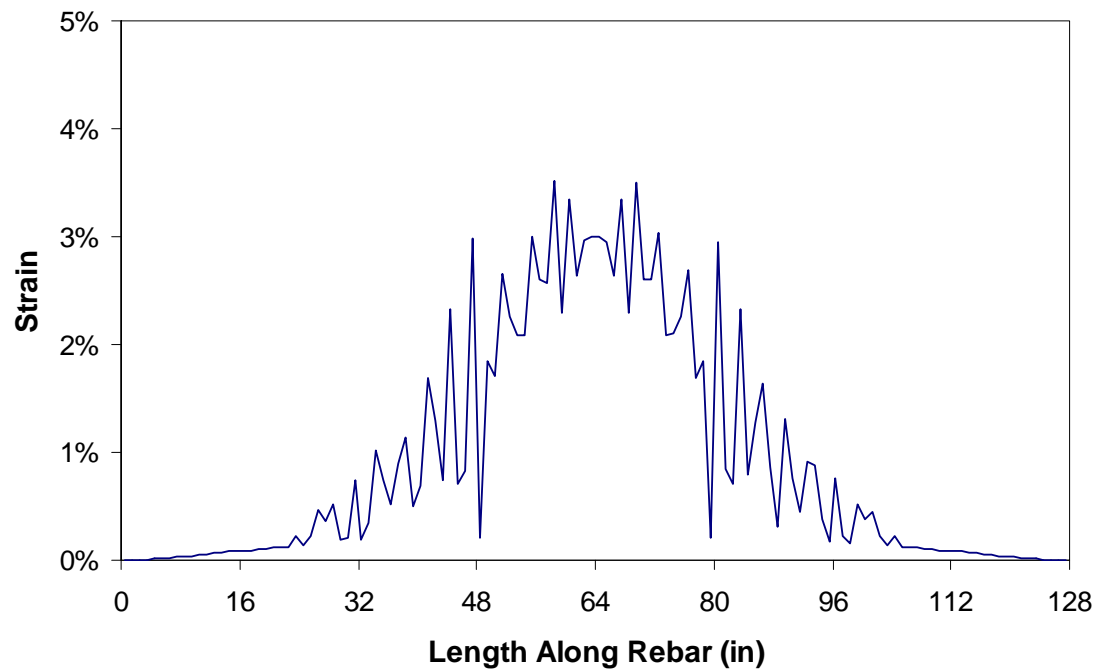


**Fig. 4.36.** Reinforcement strain distribution for 0.5Dow-4

111
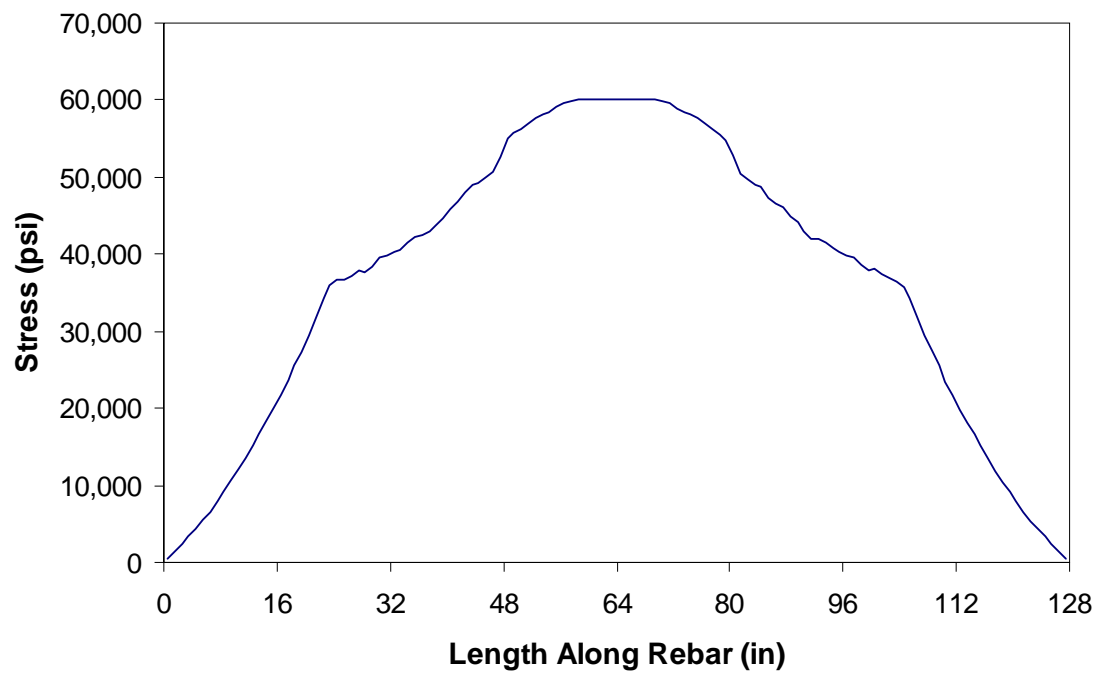
**Fig. 4.37.** Reinforcement stress distribution for 0.5Dow-8
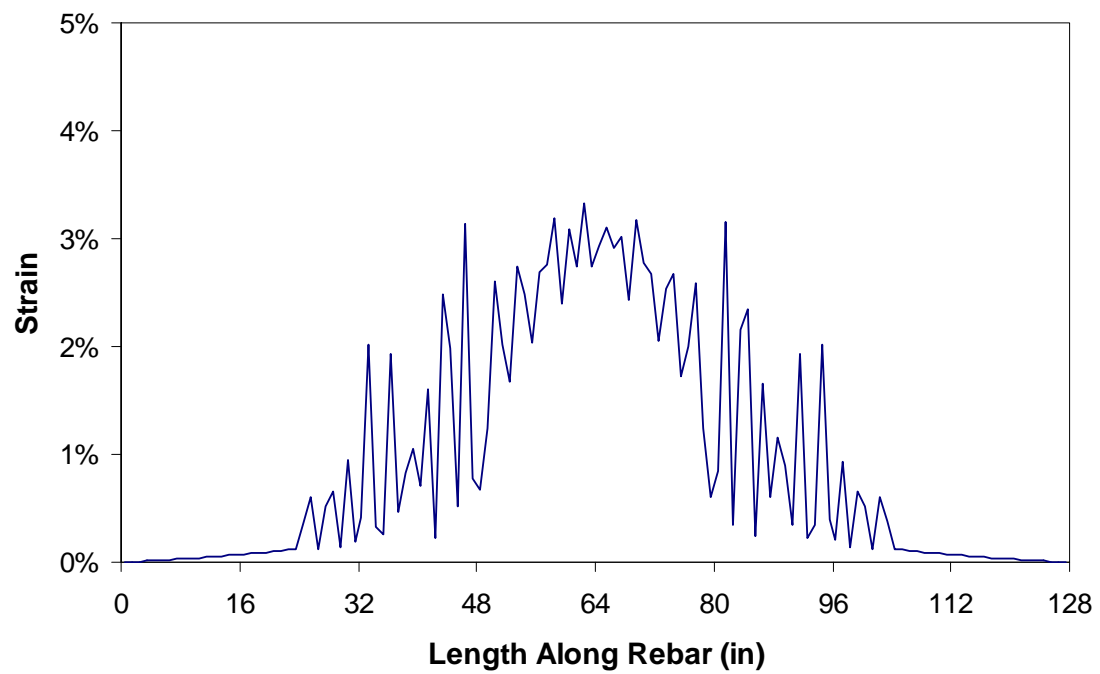


**Fig. 4.38.** Reinforcement strain distribution for 0.5Dow-8

112
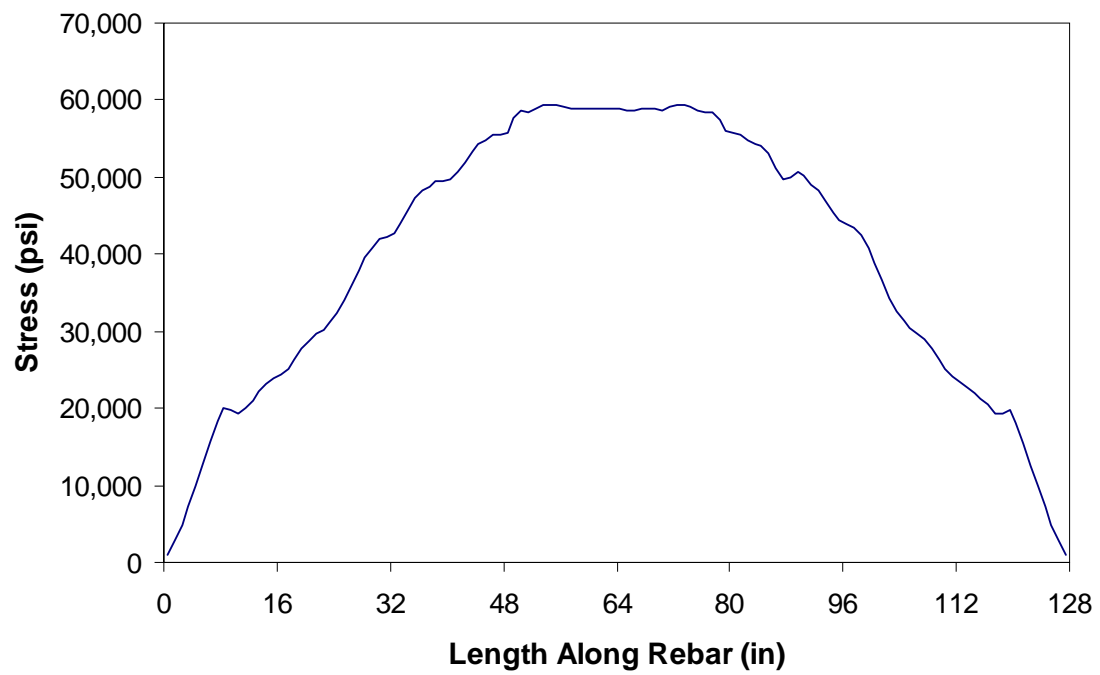
**Fig. 4.39.** Reinforcement stress distribution for Dow-2
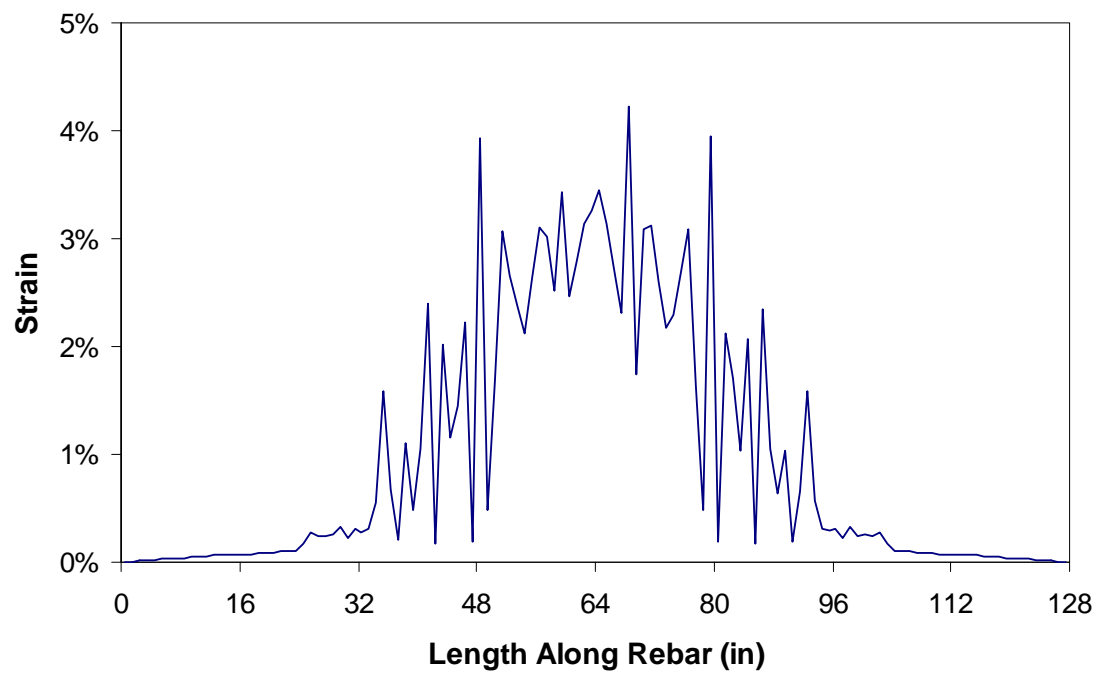


**Fig. 4.40.** Reinforcement strain distribution for Dow-2

113
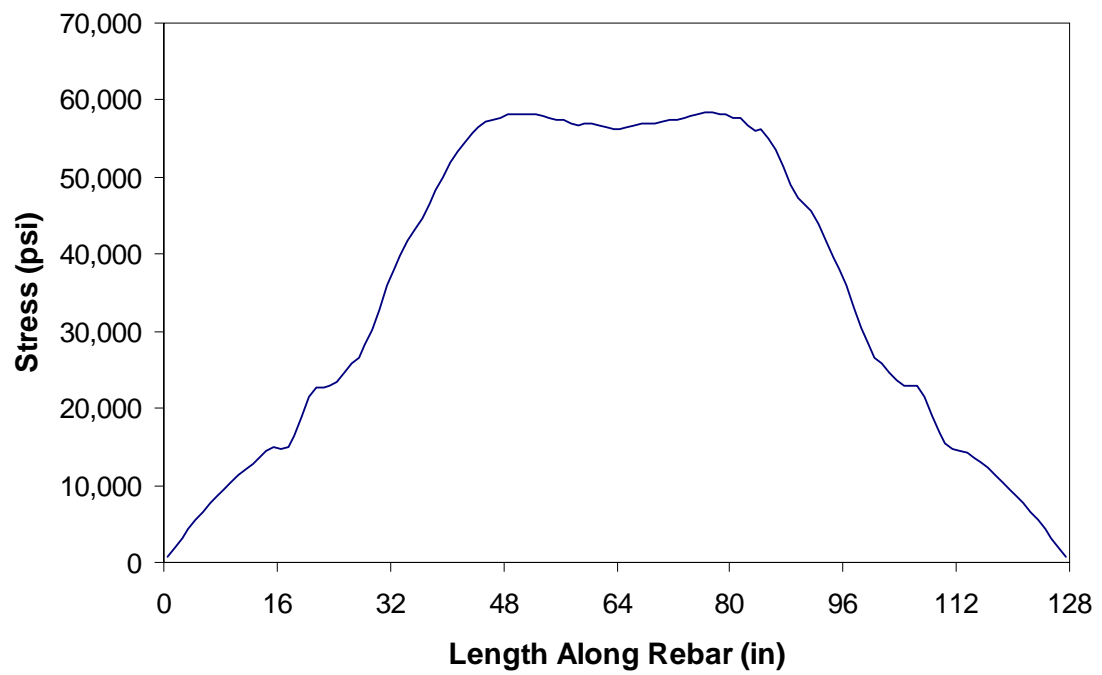
**Fig. 4.41.** Reinforcement stress distribution for Dow-4
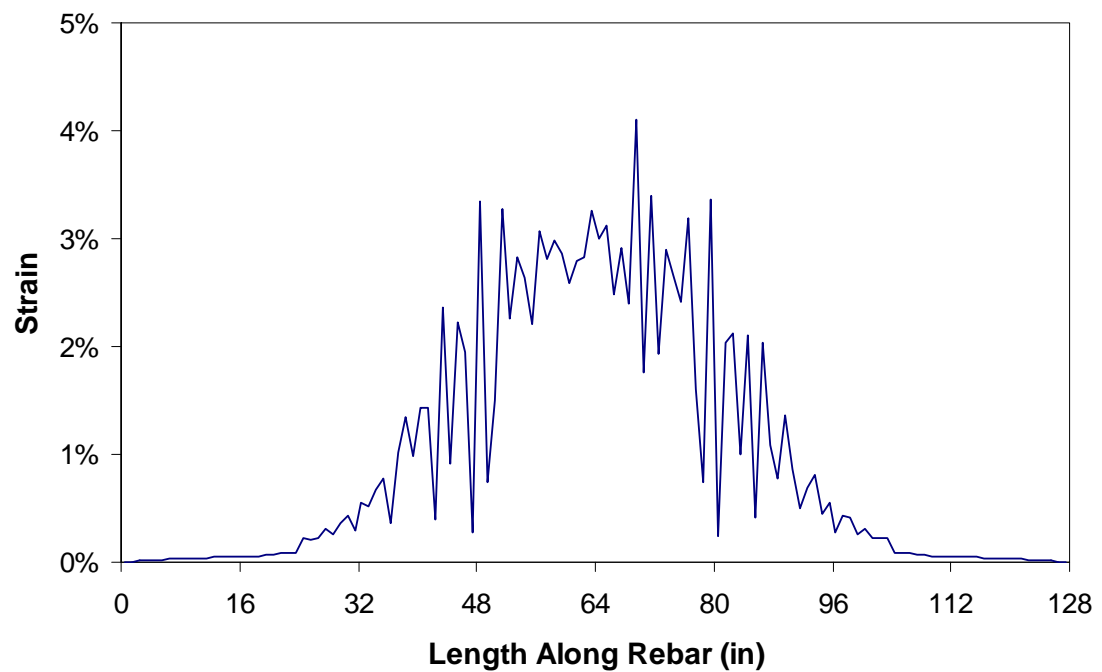


**Fig. 4.42.** Reinforcement strain distribution for Dow-4

114
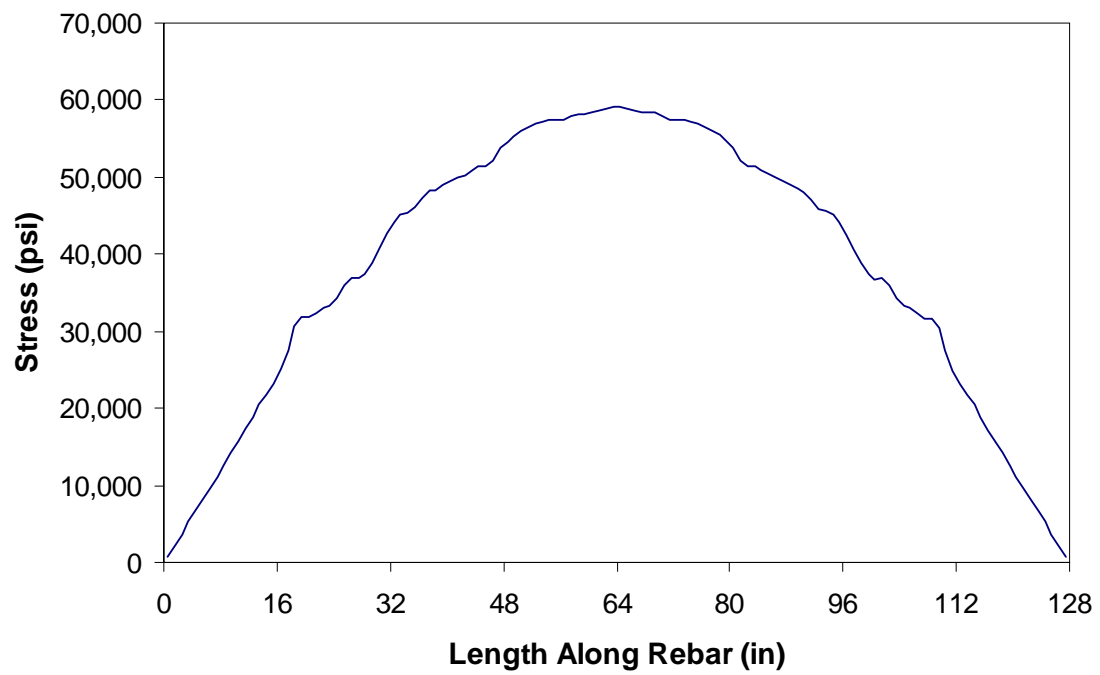
**Fig. 4.43.** Reinforcement stress distribution for Dow-8
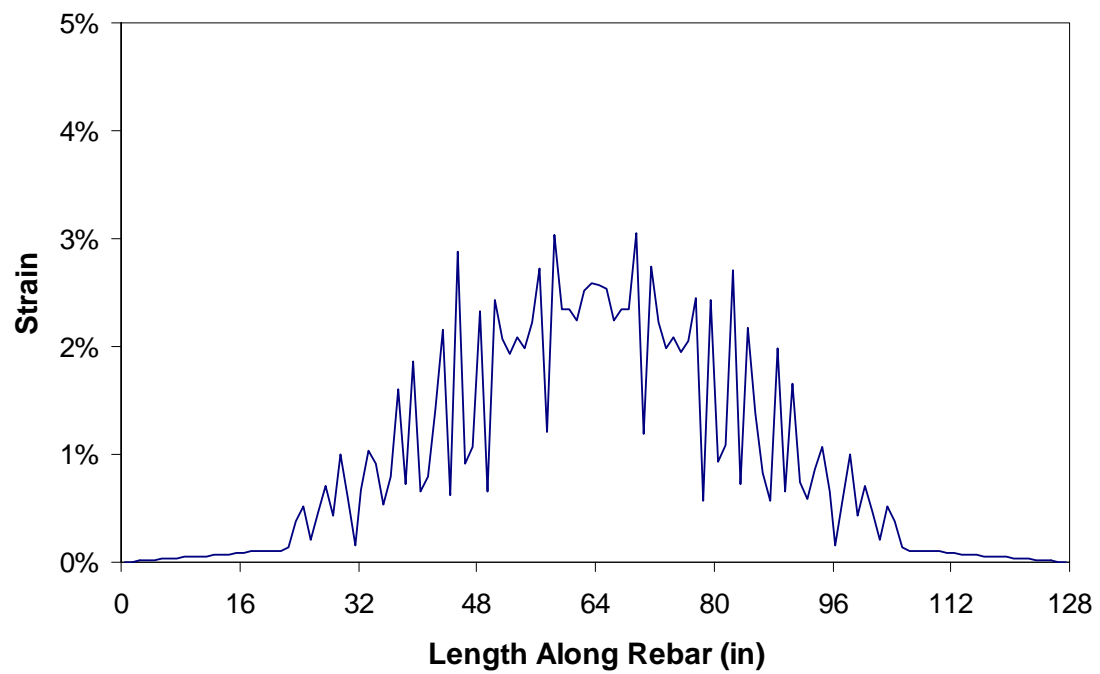


**Fig. 4.44.** Reinforcement strain distribution for Dow-8

115
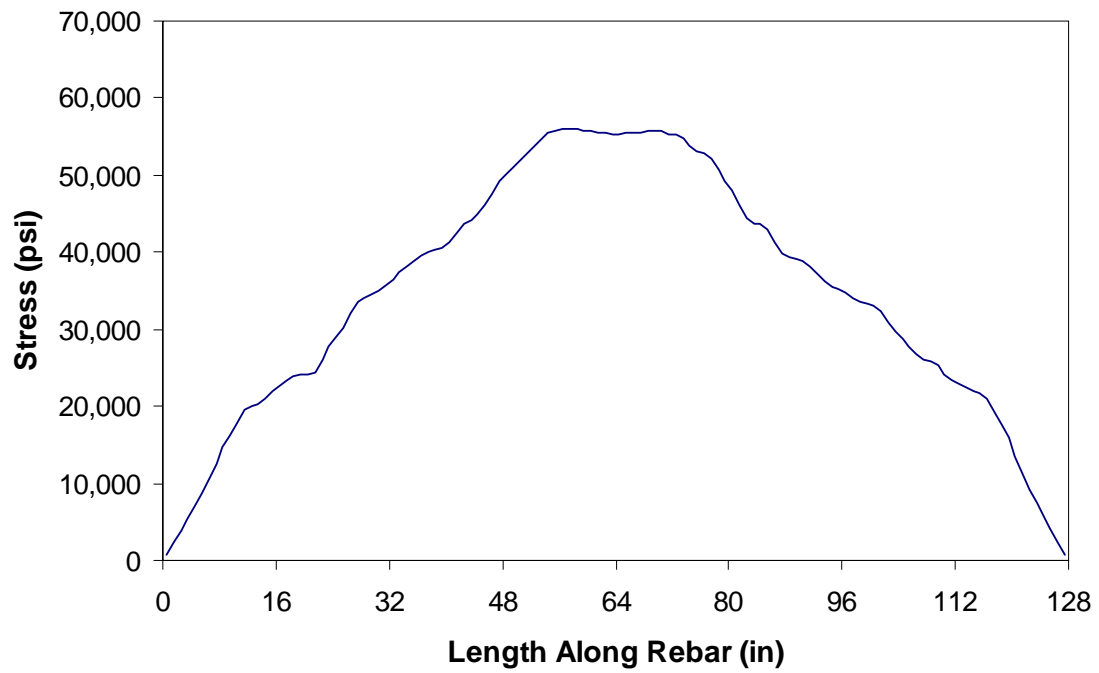
**Fig. 4.45.** Reinforcement stress distribution for 2Dow-2
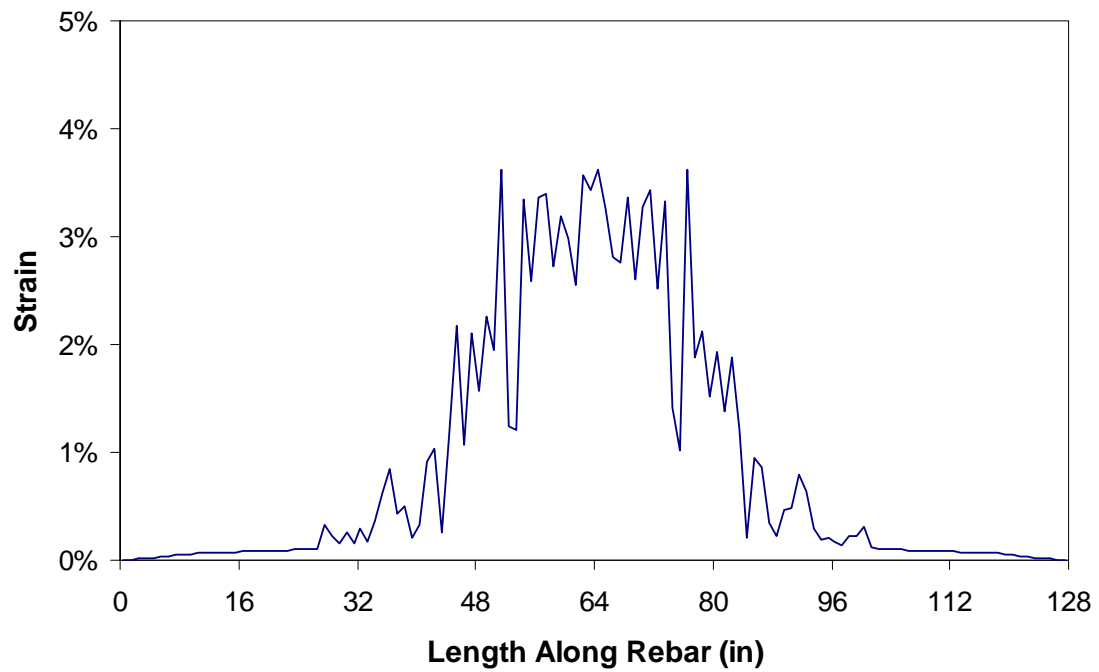


**Fig. 4.46.** Reinforcement strain distribution for 2Dow-2

116
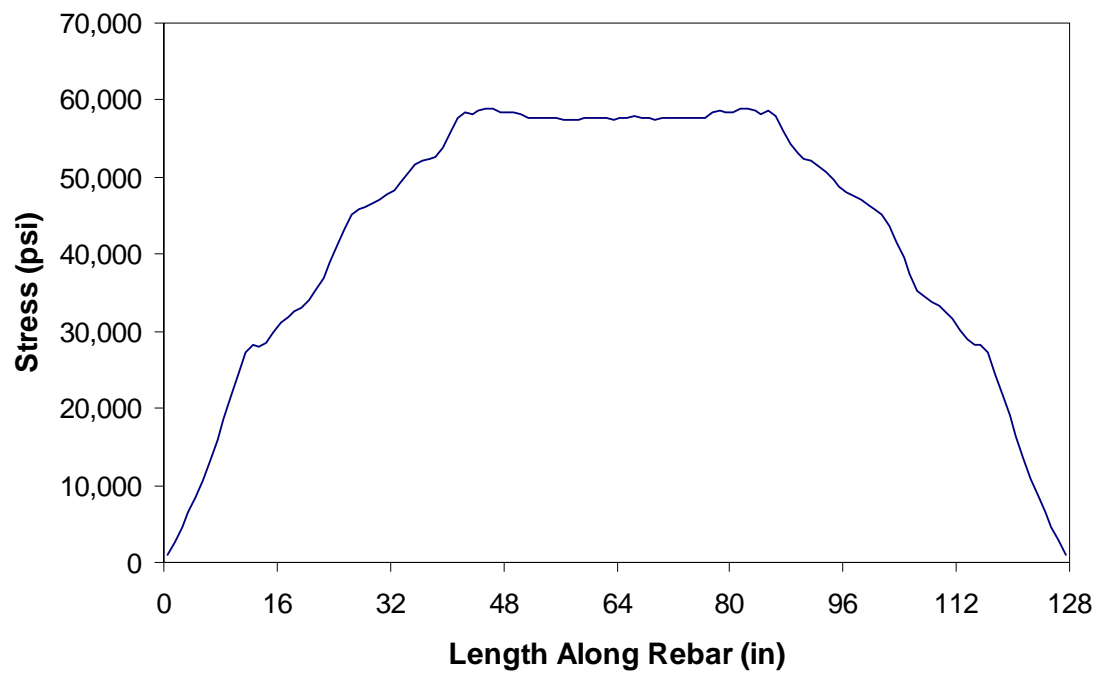
**Fig. 4.47.** Reinforcement stress distribution for 2Dow-4
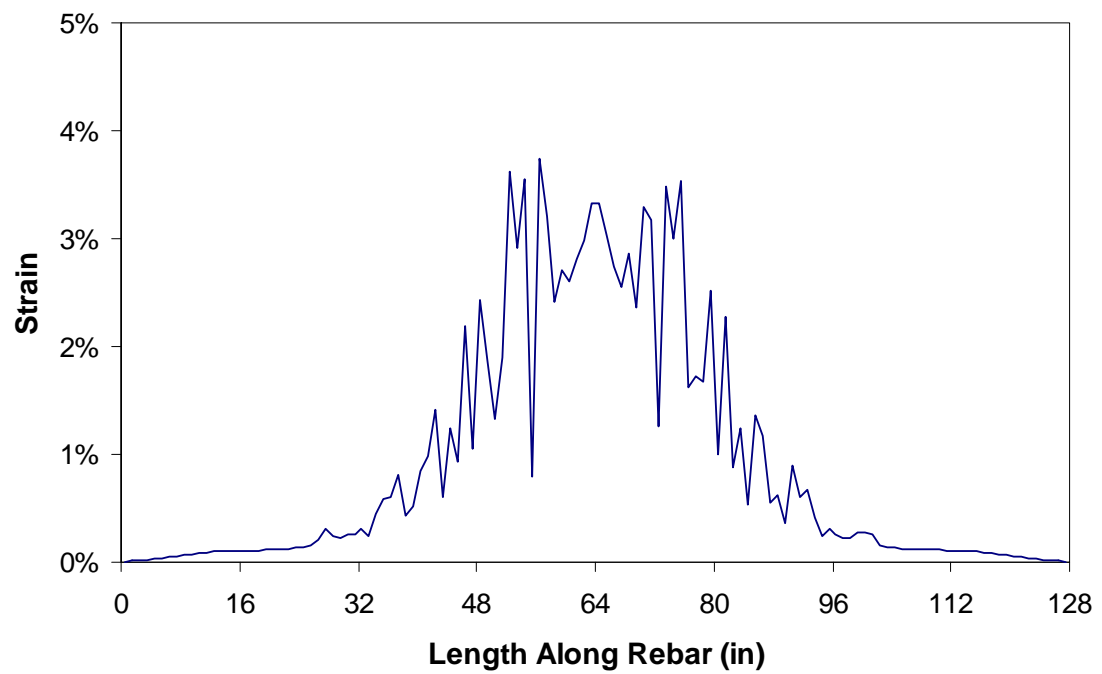


**Fig. 4.48.** Reinforcement strain distribution for 2Dow-4

117
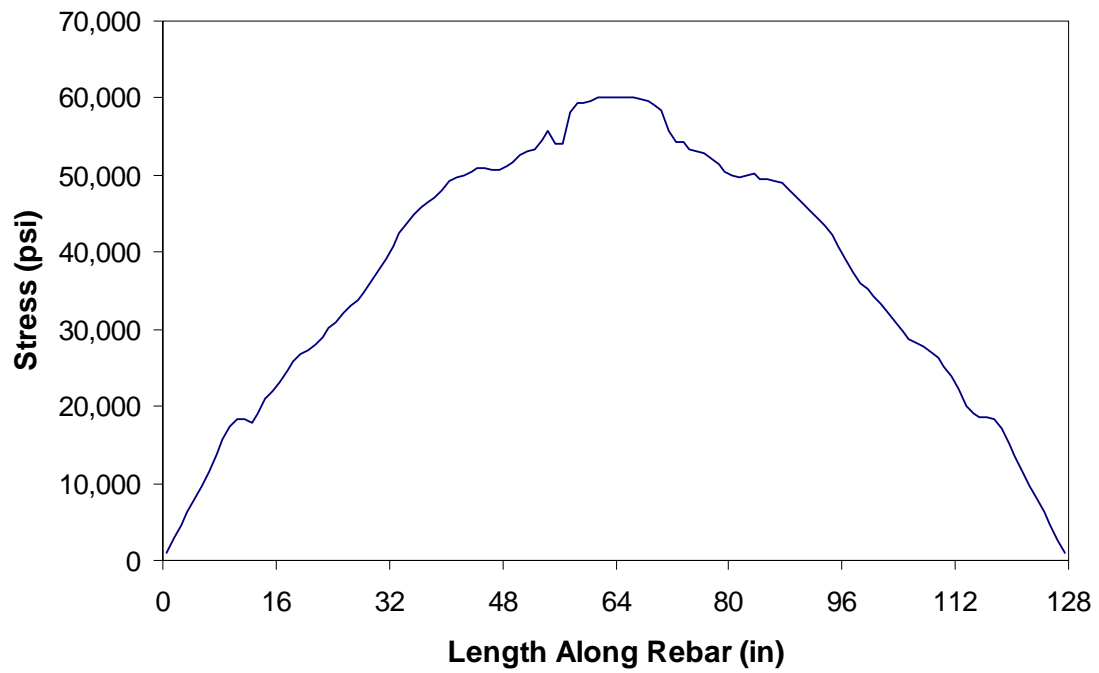
**Fig. 4.49.** Reinforcement stress distribution for 2Dow-8
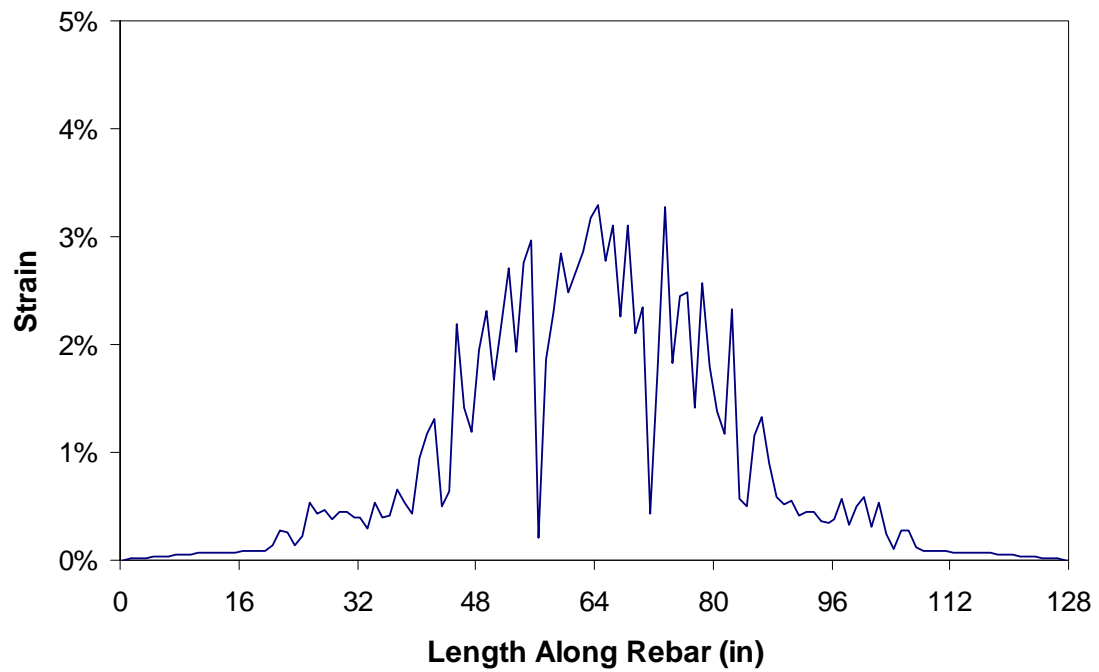


**Fig. 4.50.** Reinforcement strain distribution for 2Dow-8

118

From the previous figures it can be seen that the largest value of strain in the reinforcement occurred in the benchmark model. The stress distributions indicate proper handling of the linear-elastic-perfectly-plastic material behavior. Note that there appears to be much more plastic strain than there is plastic stress; this is actually not true. The plastic strains that do not have corresponding plastic stresses represent elements that yielded prior to ultimate deflection. Due to the tremendous cracking during the formation of the plastic hinge, some of the reinforcement elements received a reduction in stress. However, the corresponding strain reduction was very small because it simply unloaded following the slope of the initial stiffness (i.e. the modulus of elasticity).

Longitudinal strain in concrete subjected to tension caused by flexure can be used to estimate the amount of cracking present in the concrete. The material card used to model the concrete relieves the stress once a crack has appeared and allows the crack to grow, thus resulting in larger strains. The maximum values of strain in the concrete are listed within each figure just below the contour legend. The maximum strain values for the entire history of the model are labeled as the "Max" and "Min" values, whereas the maximum values for the time step shown are the values associated with the "local" label. The following figures present the strain contours at the time of maximum mid-span deflection for each case.
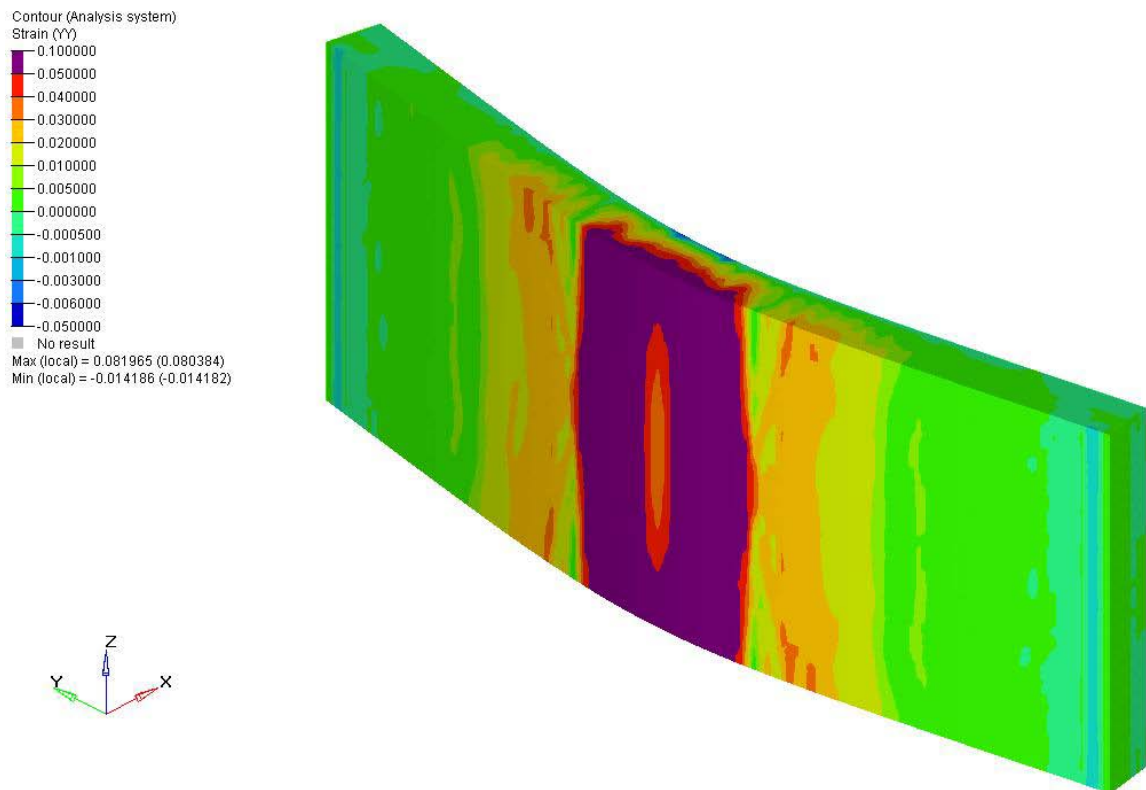
**Fig. 4.51.** Longitudinal strain in concrete for FE-BM

120
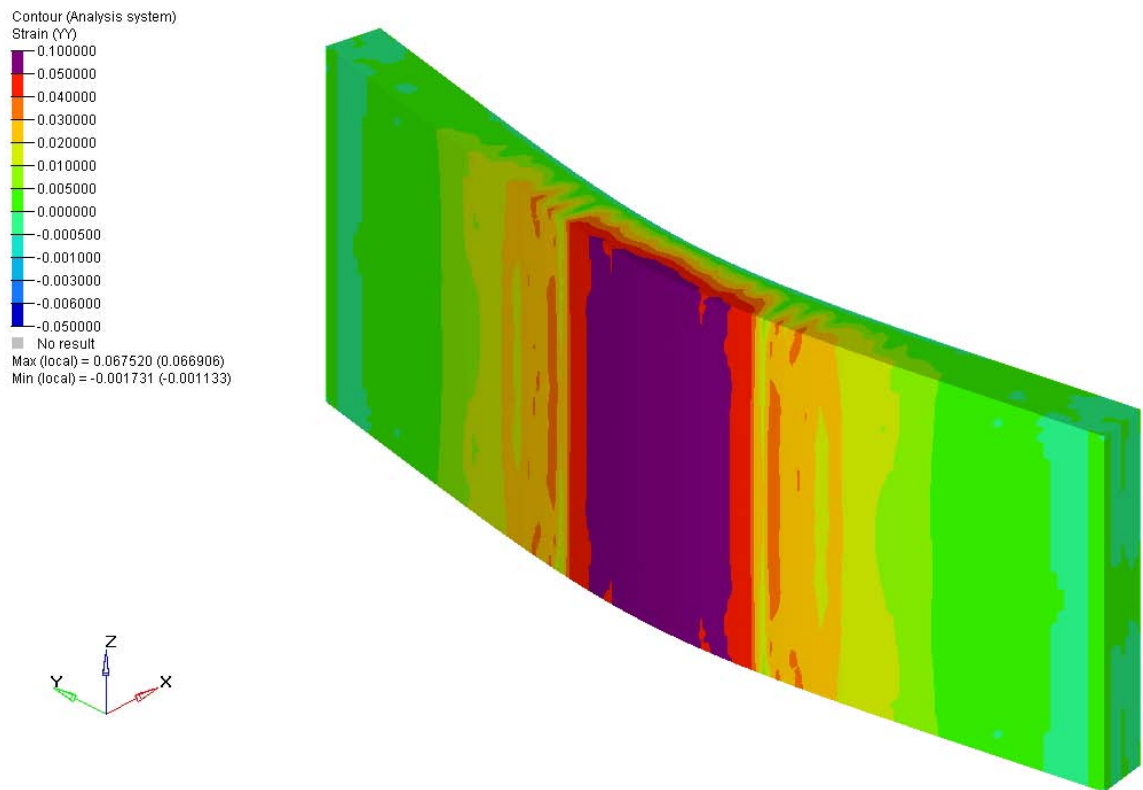
**Fig. 4.52.** Longitudinal strain in concrete for 0.5Dow-2
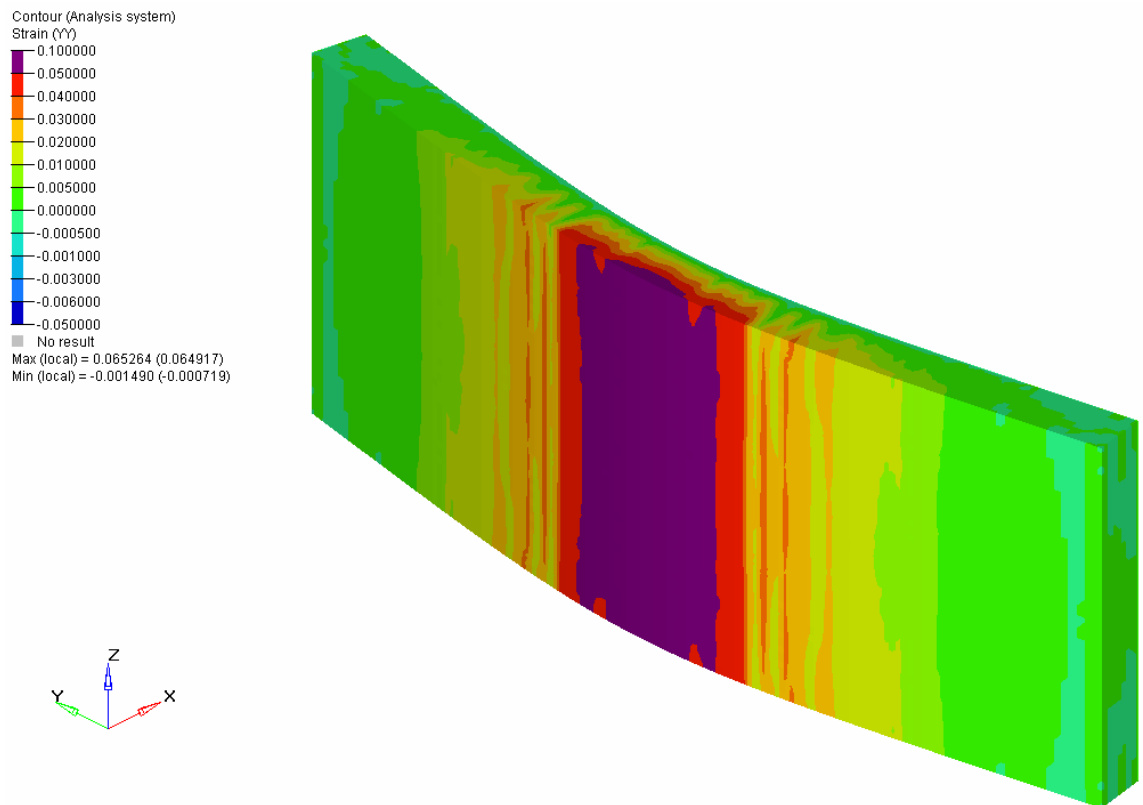
**Fig. 4.53.** Longitudinal strain in concrete for 0.5Dow-4
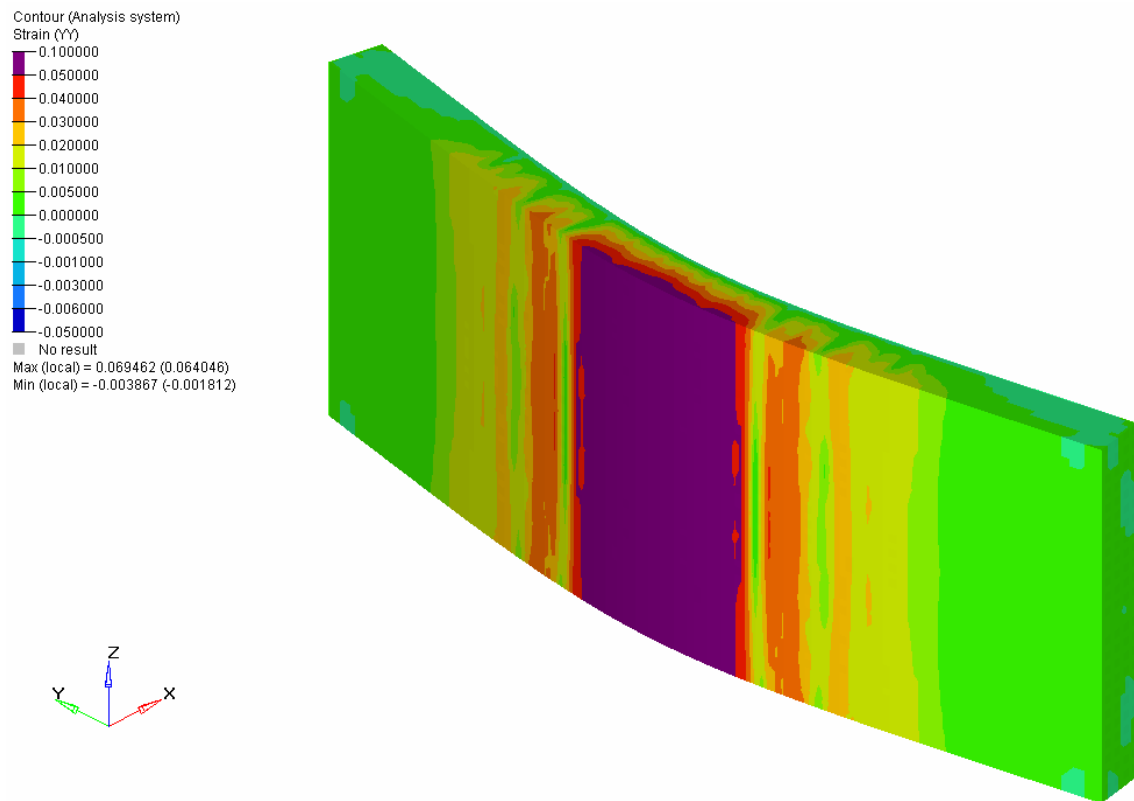
**Fig. 4.54.** Longitudinal strain in concrete for 0.5Dow-8

123
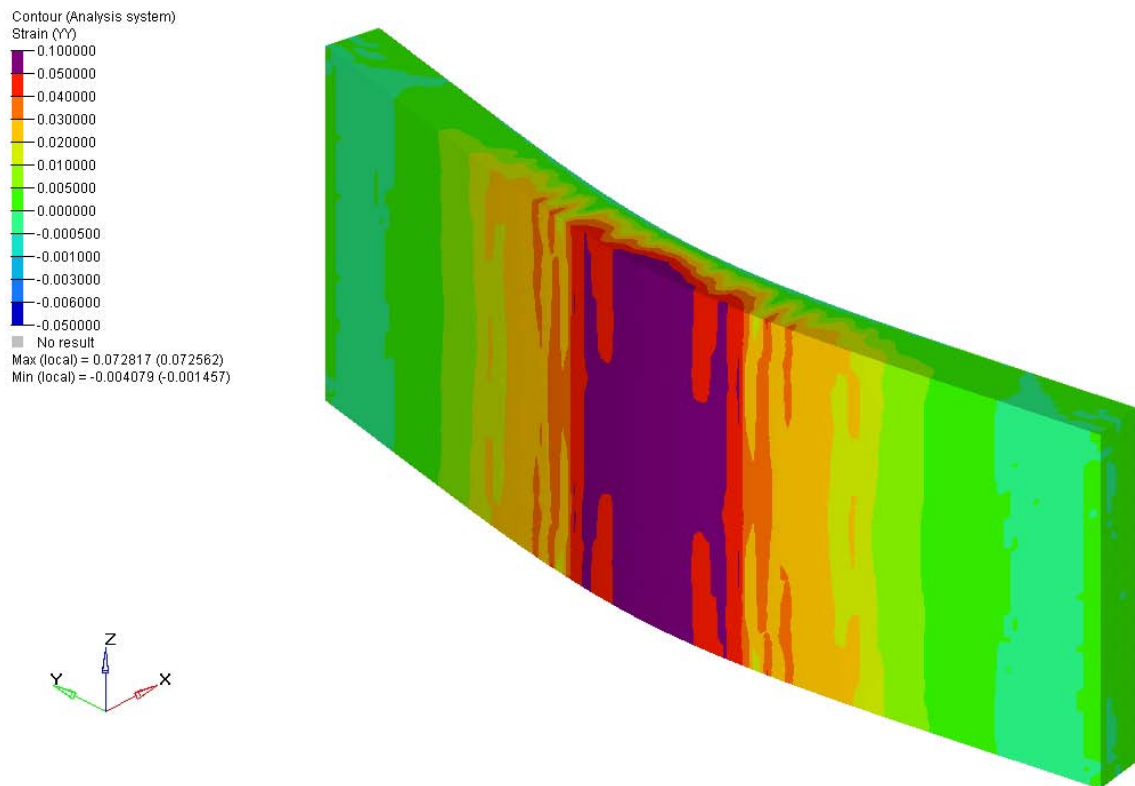
**Fig. 4.55.** Longitudinal strain in concrete for Dow-2
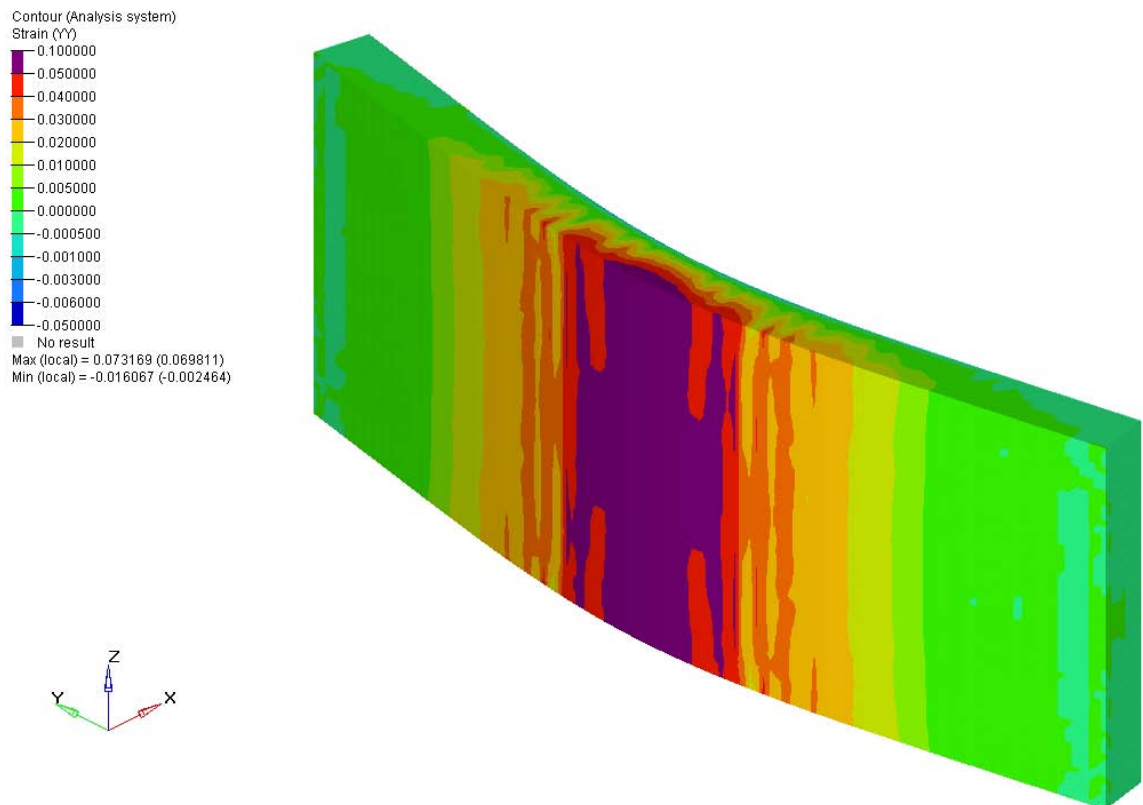
**Fig. 4.56.** Longitudinal strain in concrete for Dow-4
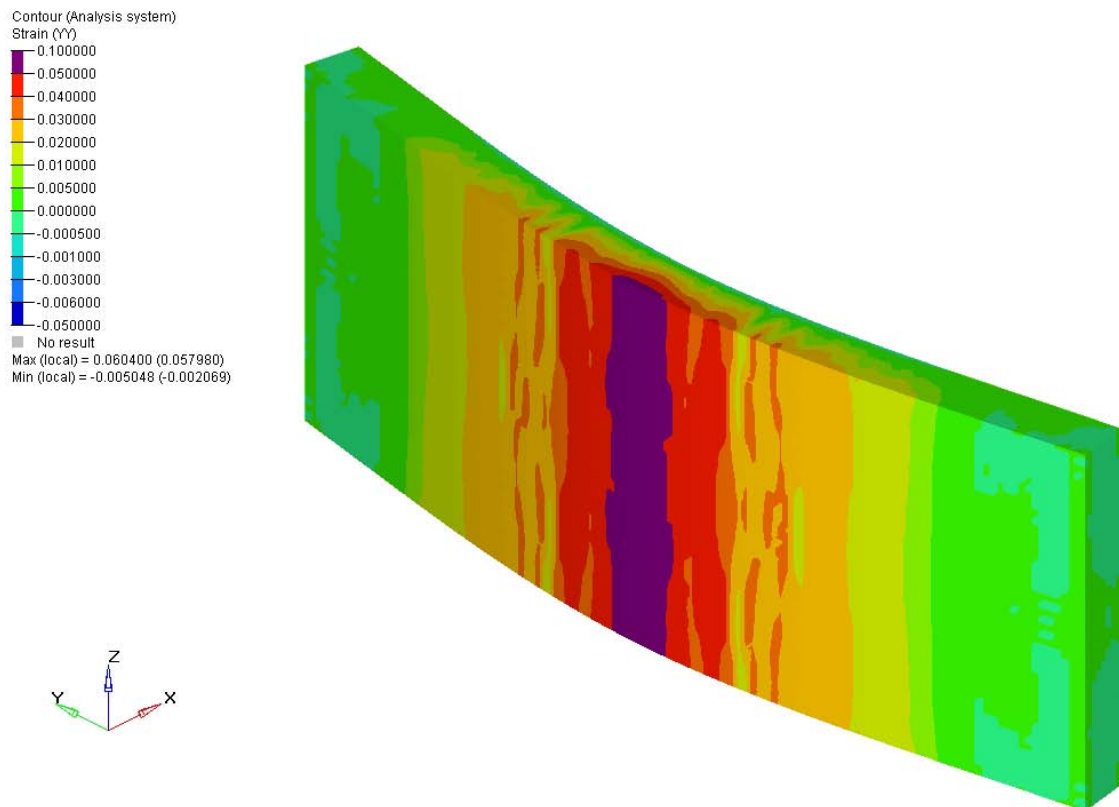
**Fig. 4.57.** Longitudinal strain in concrete for Dow-8
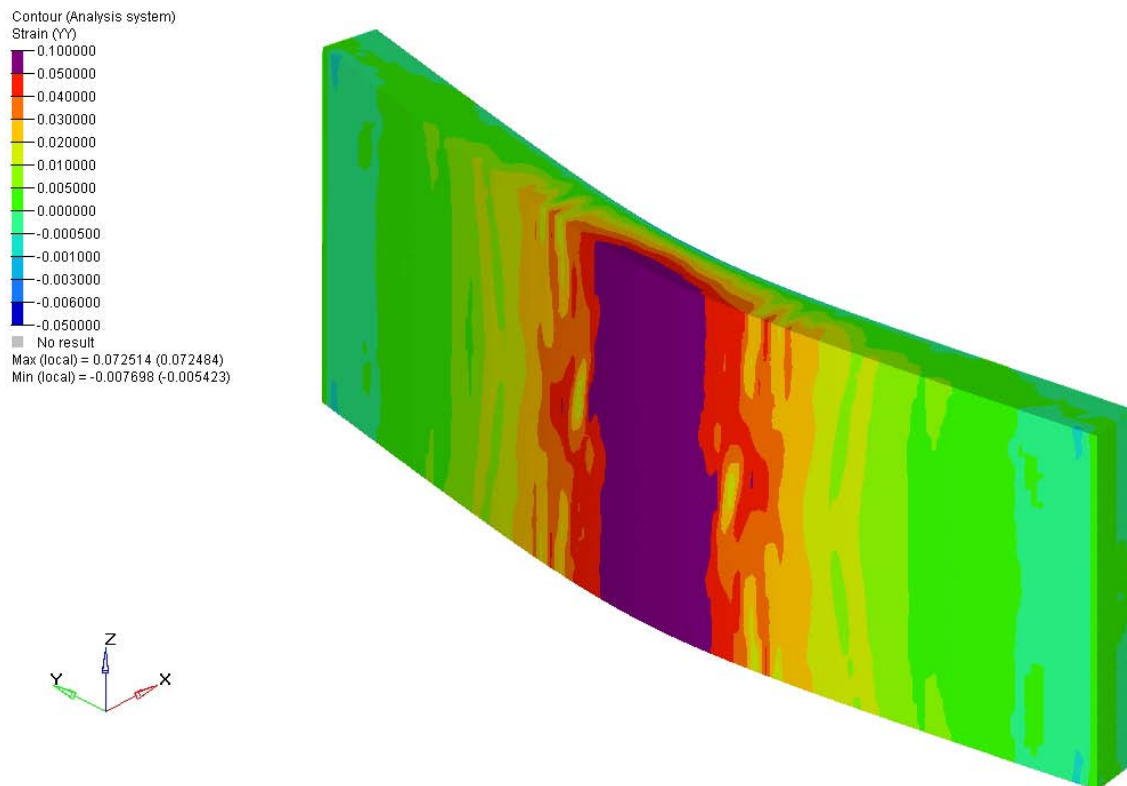
**Fig. 4.58.** Longitudinal strain in concrete for 2Dow-2
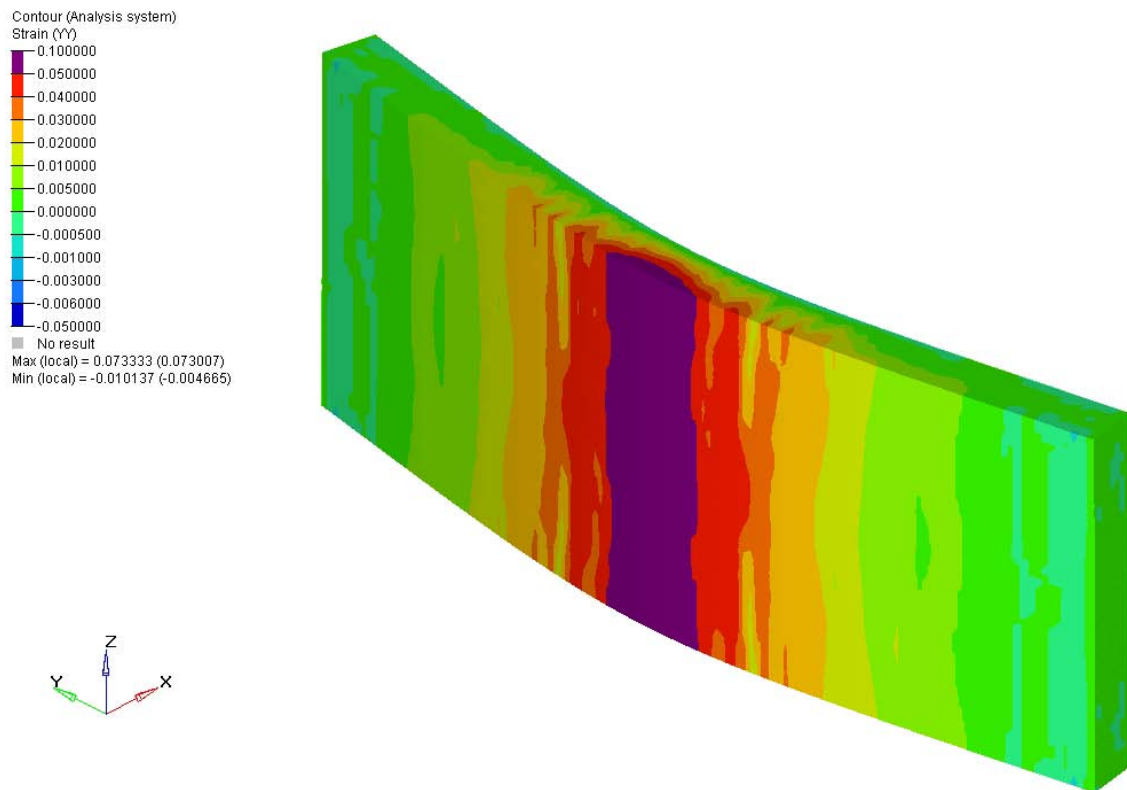
**Fig. 4.59.** Longitudinal strain in concrete for 2Dow-4
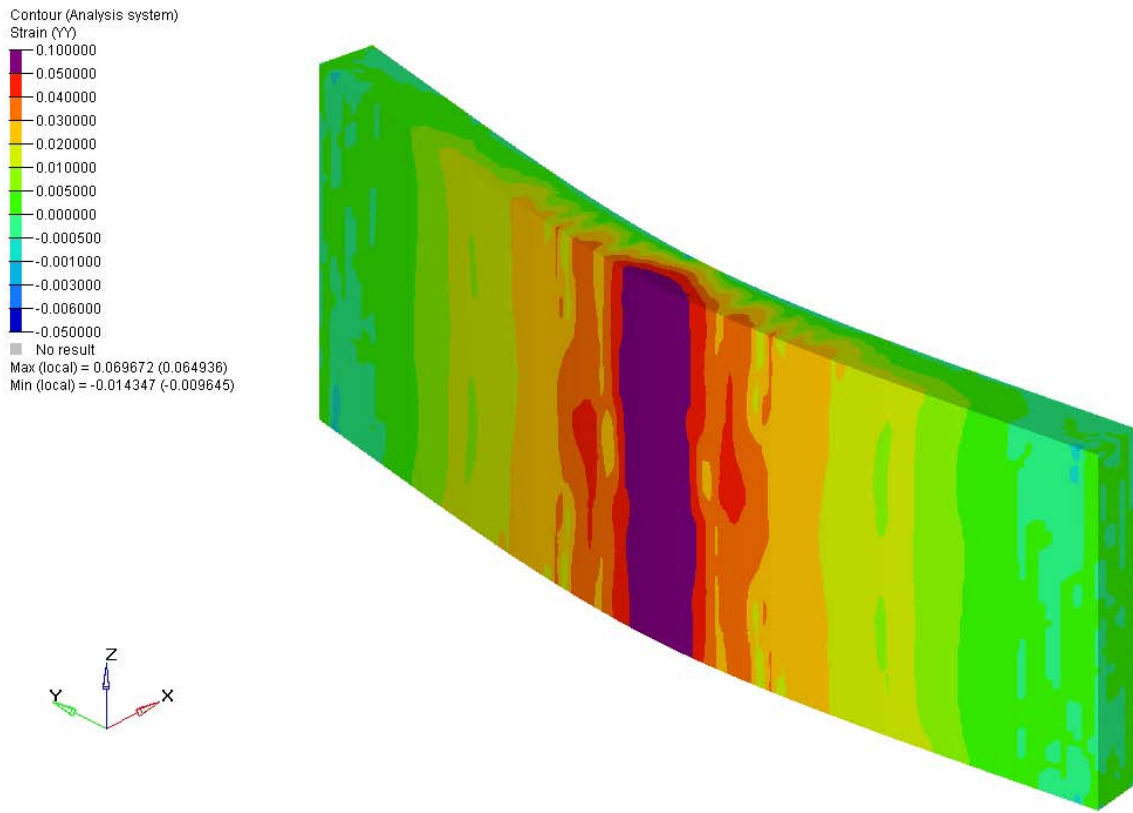
**Fig. 4.60.** Longitudinal strain in concrete for 2Dow-8

In all of the cases where foam was present, it can be seen that the maximum tensile strain in the concrete was less than in the case where there was no foam. However, the models still show significant cracking for all cases and the subsequent formation of plastic hinges at mid-span. The behavior of the FE-BM model compares well with the behavior observed in testing. The addition of foam did not alter the nature of the response but did add resistance to the system. The strain contours seen in the concrete also show excellent correlation with the respective reinforcement stress and strain distributions for each case.

129

### 4.8.3 Deflection Plots

This section provides various deflection histories generated from each of the models. Figure 4.61 presents a comparison of the FE-BM mid-span deflection to the mid-span deflections of Wall 2 and Wall 3 in Detonation 3. The figures that follow it present mid-span deflection comparisons made between the FE-BM model and the other FE models.

From Figure 4.61 it can be seen that the FE-BM model provides a reasonable average of the deflections seen in Wall 2 and Wall 3. Because of the non-uniform pressure distribution recorded in Detonation 3, it was determined that the FE-BM accurately simulated the behavior of the wall.
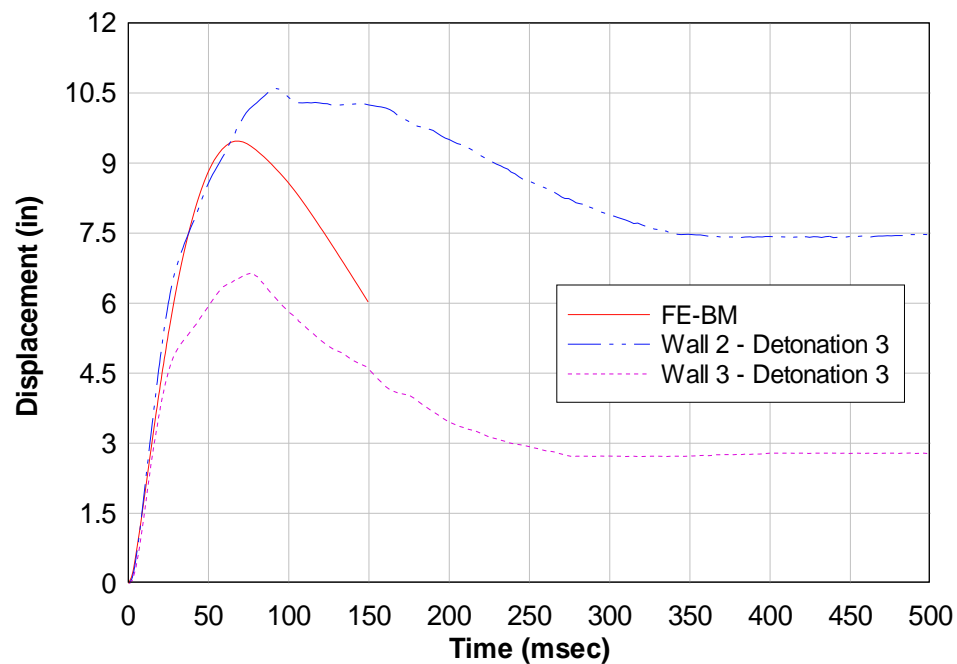


**Fig. 4.61.** Mid-span deflection comparison of FE-BM with Detonation 3 data
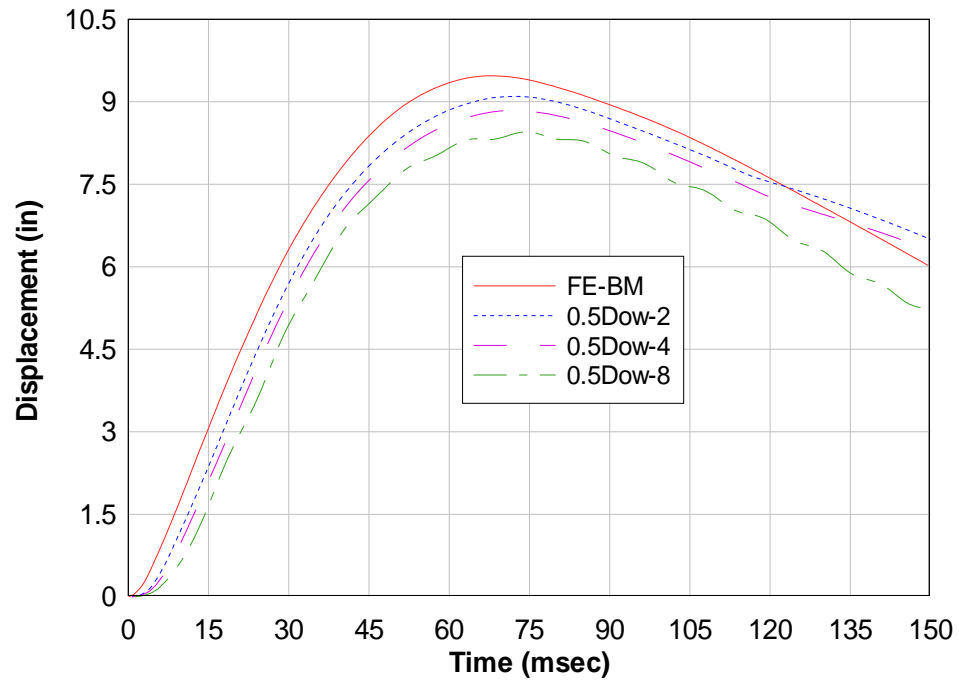
**Fig. 4.62.** Mid-span deflection comparison for 0.5Dow cases
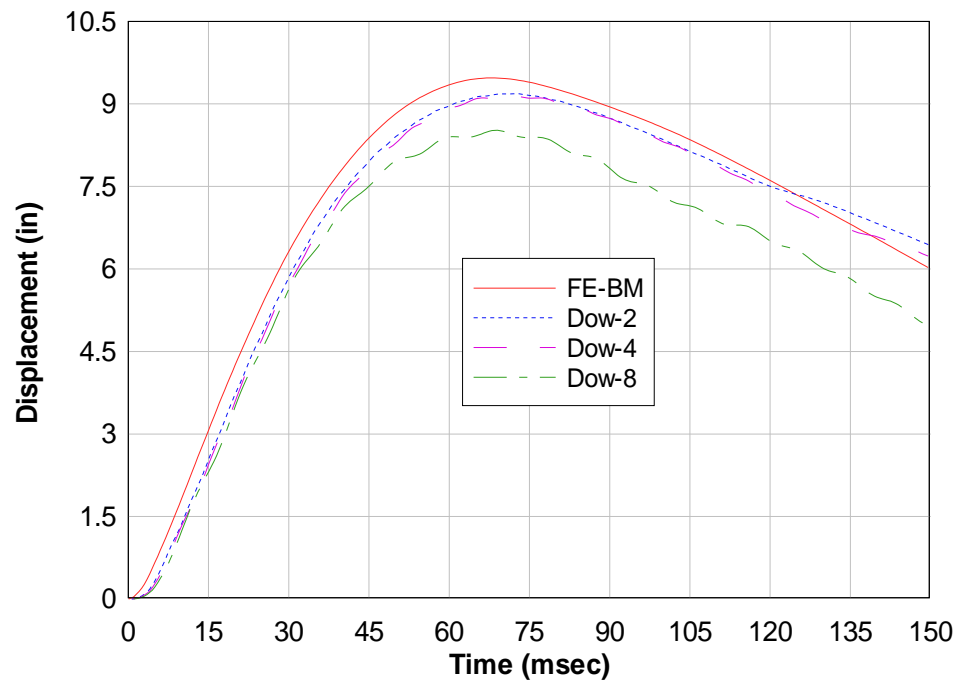


**Fig. 4.63.** Mid-span deflection comparison for Dow cases

131
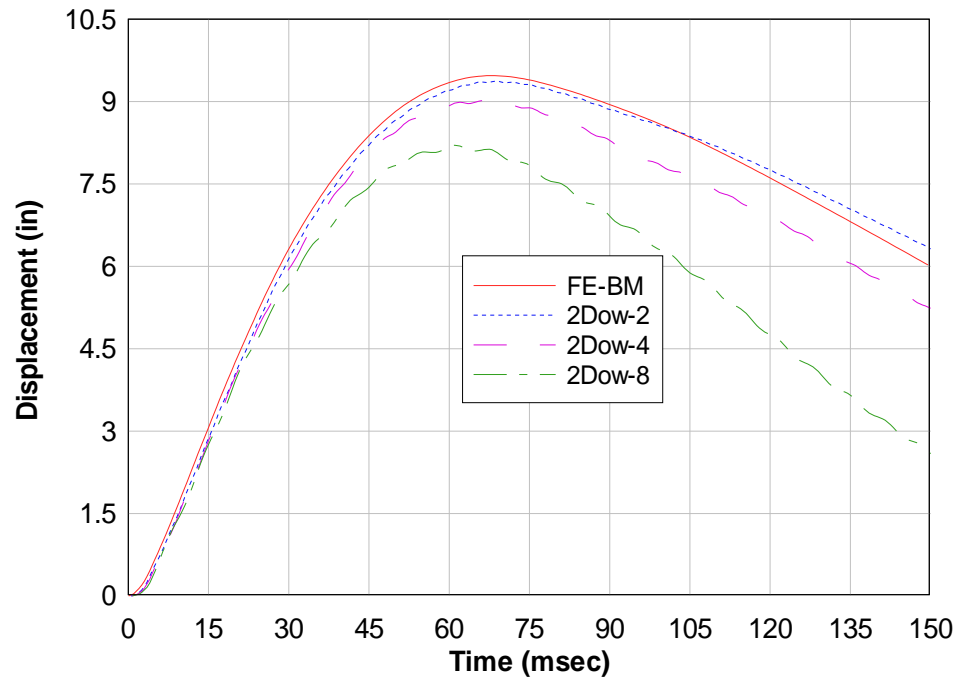
**Fig. 4.64.** Mid-span deflection comparison for 2Dow cases

Comparison of the mid-span deflection of each foam case to that of the FE-BM model shows that the addition of foam to the system decreases the total deflection. To help visualize the effects of different material properties, for each type of foam, the maximum mid-span deflections were plotted with respect to the corresponding thickness of foam. These plots are shown in Figure 4.65. The plots reveal a trend, which proposes that for thin layers of foam, soft foam performs better; whereas, for thick layers of foam, it appears that stiff foam performs better. Because it is unlikely that 8 inches of foam would be used in construction, this comparison essentially indicates that for a reasonable thickness of foam, softer foams perform best.
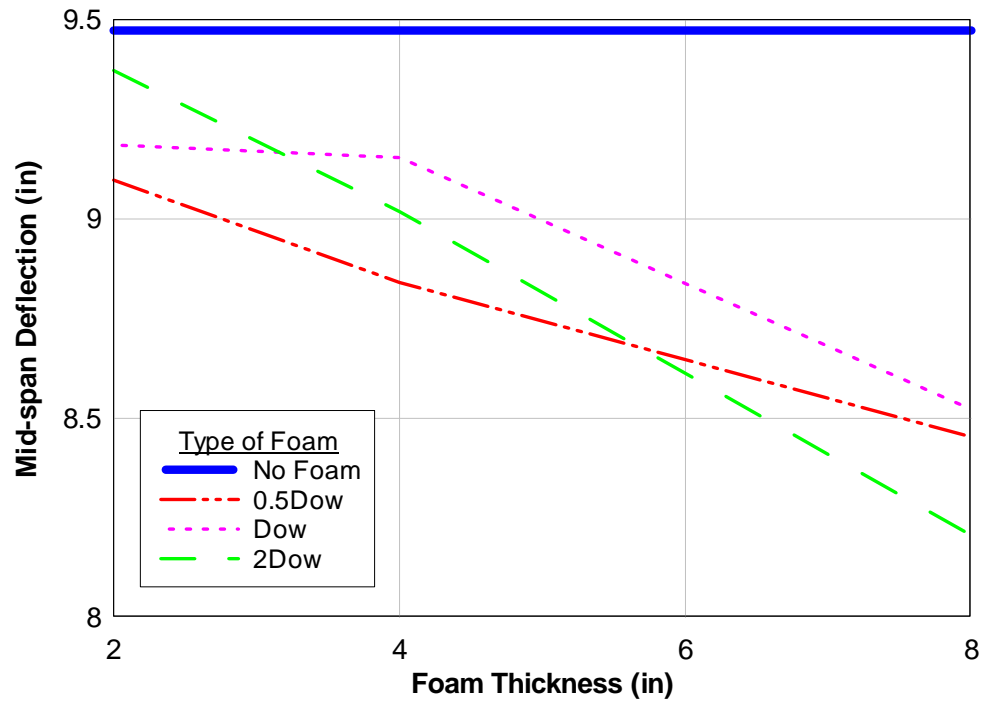
**Fig. 4.65.** Mid-span deflection versus foam thickness for all cases

The relative deflection of the foam was found to be greatest at mid-span, although in some of the models, the crushing of the foam was almost uniform. For each case, the local deflection of the foam through the thickness at mid-span was recorded and plotted. This deflection was then non-dimensionalized by dividing each deflection history by the original thickness of the foam. This provided a history of the average compressive strain through the thickness of the foam at mid-span. Care should be taken, however, in visualizing this as strain since this assumes strain to be uniform through the thickness when in fact it is not. Inspection of the deformed geometry showed that as the thickness increased, the compressive strain through the thickness became less uniform. The following three figures show the average compressive strain responses of the foam at mid-span for each case.
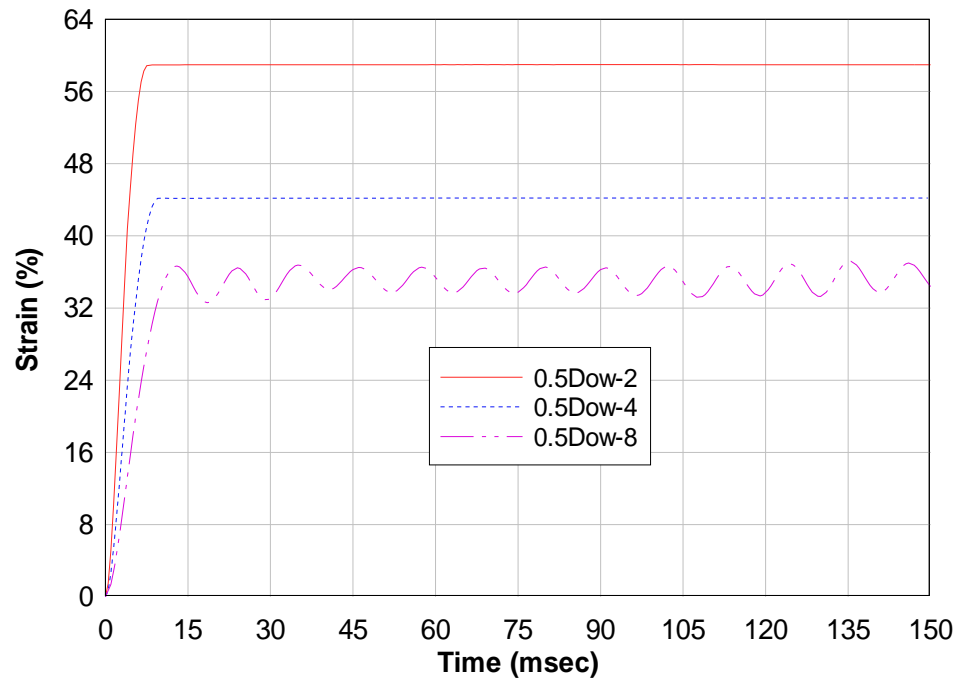
**Fig. 4.66.** Average compressive strain of foam at mid-span for 0.5Dow cases
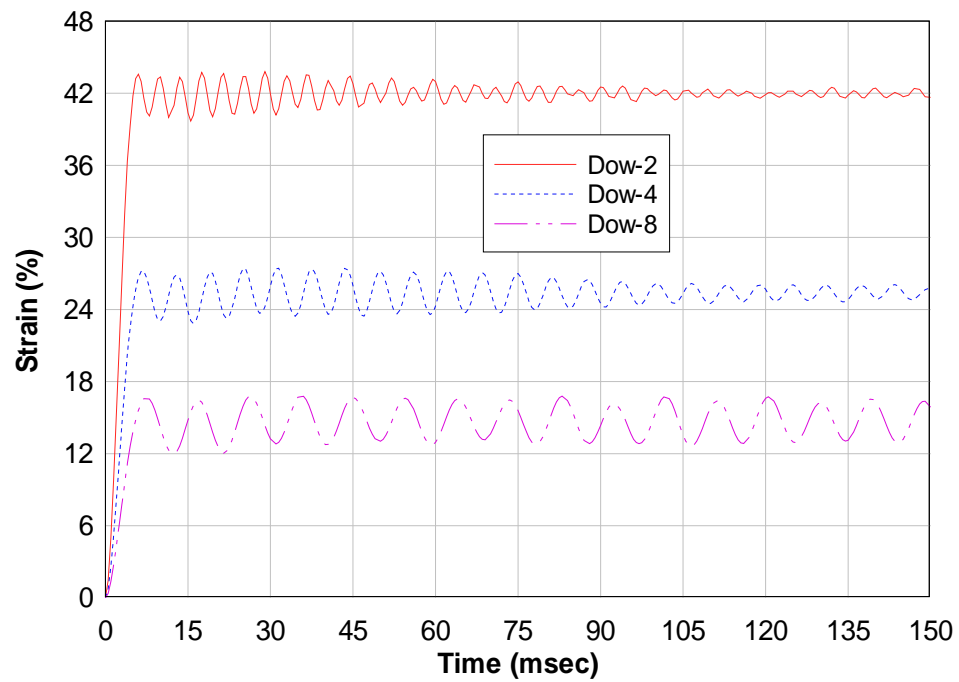


**Fig. 4.67.** Average compressive strain of foam at mid-span for Dow cases

134
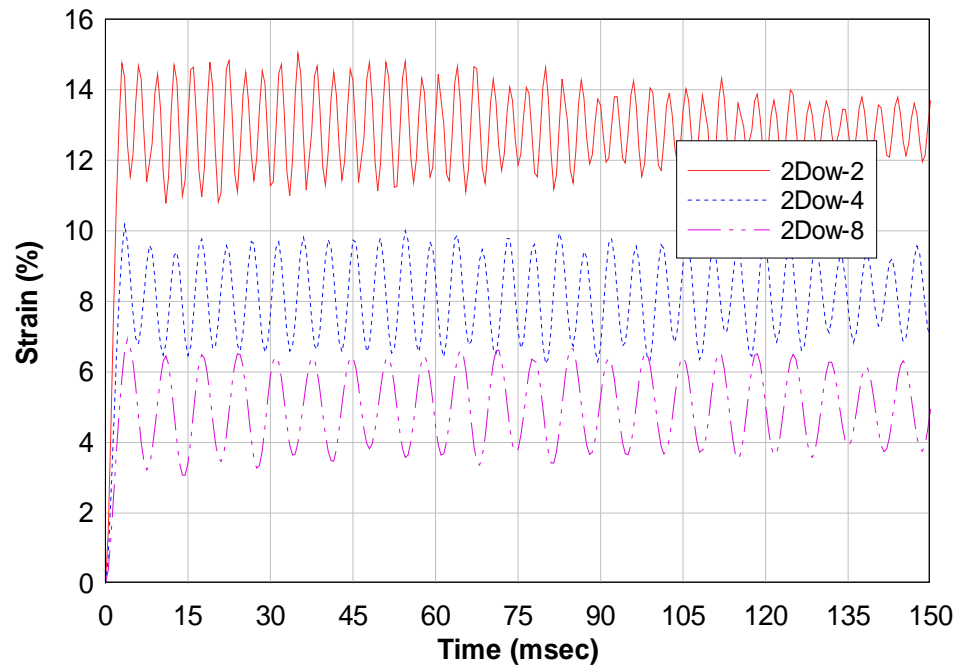
**Fig. 4.68.** Average compressive strain of foam at mid-span for 2Dow cases

Inspection of the previous figures confirms two things: 1) as the foam becomes stiffer, the average strain in the foam decreases, and 2) as the foam becomes thicker, the average strain in the foam decreases. Intuitively, these results are reasonable. The non-uniformity of the strain in the foam will be discussed further when the results of the models in Chapter 5 are compared to the FE results.

CHAPTER 5

ENGINEERING-LEVEL MODELS

**5.1 Introduction**

This chapter begins with a definition of a standard engineering-level (EL) model, and gives examples that are currently being used for blast-resistant design. An explanation of the theory behind these models is also presented, along with a detailed description of one of the most common solution methods. Finally, the deflection predictions made by one of the currently available models will be presented and discussed.

**5.2 Overview**

In general, the purpose of an EL model is to provide design engineers with a practical tool for conservatively designing a given system. In the case of structural systems subjected to blast loads, the model must, at a minimum, allow the engineer to apply an impulsive load to a structural system of his or her choice. Beyond that, models may incorporate many useful tools to simplify and expedite the design process.

Two commonly used EL models in the area of blast design are the Single-Degree-of-Freedom Blast Effects Design Spreadsheets (SBEDS) and the Wall Analysis Code (WAC). SBEDS were developed by the U.S. Army Corps of Engineers (USACE) Protective Design Center (PDC), while WAC was developed by the U.S. Army Engineer

Research and Development Center (ERDC). Both programs are capable of predicting the dynamic structural response of various structural elements subjected to blast loads. Both programs possess the capability to generate pressure-time data based on a given standoff distance and equivalent weight of TNT.

Programs such as SBEDS and WAC are based on single-degree-of-freedom (SDOF) methodology and are used to analyze complex systems possessing an infinite number of degrees of freedom. The following section describes the fundamental concepts of SDOF methodology. Finally, a proposed nonlinear 2-DOF EL model is presented, which was developed for the purpose of examining the multi-wythe masonry walls more thoroughly.

## 5.3 SDOF Methodology

In reality, all structural systems possess an infinite number of degrees of freedom. A SDOF system is one in which the displacement history can be completely described by a single coordinate. A general SDOF system, along with its dynamic free body diagram, is shown in Figure 5.1. By summing the forces, the equation of motion for this system is found to be

$$m\ddot{y} + c\dot{y} + ky = F(t) \tag{5-1}$$

where $m$ is the mass, $c$ is the damping constant, $k$ is the spring constant (or stiffness), $F(t)$ is the forcing function, and $y$, $\dot{y}$, and $\ddot{y}$ are the displacement, velocity, and acceleration of the mass. However, this equation can only be applied to systems for which the behavior can be adequately described in terms of a single degree of freedom.

137
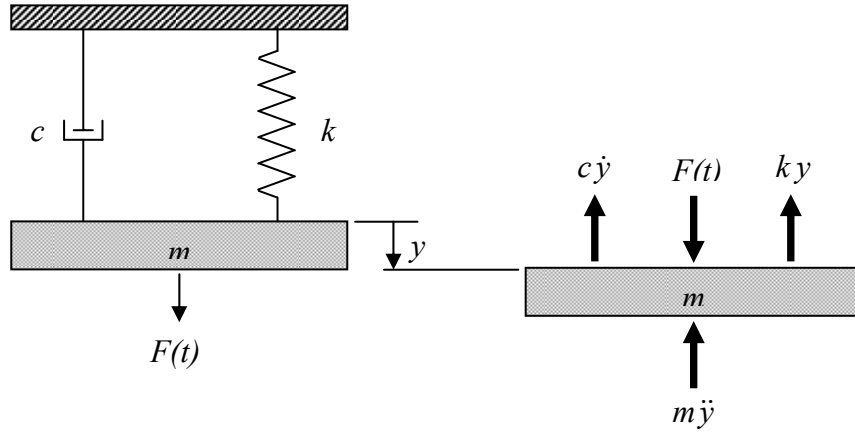
**Fig. 5.1.** Example of a SDOF system

To apply Equation 5-1 to a generic structural system, a slight modification is necessary. This modification is shown in Equation 5-2 as follows:

$$m_e \ddot{y} + c_e \dot{y} + k_e y = F_e(t) \qquad (5\text{-}2)$$

where $m_e$, $c_e$, $k_e$, and $F_e(t)$ are the effective mass, damping constant, stiffness, and forcing function of the real system, respectively, which are calculated based on an assumed deflected shape known as the shape function. This modification accounts for the effects of distributed mass and distributed load in the system.

The general equation of motion for the equivalent system will now be derived. Further details can be found in the *User's Guide for SBEDS* (2006). Consider an arbitrary beam of length *l* with a shape function $\psi(x)$ that describes the deflected shape at all points *x* along the length of the beam. Now, assume the beam has an arbitrary mass per unit length of $\overline{m}$ and an arbitrary force per unit length of *v(x)*. To rewrite the equation of motion for the equivalent system in terms of the real system parameters, a multiplication factor will be defined for mass, damping, stiffness, and load such that

138

$$K_M = \frac{m_e}{m} \tag{5-3a}$$

$$K_d = \frac{c_e}{c} \tag{5-3b}$$

$$K_S = \frac{k_e}{k} \tag{5-3c}$$

$$K_L = \frac{F_e}{F} \tag{5-3d}$$

where $F = vl$ and $m = \overline{m}\,l$ are the total force and total mass of the real system. Therefore, Equation 5-2 can be rewritten as

$$K_M m \ddot{y} + K_d c \dot{y} + K_S k y = K_L F(t) \tag{5-4}$$

This can be simplified further because $K_S$ can be shown to be equal to $K_L$; $K_d$ is taken as being equal to $K_L$ even though this is not mathematically correct. This discrepancy is tolerable since damping plays a minor role in the peak dynamic response for impulse loads. Therefore, the equation of motion is rewritten as

$$K_M m \ddot{y} + K_L c \dot{y} + K_L k y = K_L F(t) \tag{5-5}$$

The effective mass, $m_e$, and effective force, $F_e$, are calculated from the following equations:

$$m_e = \int_0^l \overline{m}\, \psi^2(x)\, dx \tag{5-6}$$

$$F_e(t) = \int_0^l v(x)\psi(x)\, dx \tag{5-7}$$

If Equation 5-5 is divided through by $K_L$, and the load mass factor is defined as

$K_{LM} = {K_M}\big/{K_L}$ , then the equation of motion can be further simplified to the following:

139

$$K_{LM}m\ddot{y} + c\dot{y} + ky = F(t) \tag{5-8}$$

Biggs' text, *Introduction to Structural Dynamics* (1964), provides tables giving values of $K_{LM}$ for typical structural applications including one-way and two-way slabs. It should be noted that, although the current work is based on a simply supported beam model, these factors can be developed for virtually any structure.

For systems subjected to blast loads, the primary interest is usually the peak deflection, which is generally the first peak in the displacement history. For this reason, damping can be ignored without appreciable error because it has very little effect during the initial response. As discussed in Chapter 2, a typical pressure-time plot for a blast load is approximated as shown in Figure 5.2. A simple but conservative approach for
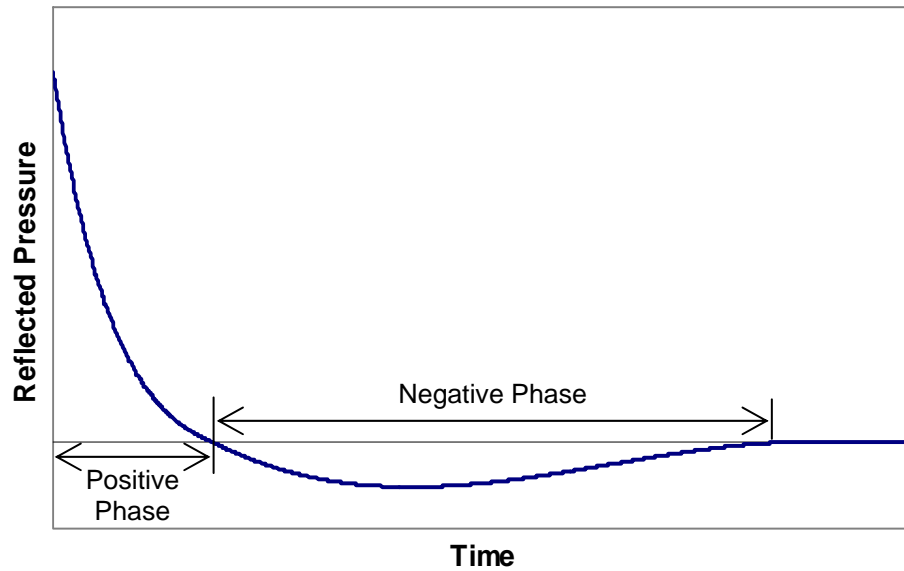


**Fig. 5.2.** Arbitrary blast load

designing structures to resist blast loads is to ignore the negative phase and then to approximate the positive phase as an equivalent-impulse triangular load with the same

initial peak pressure. This approach is most applicable to stiff structures. This is due to the fact that flexible structures possess long natural periods, which allows more of the negative phase to be applied early with respect to the time required to reach the first peak displacement. This allows the negative phase to apply suction to the responding structure, resulting in lower deflections. In the design arena, ignoring the negative phase can be a viable option, even for flexible structures, since it will yield conservative results. However, it is imperative that the negative phase be included for all structures whenever research is being conducted.

For blast design, the reflected pressure is assumed to be developed over the entire surface of the structure. Therefore, the total force on the real system, $F(t)$, is proportional to the reflected pressure, $P(t)$. Once the forcing function, $F(t)$, is defined, the only remaining parameters to define are the mass, the damping, and the stiffness. Mass plays an important role in any dynamic system due to its contribution to the inertia force, $m\ddot{y}$. For simplicity, the following explanations will be based on the equation of motion for a general SDOF system. However, it should be noted that, in reality, the $m$ shown in the following equations would actually be $K_{LM}m$.

If Equation 5-1 is divided by the mass of the system, the equation of motion can be restated as follows:

$$\ddot{y} + \frac{c}{m}\dot{y} + \frac{k}{m}y = \frac{F(t)}{m} \tag{5-9}$$

In Equation 5-9, $k/m$ is referred to as the square of the natural circular frequency, $\omega^2$. The general definition of the natural circular frequency is

$$\omega = \sqrt{\frac{k}{m}} \tag{5-10}$$

which has units of radians per second. The natural period of the structure, the time

required to complete one cycle during free vibration, is related to the natural circular

frequency by Equation 5-11:

$$T = \frac{2\pi}{\omega} \tag{5-11}$$

For systems in which the response is expected to remain entirely within the elastic

range of stresses for the respective material, the value of $k$ remains constant throughout

the entire response. The stiffness remains directly proportional to the modulus of

elasticity, $E$, of the respective material; the stiffness is also a function of the geometric

properties of the system. For example, consider the simply supported beam shown in

Figure 5.3, subjected to a uniformly distributed load, $w$.
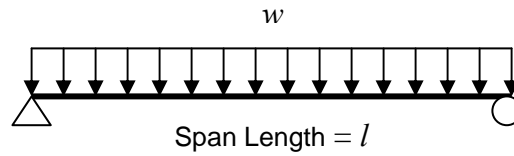


**Fig. 5.3.** Simple beam with uniform load $w$

From structural analysis, it can be shown that for small displacements, the deflection at

mid-span is equal to the following equation:

$$\Delta = \frac{5wl^4}{384\,E\,I} \tag{5-12}$$

where $I$ is the area moment of inertia about the axis of bending of the cross section. Now,

let the total load on the structure be $W = wl$. Then, defining stiffness as $k = W/\Delta$ and by

rearranging Equation 5-12, it can be shown that the stiffness of the beam with respect to

deflection at mid-span is

$$k = \frac{384\,E\,I}{5\,l^3} \qquad (5\text{-}13)$$

as long as the stress in the beam does not exceed the yield stress $f_y$.

If yielding of the material occurs, then the value of $k$ must be redefined based on

an updated value for $E$; however, when the material yields, the linear-elastic definition of

$k$ becomes invalid. Therefore, some simplifying assumptions are made in order to

evaluate the structure's resistance to deformation after yielding. For typical civil

engineering materials such as steel or reinforced concrete, a linear-elastic-perfectly-

plastic load-deflection assumption (shown in Figure 5.4) is usually sufficient. Obviously,

once yielding has occurred, a new method of defining the equation of motion is necessary

since $k$ is now equal to zero. Theoretically, after the material has yielded, the structure is

not capable of carrying any additional load; however, it is capable of continuing to carry

the ultimate load until an ultimate deflection is reached. Once the ultimate deflection is

reached, the structure will completely fail. Conservatism is built into this model since

most building materials exhibit strain-hardening during plastic behavior. If a term $R$ is

defined as the resistance of the structure to load, then it can be said that during elastic

behavior $R = k\,y$, and thus the equation of motion can be rewritten as follows:

$$\ddot{y} + \frac{c}{m}\dot{y} + \frac{R}{m} = \frac{F(t)}{m} \qquad (5\text{-}14)$$
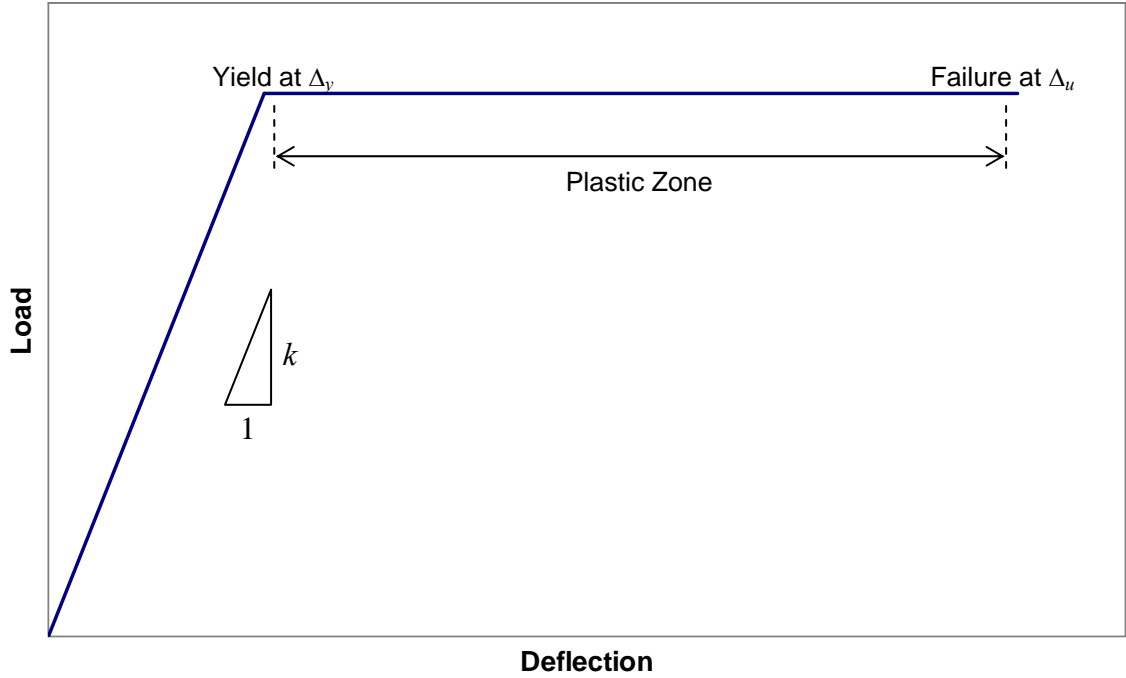
**Fig. 5.4.** Linear-elastic-perfectly-plastic material definition

The maximum load that the structure can sustain can be defined as $R_m = k \Delta_y$. To obtain an equation for $\Delta_y$ for the simply supported beam of Figure 5.3, a relation between the ultimate moment capacity, $M_u$, and the applied load, $w$, must be established. $M_u$ is ordinarily calculated based on the appropriate design code for the system considered (e.g. ACI-318 for reinforced concrete). For the simply supported beam under consideration, the maximum moment will always occur at mid-span and is equal to $\frac{wl^2}{8}$. Therefore, the load, $w_u$, associated with the ultimate capacity is equal to $\frac{8 M_u}{l^2}$. Substitution of this value for $w$ into Equation 5-12 results in the following relationship for the deflection at yielding:

144

$$\Delta_y = \frac{40 M_u l^2}{384 E I} \qquad (5\text{-}15)$$

Therefore, by substituting Equations 5-13 and 5-15 into the expression for the maximum

load the structure can sustain, the ultimate resistance can be expressed as

$$R_m = \frac{8 M_u}{l} \qquad (5\text{-}16)$$

These equations must be redefined for systems with different loading and/or boundary

conditions. The simply supported beam was chosen here partly as an illustration, but

primarily because the walls under consideration were modeled using these conditions.

Biggs (1964) derived these equations for use in SDOF analysis for many common

systems.

The point at which the structural system is unable to sustain its ultimate load any

longer is governed by a deflection limit that coincides with failure of the structure.

However, it is important to remember that the deflection-based definition of failure in this

situation is different from the typical structural design definition of failure. In elementary

structural design, all of the equations essentially assume linear-elastic behavior, and, thus,

failure is defined as the point at which the material yields. In many blast design

situations, it is more cost effective to design a structure so that it will protect the

occupants of the building, but the structure itself will be rendered unusable after the blast.

Therefore, blast design relies on the strain energy potential and inertial resistance of the

system to absorb the energy of the explosion.

The ultimate deflection that a structure can sustain can be very challenging to

calculate reliably. In most cases, ultimate deflection is defined as a simple relation

between span length and allowable support rotation. Allowable support rotation is often

governed by a certain "level of protection" or LOP; the higher the LOP is for a structure, the less the allowable rotation will be. Ultimate deflection also depends on the material being used because allowable support rotation values depend on the type of material under consideration. Usually, then the ultimate deflection, $\Delta_u$, is determined to be a conservative estimate of failure that determines the allowable amount of strain energy that can be taken advantage of for a given system.

As mentioned earlier, damping is typically ignored in predicting the response to impulse loads; however, for completeness, damping will now be discussed. Damping is typically present in a structural system in one or more of the following forms: hysteresis damping, Coulomb damping, or viscous damping. Viscous damping is most often used in structural dynamics because it is easily implemented in the equation of motion. Viscous damping, by definition, produces a damping force that is proportional to the velocity of the mass (the $c\dot{y}$ term in Equation 5-1). For a general SDOF system, the derivation of the damping constant, $c$, is related to a special damping constant known as the critical damping (Tedesco 1999). It can be shown that critical damping is

$$C_{cr} = 2m\omega \tag{5-17}$$

Since obtaining an equation for $c$ can become complicated, it is usually defined as a percentage of critical damping. The ratio of the damping in a system to the critical damping is known as the damping factor and is defined as

$$\zeta = \frac{c}{C_{cr}} \tag{5-18}$$

When $\zeta$ is equal to unity, the amount of damping is such that vibration is completely eliminated from the system during free vibration (Biggs 1964).

Since the equation of motion is a second order, non-homogeneous differential equation, it is possible to obtain a closed-form solution for displacement via a rigorous mathematical approach. The rigorous approach, however, becomes increasingly complicated for systems possessing nonlinear resistance and forcing functions. Therefore, although it is mathematically feasible, a closed-form solution will not be presented here because it is not practical for use with blast design.

The alternative to a closed-form solution is a step-by-step numerical integration of the differential equation of motion. The two fundamental concepts involved in numerical integration are "(1) the equation of motion is satisfied at only discrete time intervals $\Delta t$, and (2) for any time $t$, a variation of displacement, velocity, and acceleration within each time interval $\Delta t$ is assumed" (Tedesco 1999). A numerical integration scheme that works well for nonlinear dynamic problems is the central difference method. Although the current discussion of the central difference method is based on a SDOF system, it is also easily formulated to analyze massive multiple degree of freedom (MDOF) systems. In fact, it is the solution method most commonly used in finite element (FE) software for the solution of nonlinear dynamic problems. The following derivation of the central difference method was generated with reference to *Structural Dynamics: Theory and Applications* (Tedesco 1999).

Because the derivation of the central difference method is more easily comprehended for linear systems, the basic equations are derived for a linear SDOF system first before introducing the adaptations for considering nonlinear systems. This should provide a better understanding of both the central difference method and the effects that nonlinear behavior has on the complexity of the solution.

Consider the displacement versus time relationship shown in Figure 5.5. From calculus, it is known that the derivative of a point on a curve is equal to the tangential slope at that point. Therefore, the slope of the displacement curve (the velocity) shown
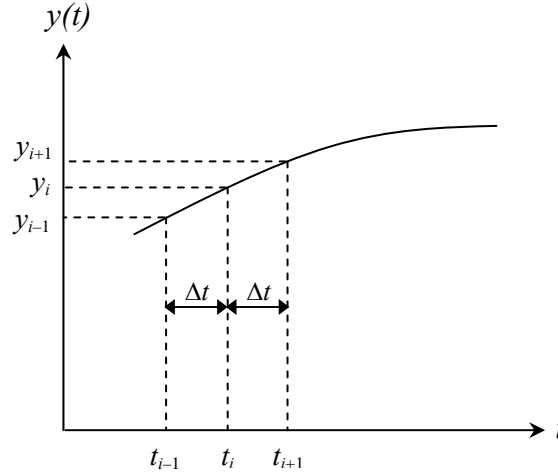


**Fig. 5.5.** Displacement versus time for central difference method

can be approximated by the following:

$$\dot{y}_i = \left(\frac{dy}{dt}\right)_{t_i} = \frac{\Delta y}{\Delta t} = \frac{y_{i+1} - y_{i-1}}{t_{i+1} - t_{i-1}} = \frac{y_{i+1} - y_{i-1}}{2\,\Delta t} \qquad (5\text{-}19)$$

In a similar fashion, the slope of the velocity curve (acceleration) can be defined as

$$\ddot{y}_i = \left(\frac{d^2 y}{dt^2}\right)_{t_i} = \frac{\left(\dfrac{dy}{dt}\right)_{t_i + (\Delta t/2)} - \left(\dfrac{dy}{dt}\right)_{t_i - (\Delta t/2)}}{\Delta t} \qquad (5\text{-}20)$$

which equates to the following:

$$\ddot{y}_i = \frac{\left(\dfrac{y_{i+1} - y_i}{\Delta t}\right) - \left(\dfrac{y_i - y_{i-1}}{\Delta t}\right)}{\Delta t} = \frac{y_{i+1} - 2 y_i + y_{i-1}}{(\Delta t)^2} \qquad (5\text{-}21)$$

148

For a viscously damped, linear SDOF system, the equation of motion at time $t_i$ is

$$m\ddot{y}_i + c\dot{y}_i + ky_i = F_i \tag{5-22}$$

By substituting Equations 5-19 and 5-21 into Equation 5-22 and rearranging, the

following expression for the displacement at time $t_{i+1}$ is obtained:

$$y_{i+1} = \left[\frac{1}{m/(\Delta t)^2 + c/(2\Delta t)}\right] \left\{\left[\frac{2m}{(\Delta t)^2} - k\right]y_i\right.$$

$$\left. + \left[\frac{c}{2\Delta t} - \frac{m}{(\Delta t)^2}\right]y_{i-1} + F_i\right\} \tag{5-23}$$

This equation will require a modification for use at the first time step after $t = 0$; this is

due to the fact that Equation 5-23 includes $y_i$ as well as $y_{i-1}$. From Equations 5-19 and

5-21, the following expression for $y_{i-1}$ at $t$ equal to zero can be obtained:

$$y_{i-1} = y_0 - \dot{y}_0 \Delta t + \frac{\ddot{y}_0(\Delta t)^2}{2} \tag{5-24}$$

Since the initial displacement and velocity are known, the only unknown left in Equation

5-24 is $\ddot{y}_0$. However, the initial acceleration can also be found by substituting the initial

conditions into Equation 5-22 as follows:

$$\ddot{y}_0 = \frac{1}{m}\left[F_0 - c\dot{y}_0 - ky_0\right] \tag{5-25}$$

Now the solution can be started by making use of Equation 5-25, and the displacement at

all other time steps can be found by using Equation 5-23.

These equations define the approach for solving linear SDOF systems. By

incorporating methodology similar to that used in the stiffness method in structural

analysis, these equations can be adapted for use with MDOF systems as well. MDOF systems are discussed further in Section 5.4.

Finally, the central difference method can be adapted to account for nonlinear material behavior. This is necessary to model resistance definitions that include effects such as plastic behavior. For nonlinear SDOF systems, the governing equation of motion is altered so that

$$m\ddot{y}_i + c\dot{y}_i = F_i - (F_S)_i \qquad (5\text{-}26)$$

where $(F_S)_i$ takes the place of $ky_i$ and is known as the restoring force in the system. The same approximations for velocity and acceleration are used, namely Equations 5-19 and 5-21. When these two equations are substituted into Equation 5-26, the following equation of motion results:

$$m\left[\frac{y_{i+1} - 2y_i + y_{i-1}}{(\Delta t)^2}\right] + c\left[\frac{y_{i+1} - y_{i-1}}{2\Delta t}\right] = F_i - (F_S)_i \qquad (5\text{-}27)$$

Therefore, by taking Equation 5-27 and solving for the only unknown, which is the deflection at the next time step, the equation defining $y_{i+1}$ is found to be the following:

$$y_{i+1} = \left[\frac{1}{m/(\Delta t)^2 + c/(2\Delta t)}\right]\left\{\frac{2m}{(\Delta t)^2}y_i + F_i\right.$$

$$(5\text{-}28)$$

$$\left. - (F_S)_i + \left[\frac{c}{2\Delta t} - \frac{m}{(\Delta t)^2}\right]y_{i-1}\right\}$$

For the purpose of programming these equations, Equation 5-28 is typically simplified by defining the following two values:

$$\hat{m} = \frac{m}{(\Delta t)^2} + \frac{c}{2\Delta t} \qquad (5\text{-}29a)$$

150

$$\hat{F}_i = \frac{2m}{(\Delta t)^2} y_i + F_i - (F_S)_i + \left[ \frac{c}{2\Delta t} - \frac{m}{(\Delta t)^2} \right] y_{i-1} \qquad \text{(5-29b)}$$

So that now

$$y_{i+1} = \frac{\hat{F}_i}{\hat{m}} \qquad \text{(5-30)}$$

The starting procedure would still be used in the same fashion as before. Finally, to give

a complete solution for a system with distributed mass, the equations must be multiplied

by the appropriate load factors. However, one more modification must first be included.

Since these equations are developed for the purpose of modeling nonlinear behavior, and

since the load-mass factor's governing shape function does not necessarily remain

constant throughout a nonlinear response, the load-mass factor must also vary with time.

Therefore, Equations 5-29a and 5-29b become

$$(\hat{m}_e)_i = \frac{(K_{LM})_i m}{(\Delta t)^2} + \frac{c}{2\Delta t} \qquad \text{(5-31a)}$$

$$(\hat{F}_e)_i = \frac{2(K_{LM})_i m}{(\Delta t)^2} y_i + F_i - (F_S)_i + \left[ \frac{c}{2\Delta t} - \frac{(K_{LM})_i m}{(\Delta t)^2} \right] y_{i-1} \qquad \text{(5-31b)}$$

and Equation 5-30 becomes

$$y_{i+1} = \frac{(\hat{F}_e)_i}{(\hat{m}_e)_i} \qquad \text{(5-32)}$$

In order to obtain accurate results via the central difference method, the size of the

time step, $\Delta t$, must be chosen carefully. The central difference method is conditionally

stable for $\Delta t \leq \Delta t_{cr}$, where $\Delta t_{cr}$ is the critical time step size and is defined as

$$\Delta t_{cr} = \frac{T}{\pi} \qquad \text{(5-33)}$$

where $T$ is the natural period of the system. For MDOF systems, $T$ is defined as the smallest natural period of the system, which corresponds to the highest natural frequency. Solution methods that are conditionally stable are known as explicit methods and can become unstable due to time steps that are too large. In contrast to explicit methods are implicit methods, which are unconditionally stable, meaning that the equations can be accurately evaluated using a much larger time step than can be used with explicit methods. Since the calculations used in implicit methods do not rely on data from the previous time step, the methods are also self starting. Implicit methods allow the use of virtually any time step size; however, if the time step chosen is too large, then important behavior may not be captured in the response. Therefore, practical limits for time step size exist for each methodology. In general, explicit methods are preferred because they help eliminate convergence issues when facing highly nonlinear dynamic problems.

## 5.4 MDOF Methodology

It is not always possible to reduce a complex system down to a single degree of freedom. In such cases, a multi-degree-of-freedom (MDOF) approach must be used. MDOF systems possess multiple equations of motion and multiple natural frequencies. Matrix notation is used to describe the relations for MDOF systems. This provides an organized, systematic approach to solving problems that can easily be programmed on a digital computer.

The equations defining MDOF systems are almost identical to those for SDOF systems. The primary difference between the two systems is that each scalar term is now

either a column vector or a square matrix.  For a general, elastic MDOF system, the

equation of motion is expressed as

$$[m]\{\ddot{y}\} + [c]\{\dot{y}\} + [k]\{y\} = \{F(t)\} \tag{5-34}$$

where $[m]$ is the mass matrix, $[c]$ is the damping matrix, $[k]$ is the stiffness matrix,

$\{F(t)\}$ is the force vector, and $\{\ddot{y}\}$, $\{\dot{y}\}$, and $\{y\}$ are the acceleration, velocity, and

displacement vectors for each degree of freedom, respectively.  Therefore, the equation

of motion for a MDOF system is

$$\{K_{LM}\}[m]\{\ddot{y}\} + [c]\{\dot{y}\} + [k]\{y\} = \{F(t)\} \tag{5-35}$$

where $\{K_{LM}\}$ is a vector of load-mass factors pertaining to each respective degree of

freedom.  This system of equations can be solved in the same manner as its

corresponding SDOF version via the central difference method.  For an equivalent

system, the effective mass and effective force vectors used in the numerical integration

are expressed as

$$[\hat{m}_e]_i \;=\; \frac{1}{(\Delta t)^2}\{K_{LM}\}_i\,[m] + \frac{1}{2\,\Delta t}[c] \tag{5-36a}$$

and

$$\{\hat{F}_e\}_i \;=\; \{F\}_i - \{F_S\}_i + \frac{2}{(\Delta t)^2}\{K_{LM}\}_i\,[m]\{y_i\}$$

$$\tag{5-36b}$$

$$+ \left[\frac{1}{2\,\Delta t}[c] - \frac{1}{(\Delta t)^2}\{K_{LM}\}_i\,[m]\right]\{y\}_{i-1}$$

where $\{F_S\}_i$ is the restoring force vector at a given time step.  The deflection at the next

time step is then calculated by the following equation:

$$\{y\}_{i+1} \ = \ \frac{\{\hat{F}_e\}_i}{\{\hat{m}_e\}_i} \tag{5-37}$$

## 5.5 SBEDS Analysis

As previously stated, the Single-Degree-of-Freedom Blast Effects Design Spreadsheets (SBEDS) program can be used for a wide variety of blast design applications. Due to its availability and user-friendly interface, it was well suited for performing prediction analyses for the walls under investigation. SBEDS was also chosen because it was a prime candidate for implementation of the resistance definitions developed over the course of this project. The details of the system modeled by SBEDS are shown in Figure 5.6, where $m$ is the total mass of the system, $R$ is the resistance of the masonry wall, $y$ is the midpoint deflection of the masonry wall, and $F(t)$ is the applied blast load. The SBEDS methodology manual (PDC-TR 06-01) and user's guide (PDC-TR 06-02) provide the technical background for the software (USACE PDC 2006). Damping is not shown because it was ignored in this analysis; however, SBEDS can include damping, expressed as a percentage of critical damping.
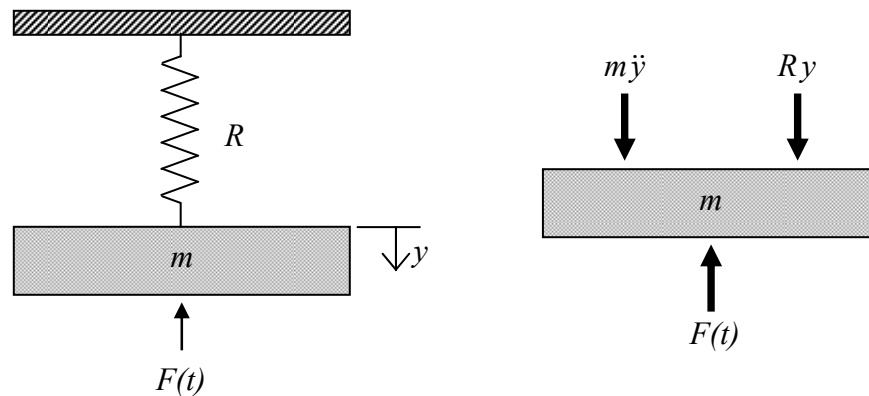


**Fig. 5.6.** SBEDS SDOF model

154

SBEDS has pre-programmed options for designing both unreinforced and reinforced concrete masonry unit (CMU) walls. This capability provided a simple way to attain the basic resistance function for a reinforced masonry wall. The wall was modeled as a strip based on reinforcement spacing equal to 48 inches on center. The support conditions were set as simple supports, and a flexural-only response was chosen. The wall's physical properties were entered as follows: span length = 10.5 feet, wall thickness = 7.625 inches, reinforcing steel spacing = 48 inches, reinforcing steel area = 0.31 square inches, depth of reinforcing steel = 3.8125 inches, masonry type = Medium Weight CMU, percent of void space grouted = 100, masonry compressive strength = 2500 psi, and steel yield strength = 60 ksi. To account for the exterior brick veneer, an additional mass of 40 lb/ft$^2$ was included in the model's definition. The time step was set to 0.10 msec, which adequately captured the behavior of the system, and damping was ignored.

For the prediction analysis, the SBEDS load prediction option was used. This method predicts reflected pressure history based on a charge weight and standoff distance. After the completion of the full-scale tests, the model was analyzed again but this time using the pressure histories acquired from testing. Due to failure of the mid-height gauge in the center in Detonations 2 and 3, the larger of the side pressures was used for these two cases. The pressure histories with their respective impulses are shown in Figures 5.7 through 5.9. The corresponding deflection histories can be found in Figures 5.10 through 5.12. The deflection plots from the full-scale testing are also included for comparison.
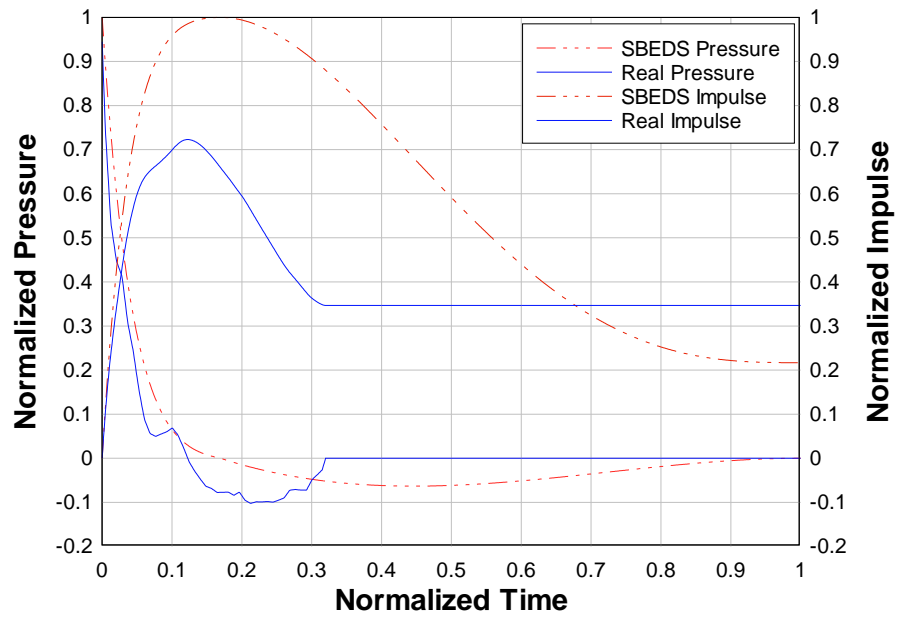
**Fig. 5.7.** Pressures and impulses for Detonation 1
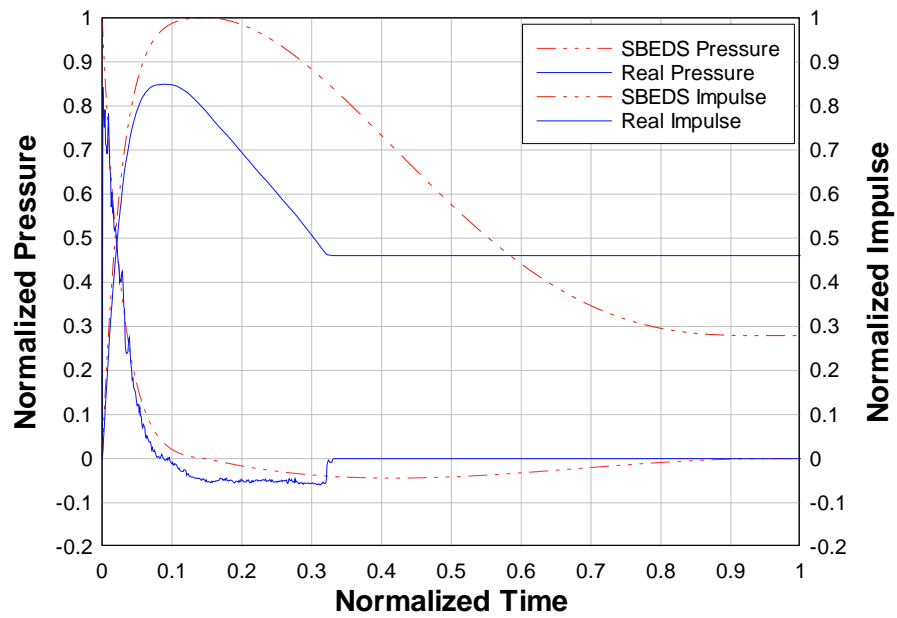


**Fig. 5.8.** Pressures and impulses for Detonation 2

156
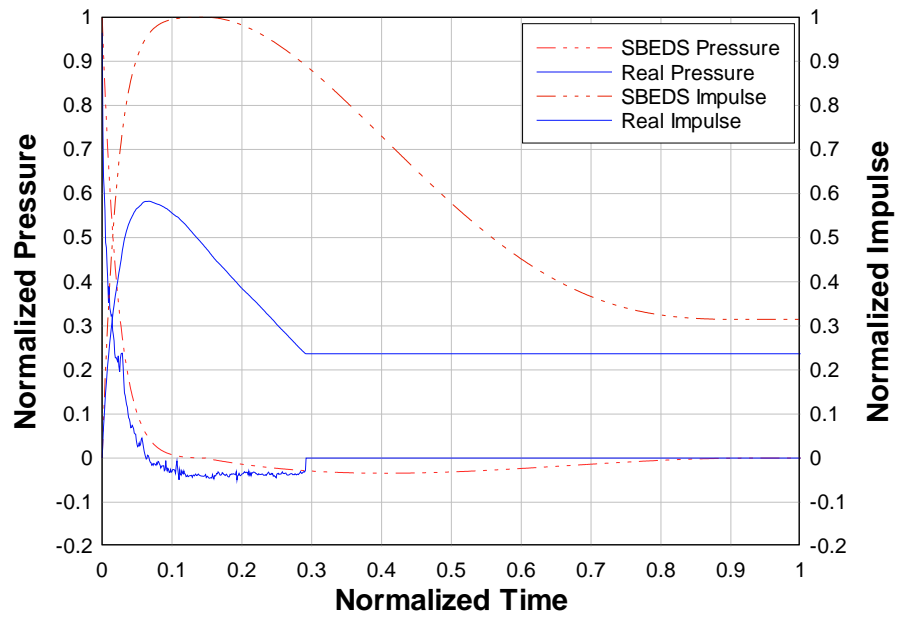
**Fig. 5.9.** Pressures and impulses for Detonation 3
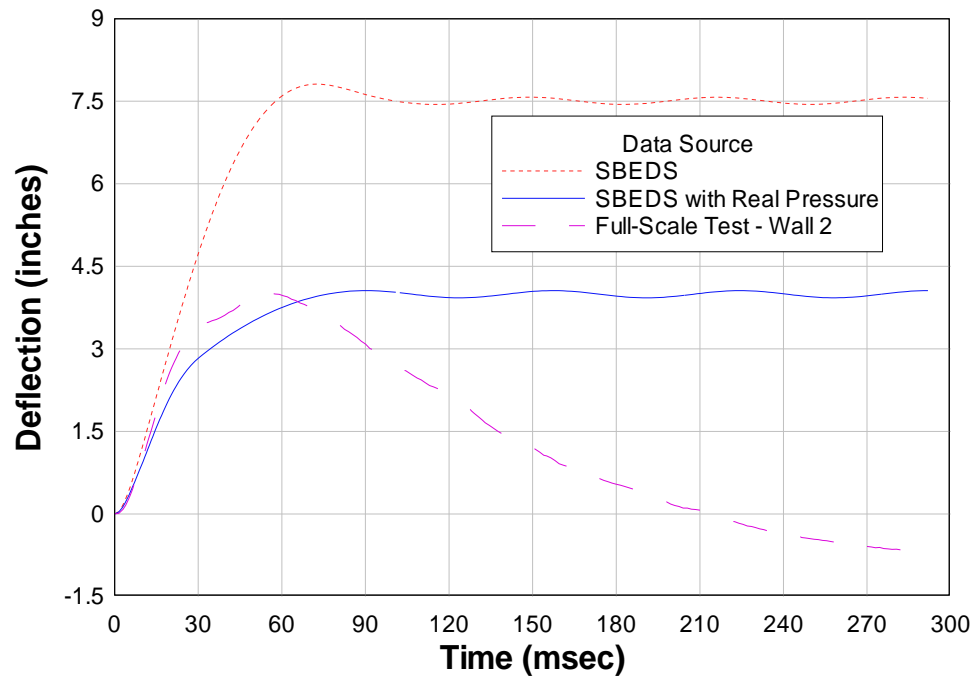


**Fig. 5.10.** SBEDS deflection predictions for Detonation 1

157
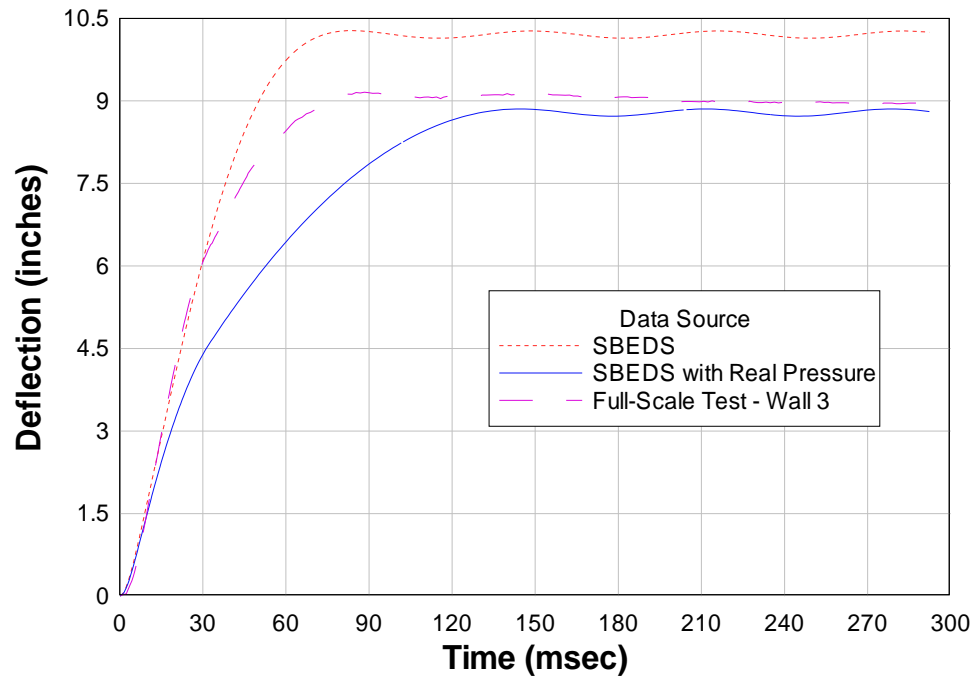
**Fig. 5.11.** SBEDS deflection predictions for Detonation 2
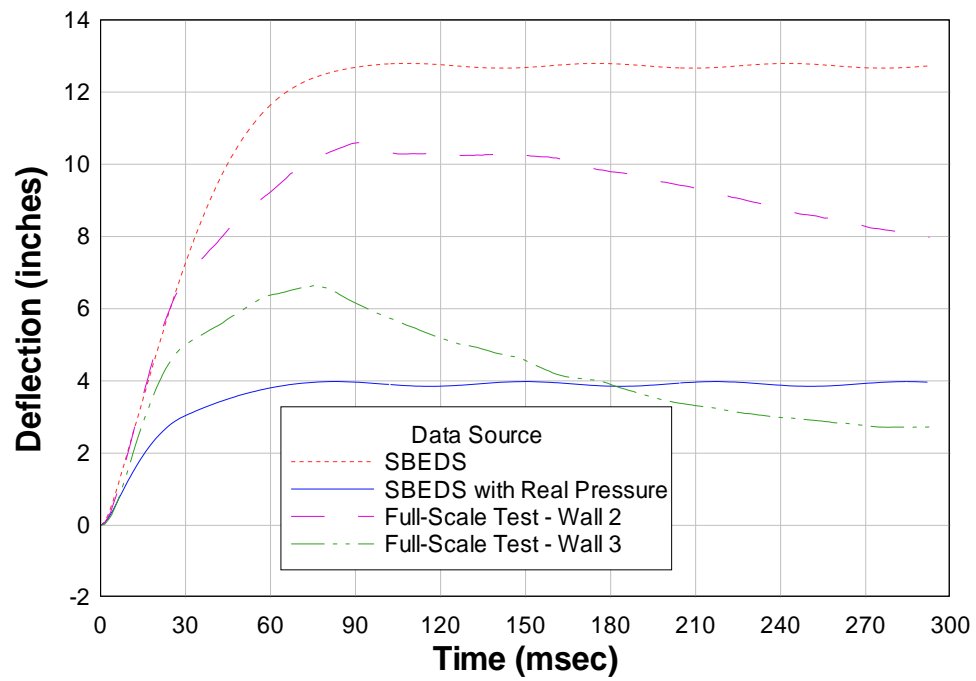


**Fig. 5.12.** SBEDS deflection predictions for Detonation 3

158

To obtain accurate predictions of deflection, it is not only vital to have a reasonable resistance definition, but it is also important to have an accurate estimate of the load that is to be applied. Figures 5.7, 5.8, and 5.9 demonstrate that the current load prediction method is not accurate but will result in a conservative design. Figure 5.10 shows the predicted deflection for Detonation 1 based on SBEDS load prediction along with its prediction based on the recorded pressure. The actual deflection is also shown in the figure. For Detonation 1, SBEDS predicted a deflection that was approximately twice as large as the recorded value. However, when the recorded pressure was used as the forcing function, SBEDS' prediction of peak deflection was within 1% of the recorded value. A similar result is shown in Figure 5.11, but no conclusions were drawn from this data because the system exhibited a support failure. Figure 5.12 shows a reasonable prediction from SBEDS, but does not show a good prediction when using the recorded pressure data. It is believed that this discrepancy was caused by the very close standoff distance, which resulted in a poorly developed pressure distribution. This, coupled with the fact that the pressure history could only be collected on the sides, resulted in a pressure history that did not accurately describe the total load that was imparted to the walls.

Based on these results, the resistance definition employed by SBEDS is sufficient for designing fully grouted reinforced masonry walls with non-structural brick veneers. When this resistance definition is combined with the SBEDS load prediction model, a competent engineer would be able to safely design a structure for a specified level of protection.

159

### 5.6 2-DOF Analysis of Foam

This section presents the development of a 2-DOF EL model. Obviously, to include the foam insulation in an EL model, a second degree of freedom had to be added. This model assumes that there is no flexural resistance associated with the brick veneer, and therefore, the mass of the veneer is simply added to that of the foam. The 2-DOF system is shown in Figure 5.13, where $m_1$ is the mass of the masonry wall, $m_2$ is the combined mass of the insulation and veneer, $R_1$ is the resistance of the masonry wall, $R_2$ is the resistance provided by the foam, $y_1$ is the deflection of the masonry wall, $y_2$ is the total deflection of the insulation and veneer, and $F_2(t)$ is the applied load due to blast. The value given by $\left(y_2 - y_1\right)$ represents the local deformation of the foam, or the amount that the foam has crushed. Although the foam insulation is somewhat elastic, it was
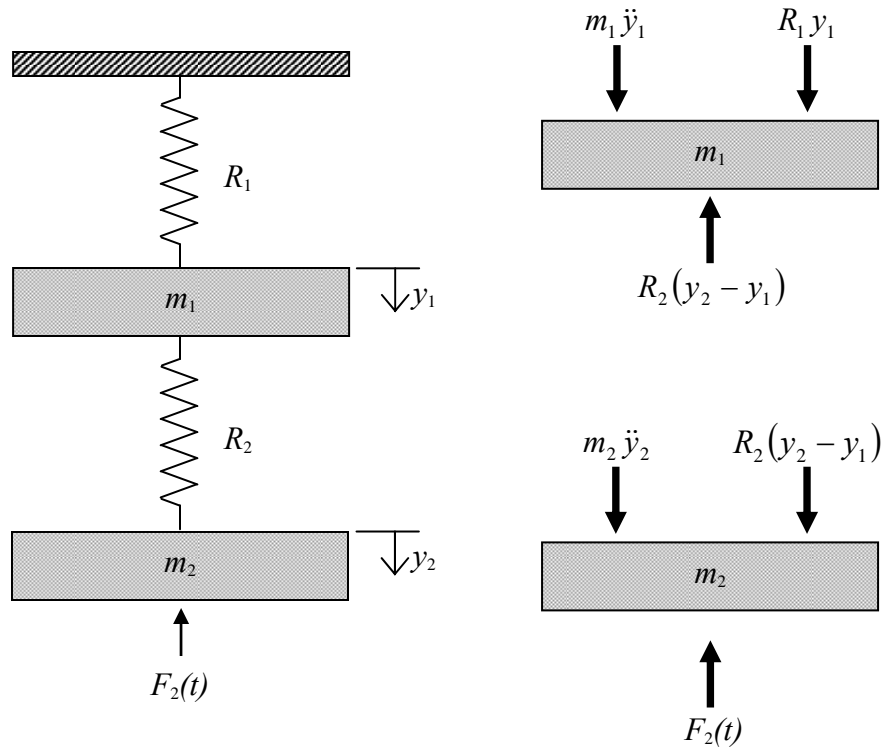


**Fig. 5.13.** Schematic of 2-DOF model

assumed to possess no elasticity for this model.  This assumption dictated that the 2-DOF

system would simplify to a SDOF system when the relative deflection of the foam began

to decrease with respect to the previous time step.  The simplified SDOF system is the

same as the one used in the SBEDS program, which appeared in Figure 5.6.

This model served as a tool in the comparison of foams with different constitutive

properties as well as different thicknesses.  This model was developed based on the

concept that the foam would be allowed to play an active role in the overall resistance of

the system.  To develop a resistance definition for the foam, the following assumptions

were made:  1) the foam reaches a maximum crushed deflection and remains constant, 2)

constitutive properties gathered from 2-inch-thick samples are applicable to specimens of

any thickness, 3) the area of foam loaded in the model is equal to the tributary area of the

wall, 4) the load-mass factor for the foam and veneer is equal to the elastic load-mass

factor for the masonry wall until the 2-DOF system is simplified to the SDOF system,

and 5) no strain rate effects were considered.  The algorithm was coded using Microsoft

Visual Basic in conjunction with Microsoft Excel.  The solver is capable of processing a

completely nonlinear resistance definition for both the foam and the CMU wythe.

A linear-elastic-perfectly-plastic resistance definition was used for the CMU

wythe; this is the same definition used in SBEDS.  The model was analyzed using the

same foam material properties described in Chapter 4.  A plot of these stress-strain

definitions is shown in Figure 5.14.  To use these curves in a 2-DOF model, stress and

strain was converted to load and deflection.  Since the entire area of the foam was

considered to be uniformly loaded, and since the load used in the model was expressed as

uniform pressure, the values for stress were identical to the values of load.  The

161
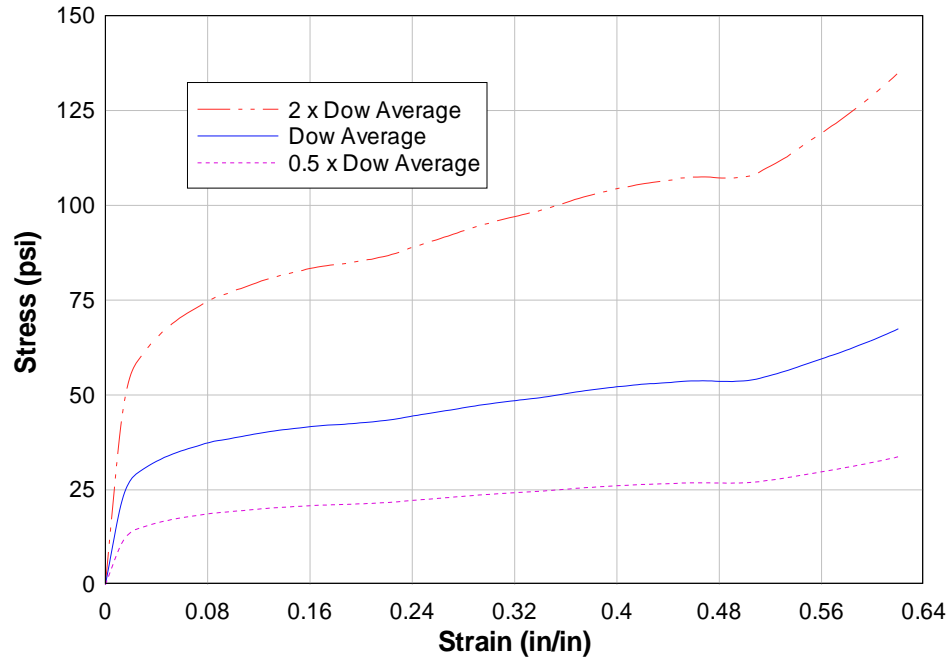
**Fig. 5.14.** Stress-strain curves for XEPS foams

deflection values were defined using the simple relation for engineering strain: strain

equals deflection divided by original length. Therefore, the strain values were multiplied

by the original thickness of the foam to obtain the respective deflections.

The 2-DOF foam model was compared with the SBEDS model as well as the FE

models described in Chapter 4. Therefore, the 2-DOF foam model was analyzed under

three load cases: the recorded pressures for Detonations 1 and 2, as well as the SBEDS-

generated load used for the FE analysis. The recorded pressure for Detonation 3 was not

used here since it did not produce reasonable results when used in SBEDS. The effect of

the thickness of the foam was also studied; therefore, the thicknesses were varied

between 2 inches, 4 inches, and 8 inches – just as they were for the FE models in Chapter

4. By varying the material properties of the foam, the load, and the thickness of the

foam, twenty-seven unique analysis cases were identified.

162

The results of the 2-DOF cases are summarized in Figures 5.15 through 5.24. In Figures 5.15 through 5.17, the mid-span deflection predictions using the recorded pressure from Detonation 1 are shown and compared to those made by SBEDS along with the actual deflection. In Figures 5.18 through 5.20, the same are shown for Detonation 2. Figure 5.21 shows a comparison of the mid-span deflection predicted by the benchmark FE model, FE-BM, to that predicted by SBEDS; both were loaded with the SBEDS-generated load corresponding to Detonation 3. Figures 5.22 through 5.24 show comparisons of the mid-span deflection predictions made by the FE models to those made by the 2-DOF models for each set of foam material properties.
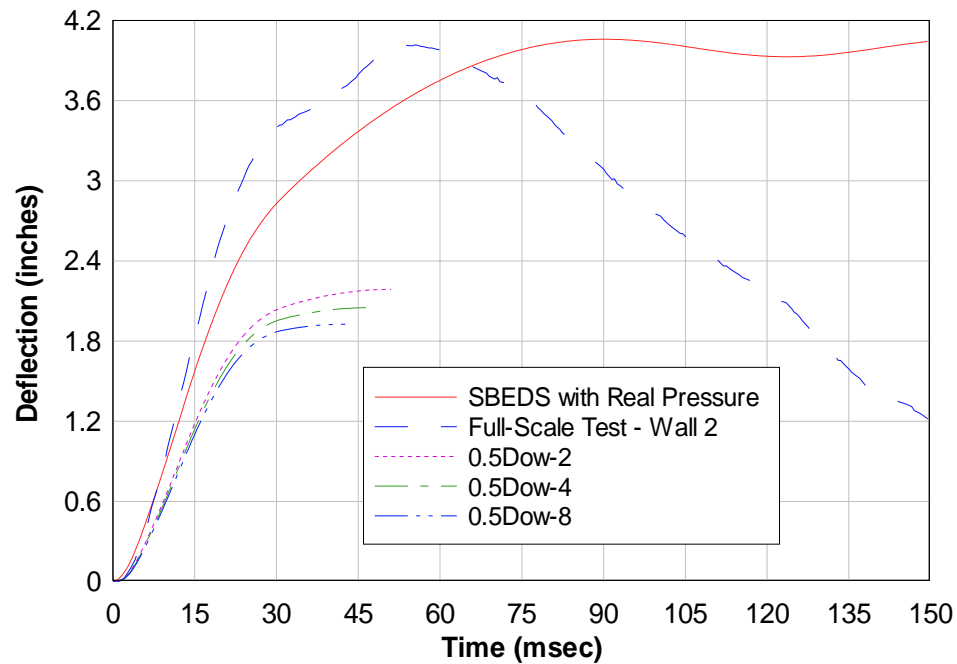


**Fig. 5.15.** Mid-span deflection predictions using pressure from Detonation 1 in 2-DOF model with 0.5Dow foam properties
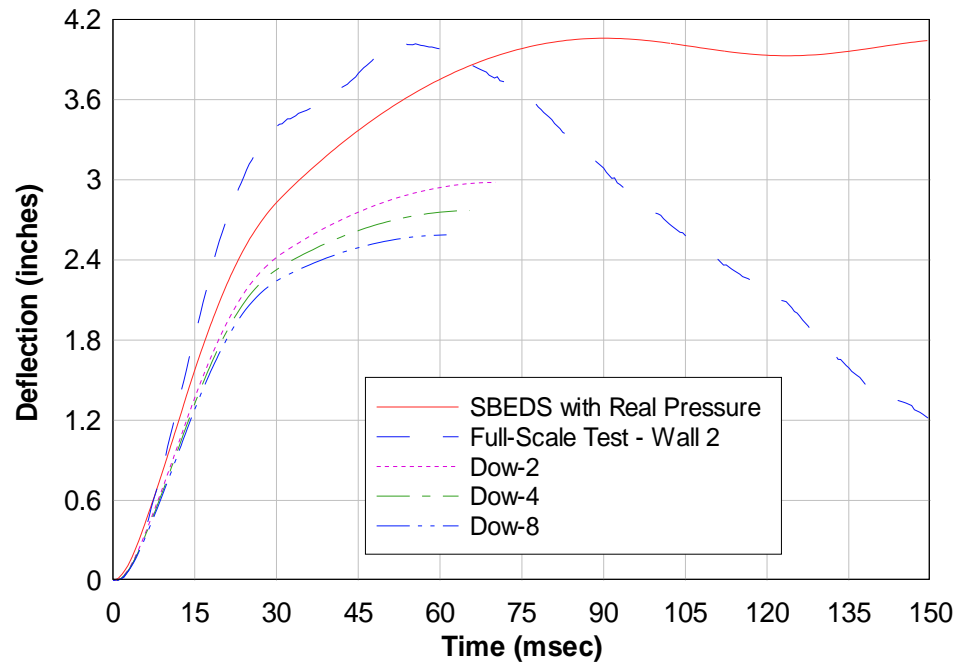
**Fig. 5.16.** Mid-span deflection predictions using pressure from Detonation 1 in 2-DOF model with Dow foam properties
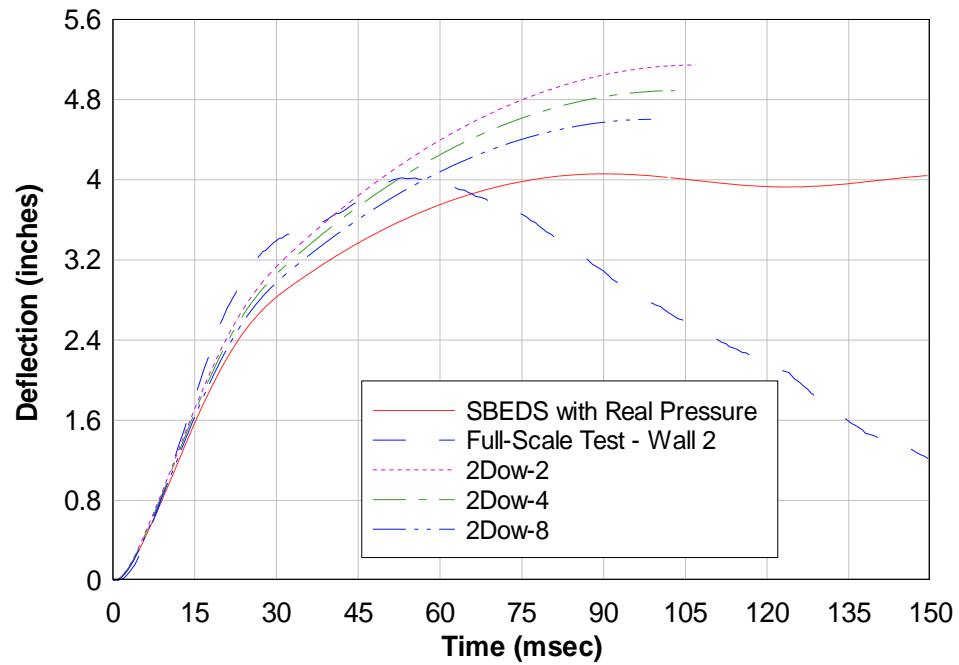


**Fig. 5.17.** Mid-span deflection predictions using pressure from Detonation 1 in 2-DOF model with 2Dow foam properties

164
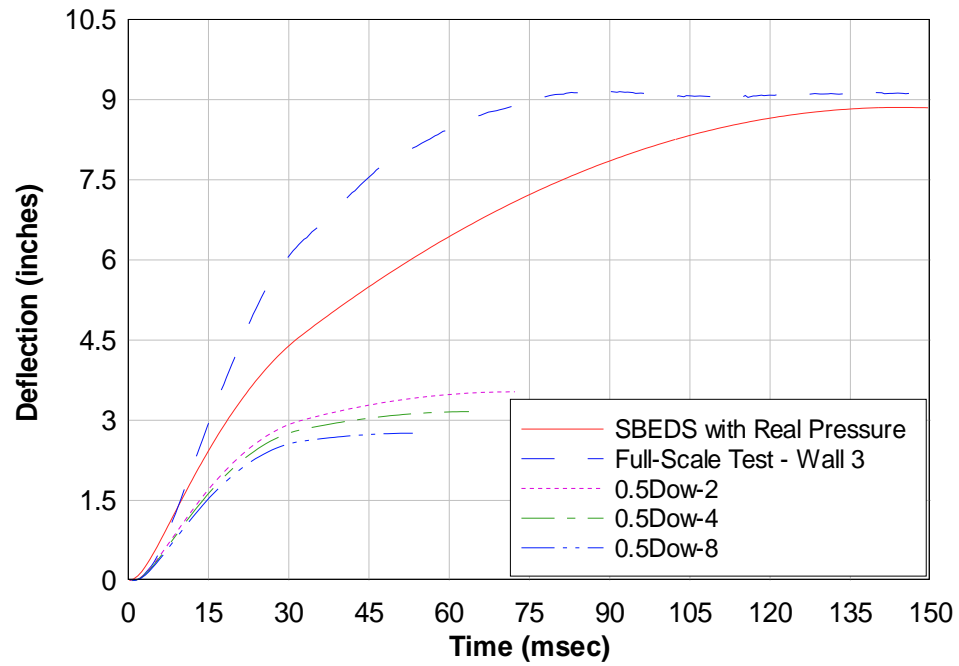
**Fig. 5.18.** Mid-span deflection predictions using pressure from Detonation 2 in 2-DOF model with 0.5Dow foam properties
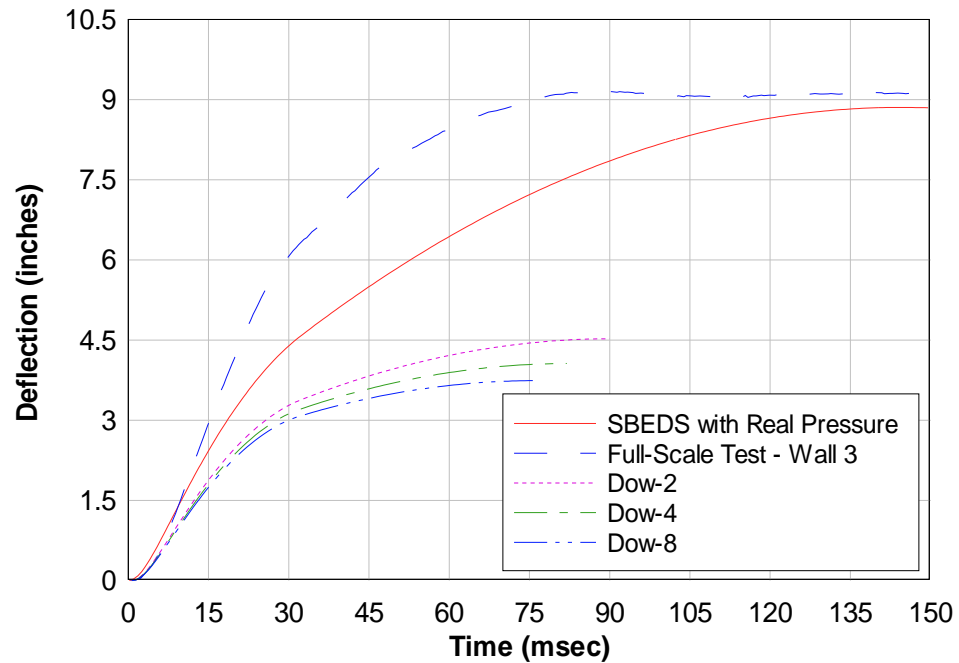


**Fig. 5.19.** Mid-span deflection predictions using pressure from Detonation 2 in 2-DOF model with Dow foam properties

165
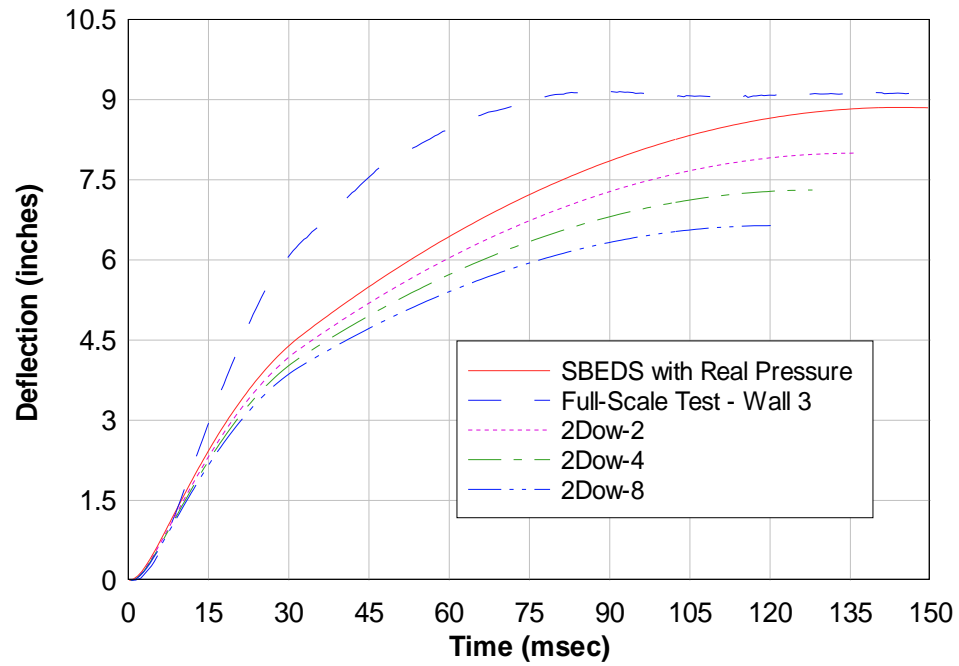
**Fig. 5.20.** Mid-span deflection predictions using pressure from Detonation 2 in 2-DOF model with 2Dow foam properties
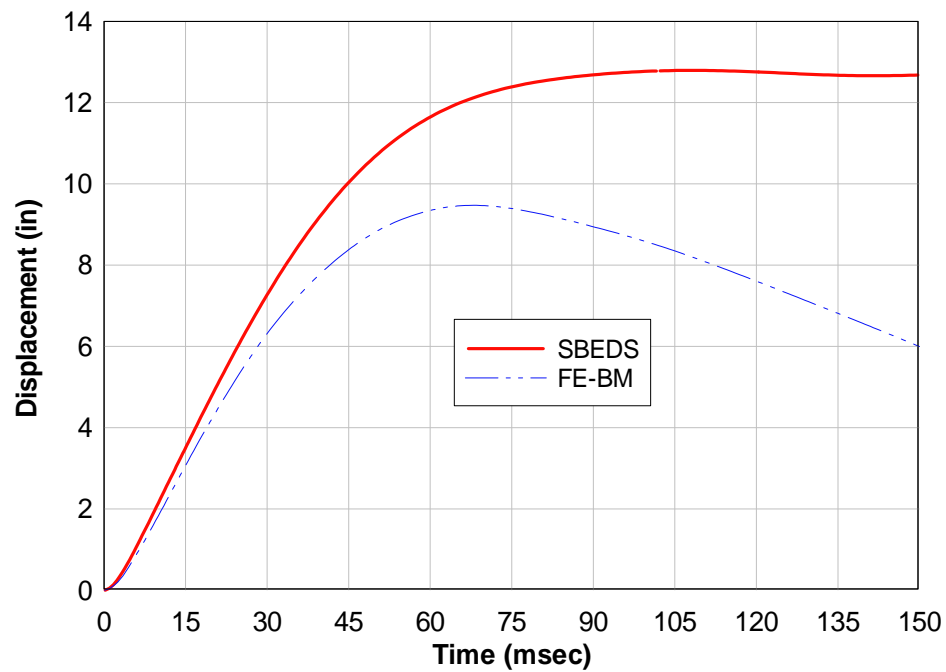


**Fig. 5.21.** Mid-span deflection predictions made by SBEDS and the FE-BM FE model using the SBEDS generated load

166
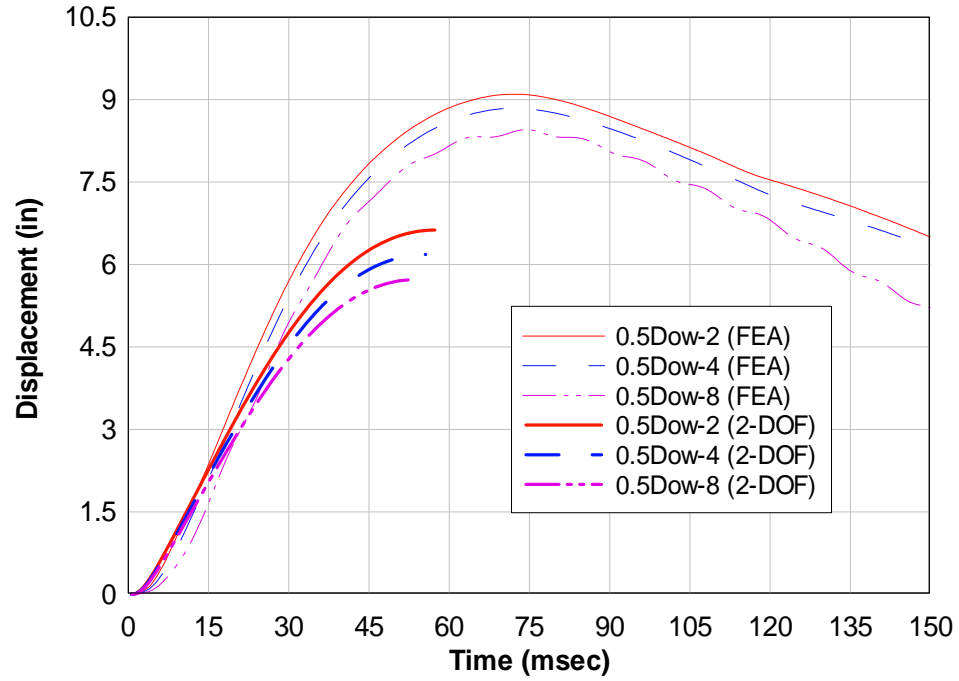
**Fig. 5.22.** Mid-span deflection predictions made by FE models and by 2-DOF models using 0.5Dow foam properties and the SBEDS generated load
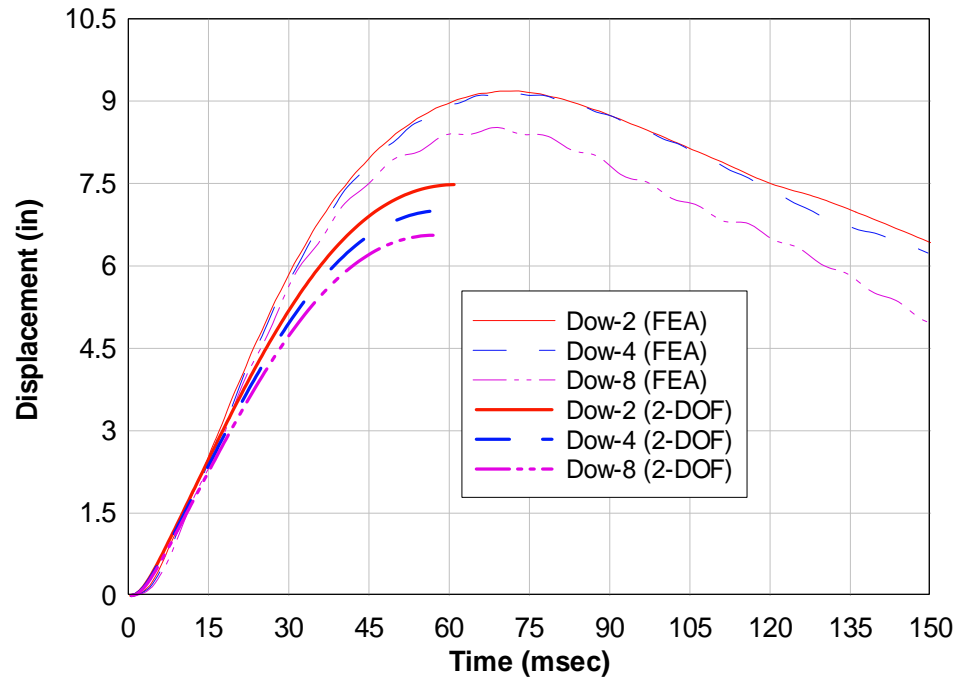


**Fig. 5.23.** Mid-span deflection predictions made by FE models and by 2-DOF models using Dow foam properties and the SBEDS generated load

167
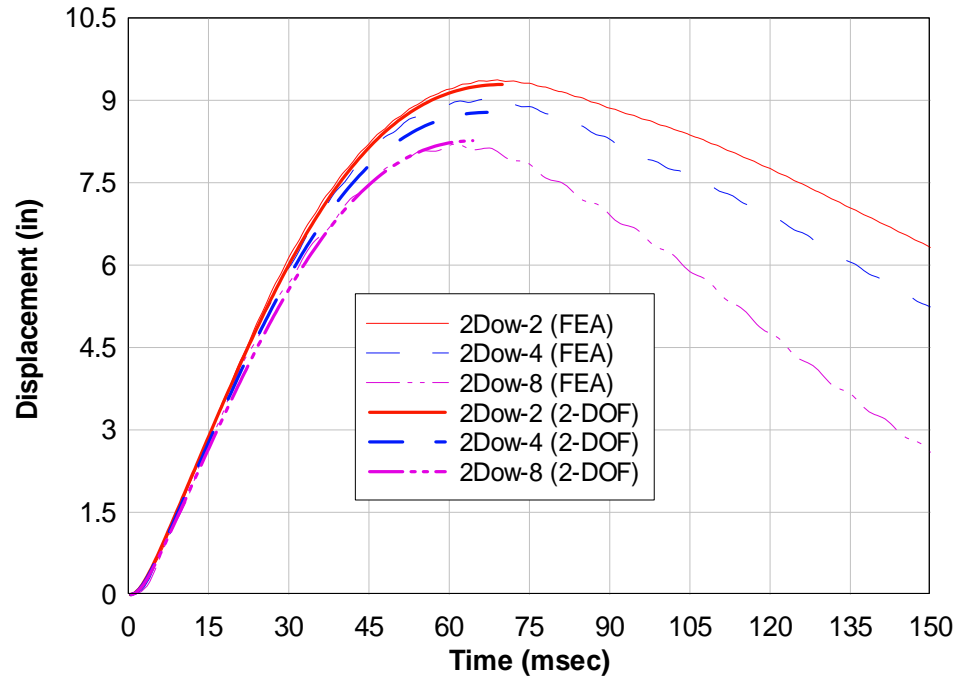
**Fig. 5.24.** Mid-span deflection predictions made by FE models and by 2-DOF models using 2Dow foam properties and the SBEDS generated load

The data presented in Figures 5.15, 5.16, and 5.18 through 5.20 indicate that the foam provides extra resistance. However, Figure 5.17 shows that the mid-span deflection increased due to the addition of the foam. Although it is not likely that this would occur in reality, it indicates a disadvantage of stiffer or stronger foam. Because the deflection increased for the load case corresponding to Detonation 1, but not for Detonation 2, this indicates that the response of the foam is sensitive to the intensity of the forcing function. Thus, the ability of the foam to reduce deflection is also a function of the applied load. In Detonation 1, the applied load is significantly less than the ultimate strength of the 2Dow foam, whereas, in Detonation 2, the ultimate strength is approximately equal to the peak load. This is discussed again later in the report.

Figure 5.21 shows that SBEDS predicts significantly more deflection than the FE-BM model. From a design safety standpoint, this is appropriate. By comparing Figures 5.22 and 5.23 with Figure 5.21, it can be seen that the reduction in deflection due to the inclusion of foam is much greater for the 2-DOF model than for the FE models. Note that although it appears that Figure 5.24 shows an almost perfect match of predicted deflection, this plot by itself is misleading. Figure 5.24 must be interpreted in parallel with Figure 5.21; then, it is clear that the 2-DOF model predicts a much larger reduction in deflection than the FE model. While there is a large difference in the predictions made by the 2-DOF models and those made by the FE models, the overall trend is the same. This trend shows that the inclusion of foam causes a decrease in mid-span deflection and that the mid-span deflection decreases as the thickness of the foam increases.

Because there is no laboratory test data to compare to either the FE or the 2-DOF foam models, it is impossible to be certain that either approach is accurate. It is reasonable to assume that the FE models provide a more realistic prediction due to the robust nature of FE modeling. Based on this assumption, the 2-DOF models overestimate the resistance provided by the foam. This, along with the case where the 2-DOF model predicted an increase in deflection, indicate that there is room for further research to be accomplished in developing an EL model for foam insulated wall sections. However, before attempting to develop an EL model that matches the FE models, laboratory testing should be conducted that would allow assessment of the validity of the FE models.

### 5.7 2-DOF Analysis of Ties

Because the foam did not appear to have received significant loading during the full-scale tests, it was assumed that the metal ties between the CMU wythe and the brick veneer transferred the load. In order to numerically validate this assumption, an EL model was developed in which the ties were included in the resistance definition. Figure 5.25 depicts the ideal arrangement for this system: $R_1$, $R_2$, and $R_3$ are the resistances of the CMU wythe, the brick veneer, and the ties, respectively, and $m_1$ and $m_2$ are the masses of the CMU wythe and the brick veneer, respectively. Note that, unlike the previous EL model, this system includes a resistance function for the brick veneer.
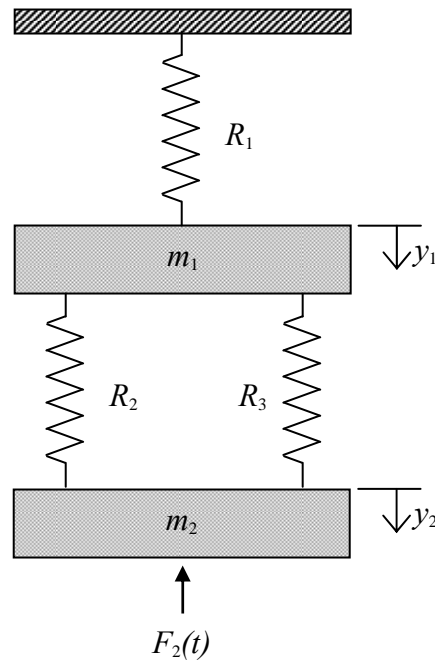
**Fig. 5.25.** Ideal arrangement for including resistance of metal ties

Due to the increased complexity of this system, coupled with the fact that this calculation was only used to validate the behavior witnessed during testing, a simplified approach was taken that allowed the previous EL model to be reused. Since establishing a definition of the resistance function for the brick veneer was outside the scope of work, an assumption was made to eliminate it from the system of equations. The load-mass factor for the brick would theoretically be defined in the same way as the one for the CMU wythe, which would lead to an elastic load-mass factor of 0.78. Instead, the load-mass factor for the brick was taken as unity, and the resistance of the veneer was omitted. This allowed the system to be solved using the same code developed for the previous 2-DOF model.

The material model most often used for steel is the elastic-perfectly-plastic model with unloading following the initial stiffness. Due to the elastic behavior of steel, the 2-DOF model written for the foam could not accurately simulate the entire response because the model assumed the foam would lock up, and therefore could not incorporate the unloading of the ties. To deal with this problem, the calculation was terminated when the ties began to rebound. The local peak deflection of the ties was then plotted to determine if the brick would have come into contact with the foam or not. For the wall sections used in testing, the ties could deflect one inch before the brick would come into contact with the foam. This would be an extreme strain in the ties (approximately 33%), but is not unreasonable since the ties were in compression, and the loading itself was an extreme event.

A set of technical notes supplied by The Brick Industry Association states that the static yield strength of the ties, based on ASTM A 82, is 70 ksi (1992). This magnitude

was amplified using the amplification factors for steel used by SBEDS. Two different resistance definitions were developed for approximating the resistance of the ties. The first assumed an elastic-perfectly-plastic material definition without any rupture conditions. The second approximation assumed that strain hardening would increase the ultimate strength of the material, but that it would eventually reach a peak and then start to decline. The resistance would eventually go to zero at a strain of 33%. These two resistance definitions are shown in Figure 5.26.
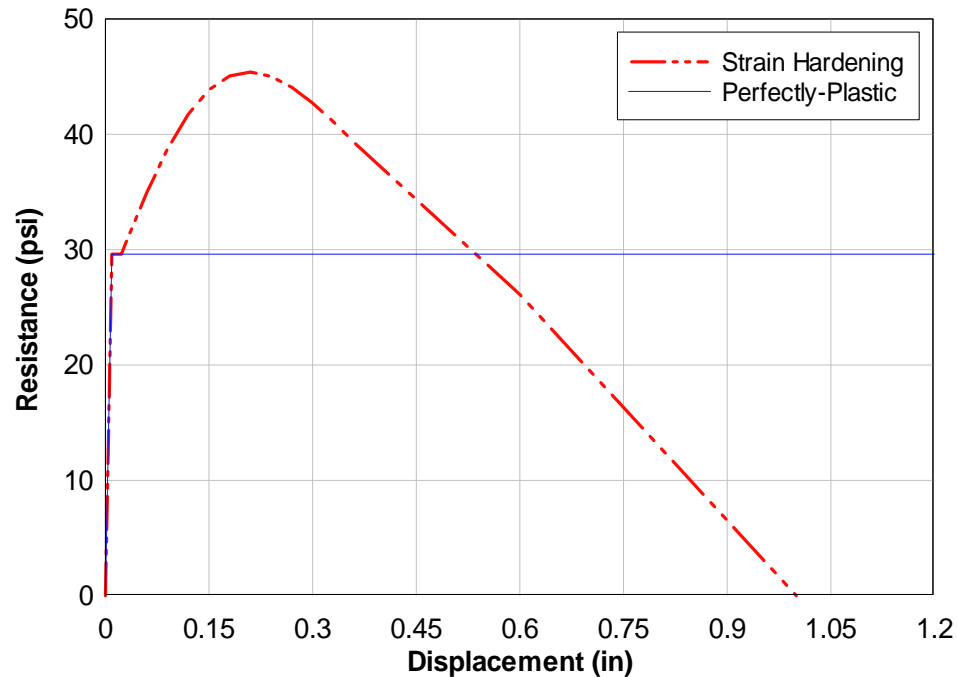


**Fig. 5.26.** Resistance functions for metal ties used in 2-DOF ties models

Using the perfectly-plastic resistance function, the model showed that the ties could transmit the recorded pressures associated with Detonations 1 and 2 without allowing the brick to encounter the foam. Since accurate recorded pressure data was not

available for Detonation 3, a pressure curve generated by SBEDS was used. The

parameters used to generate the curve in SBEDS were modified per engineering

judgment to compensate for the conservative nature of SBEDS. The resulting deflection

of the ties was slightly larger than the allowable deflection of one inch. The results of the

perfectly-plastic and the strain hardening models are shown in Figures 5.27 and 5.28,

respectively.
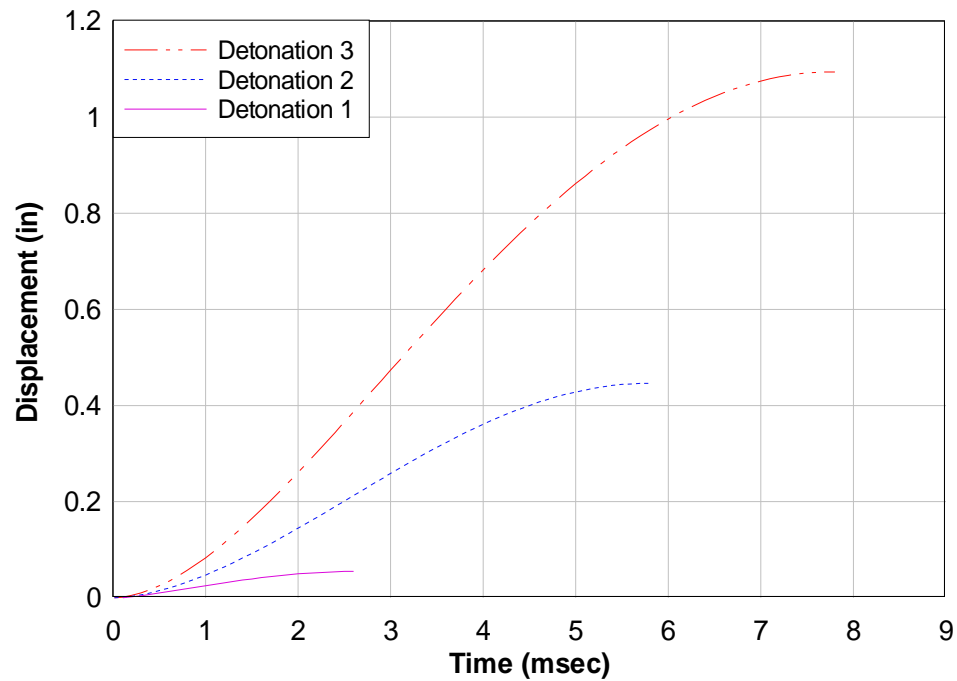


**Fig. 5.27.** Deflection of ties for perfectly-plastic 2-DOF ties models
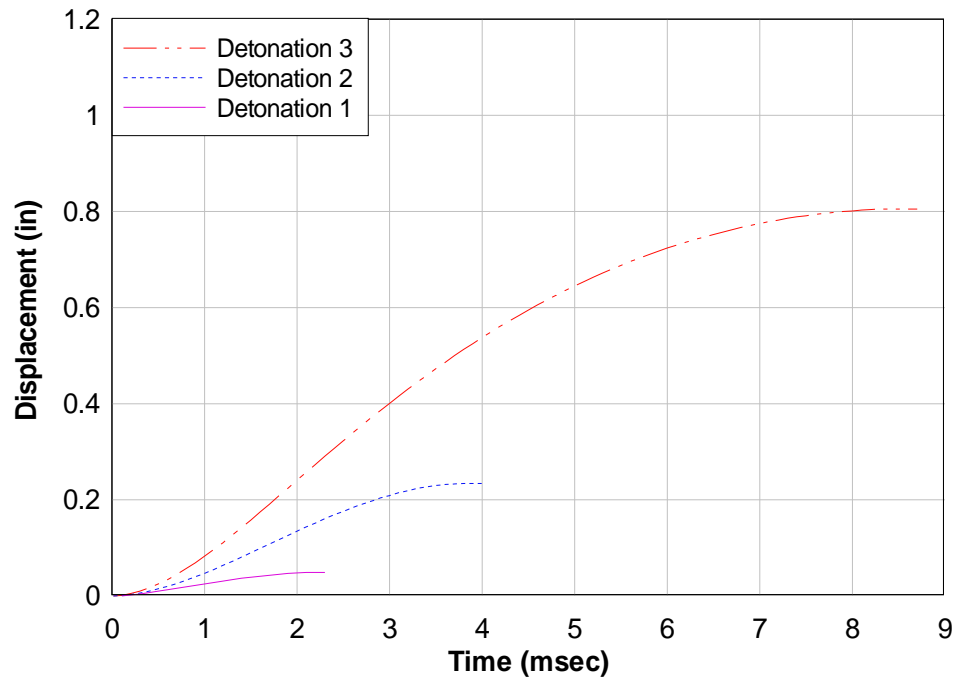
**Fig. 5.28.** Deflection of ties for strain hardening 2-DOF ties models

From Figure 5.28 it can be seen that if strain hardening effects are included, then even under the severe loading of Detonation 3, the ties would still have been able to transmit the load directly to the CMU wythe.

For completeness, buckling was considered in the determination of the resistance function of the ties. Due to the very short length of the ties (3 inches), the Euler buckling strength was found to be much greater than the yield strength. A theoretical effective length factor of 0.7 was used in this calculation to account for the fixity of the ties. Because of the way that the wall was actually constructed, a theoretical value of 0.5 could have been used. This was the result of a construction flaw that resulted in foam being cut out around each pair of ties and mortar being packed in the hole. This mortar was present on all ties and covered the ties through the thickness of the foam. Thus, each tie was

fixed at both ends, and the effective length of each tie would have been reduced to 0.5

inch. Figure 5.29 shows the condition of the ties during construction. Since Euler

buckling did not control, the ultimate strength of each tie was governed by its yield

strength. It was calculated that under static conditions, each tie was capable of

transmitting 1,932 lb through each leg or a total of 3,864 lb. With a vertical and

horizontal spacing of 16 inches, this meant that each tie could support a static pressure of

15.09 psi.

It is not clear what effect the constructed condition of the ties had on the global

behavior of the system. The previous calculation indicates that the ties were capable of

carrying the entire load regardless of the mortar. The only way to conclusively prove the

capability of the ties is through more testing. If more robust modeling of the ties is to be

performed, then an investigation of the actual constitutive properties of the ties should be

conducted. This investigation should also include a study on the effects of strain rate on

the ultimate strength of the ties.



**Fig. 5.29.** Actual constructed condition of wall ties

CHAPTER 6

SUMMARY AND CONCLUSIONS

## 6.1 Conclusions

Full-scale dynamic testing of two common multi-wythe insulated masonry wall sections was conducted. The data collected from this research provided great insight into the respective resistance mechanisms. However, there are questions that could be answered through further testing.

Full-scale dynamic test results indicated that the foam insulation was not significantly loaded. This is because the metal ties connecting the interior and exterior wythes transmitted all of the load. It is possible, however, that the ability of the ties to transmit all of the force was magnified by the mortar that was packed around the ties. Plans for static testing of these wall sections have been made. If the ties are installed correctly for this series of tests, then the true behavior of the ties can be studied in a static loading situation.

In Detonation 3 it was observed that Wall 2 deflected much more than Wall 3. It was also observed that the pressures and impulses on the right and left of the reaction structure were not uniform, and that the higher pressure corresponded with the larger deflection seen in Wall 2. While it is possible that A-block CMU walls behave differently from conventional CMU walls, it is unlikely that the A-block is responsible

for the reduction in deflection seen in Detonation 3. The results indicate that Wall 2 deflected more due to higher pressures caused by a non-uniform pressure distribution.

Finite element (FE) and engineering-level (EL) models were developed to study the effects of the foam insulation. Modeling efforts showed that foam is capable of increasing the resistance of the system by lowering the peak pressure applied to the primary structure. Both models indicate that thicker foam will provide more resistance. Both models also indicate that there is a relation between the added resistance and the ratio of peak reflected pressure to the compressive strength of the foam. Because the testing did not result in crushing of the foam, these models have not been validated. While the same trend was evident in the EL and FE models, there was not a good correlation between the predicted displacements. This is most likely due to three assumptions made in the development of the EL model. First, the engineering strain in the foam was assumed to be uniform for the EL model, whereas the FE model results clearly show a varying strain distribution through the thickness of the foam. Second, the EL model allows the foam to crush through the entire stress-strain curve, whereas the FE results do not indicate this behavior is accurate. Third, the FE results show that the crushing of the foam is not uniform, as assumed in the EL models, but is more pronounced at mid-span.

The blast design program SBEDS was also used to analyze the behavior of the system. It was found that SBEDS provides conservative design results and is adequate for the current construction methods. Until a wall section is developed that will allow the foam to become loaded, it would not be appropriate to use any model that includes the foam as part of the resistance definition.

## 6.2 Recommendations

It is recommended that further testing of foam insulation be conducted to gain a broader understanding of the constitutive properties. It is likely that a better approach for modeling foam would be to use an orthotropic material model. This would require obtaining stress-strain results in all three global directions as well as three measurements of Poisson's ratio. Further study of foam should also investigate strain rate effects. It is possible that under rapid loading, the foam may stiffen to the point that it essentially provides no added resistance at all. It should be possible, however, to design a foam that would increase the resistance of any structure. Overall, the methodology developed here shows that foam does have potential, and further study could lead to a system with significant added blast resistance.

As previously stated, plans for static testing of the wall sections have been made. The upcoming series of tests will experimentally determine the static resistance function of each wall section. The study should include an investigation of the different types of metal ties used in standard construction, as well as the different types of block (i.e. conventional and A-block). Further study should investigate the effects of only partially grouting the concrete masonry unit (CMU) wythe, as this could lead to a more economical design. Each type of tie should also be tested individually in compression to obtain load-deflection at different strain rates.

# REFERENCES

Baylot, J. T., Bullock, B., Slawson, T. R., and Woodson, S. C. (2005). "Blast Response of Lightly Attached Concrete Masonry Unit Walls." *Journal of Structural Engineering*, Vol. 131, No. 8, pp. 1186-1193.

Beall, C. (1993). *Masonry Design and Detailing: For Architects, Engineers, and Contractors*, McGraw-Hill, New York.

Bielenberg, R. W. and Reid, J. D. (2004). "Modeling Crushable Foam for the SAFER Racetrack Barrier." *$8^{th}$ International LS-DYNA Users Conference*, Livermore Software Technology Corporation, Livermore, CA, and Engineering Technology Associates, Inc., Troy, MI, 6.1-6.10.

Biggs, J. M. (1964). *Introduction to Structural Dynamics*, McGraw-Hill, New York.

The Brick Industry Association (1992). *Technical Notes on Brick Construction*, Chapter 3A - Brick Masonry Material Properties, Reston, VA.

Chang F. S., Hallquist J. O., Lu D. X., Shahidi B. K., Kudelko C. M., and Tekelly J. P. (1994). "Finite Element Analysis of Low-Density High-Hysteresis Foam Materials and the Application in the Automotive Industry." *Society of Automotive Engineers*, Paper No. 940908, pp. 699-706.

Dennis, S. T., Baylot, J. T., and Woodson, S. C. (2002). "Response of 1/4-Scale Concrete Masonry Unit (CMU) Walls to Blast." *Journal of Engineering Mechanics*, Vol. 128, No. 2, pp. 134-142.

Departments of the Army, the Navy, and the Air Force (1990). "Structures to Resist the Effects of Accidental Explosions." Army TM 5-1300, NAVFAC P-397, and AFR 88-22.

Eamon, C. D., Baylot, J. T., and O'Daniel, J. L. (2004). "Modeling Concrete Masonry Walls Subjected to Explosive Load." *Journal of Engineering Mechanics*, Vol. 130, No. 9, pp. 1098-1106.

Hanssen, A. G., Enstock, L., and Langseth, M. (2002). "Close-Range Blast Loading of Aluminum Foam Panels." *International Journal of Impact Engineering*, Vol. 27, No. 6, pp. 593-618.

Jenkins, R. S. (2008). *Compressive Properties of Extruded Expanded Polystyrene Foam Building Materials*. M.S.C.E. report, University of Alabama at Birmingham.

Kostopoulos, V., Markopoulos, Y. P., Giannopoulos, G., and Vlachos, D. E. (2002). "Finite Element Analysis of Impact Damage Response of Composite Motorcycle Safety Helmets." *Composites Part B: Engineering*, Vol. 33, No. 2, pp. 99-107.

Randers-Pehrson, G. and Bannister, K. A. (1997). "Airblast Loading Model for DYNA2D and DYNA3D." Army Research Laboratory, ARL-TR-1310.

Schenker, A., Anteby, I., Nizri, E., Ostraich, B., Kivity, Y., Sadot, O., Haham, O., Michaelis, R., Gal, E., and Ben-Dor, G. (2005). "Foam-Protected Reinforced Concrete Structures under Impact: Experimental and Numerical Studies." *Journal of Structural Engineering*, Vol. 131, No. 8, pp. 1233-1242.

Tedesco, J. W., McDougal, W. G., and Ross, C. A. (1999). *Structural Dynamics: Theory and Applications*, Addison Wesley Longman, California.

U.S. Army Corps of Engineers Protective Design Center (2006). "Methodology Manual

for the Single-Degree-of-Freedom Blast Effects Design Spreadsheets (SBEDS)." PDC-TR 06-01.

U.S. Army Corps of Engineers Protective Design Center (2006). "User's Guide for the Single-Degree-of-Freedom Blast Effects Design Spreadsheets (SBEDS)." PDC-TR 06-02.

Ye, Z. Q. and Ma, G. W. (2007). "Effects of Foam Claddings for Structure Protection against Blast Loads." *Journal of Engineering Mechanics*, Vol. 133, No. 1, pp. 41-47.

```
*KEYWORD
*TITLE
Dow2
*CONTROL_CONTACT
$#   slsfac   rwpnal   islchk   shlthk   penopt   thkchg    orien   enmass
   0.100000    0.000        2        0        1        1        1        1
$#   usrstr   usrfrc    nsbcs   interm    xpene    ssthk     ecdt  tiedprj
        0        0       10        0 4.000000
$#    sfric    dfric      edc      vfc       th    th_sf   pen_sf
    0.000    0.000    0.000    0.000    0.000    0.000    0.000
$#   ignore   frceng  skiprwg   outseg  spotstp  spotdel  spothin
        0        0        0        0        0        0    0.000
$#     isym   nserod   rwgaps   rwgdth    rwksf     icov        x   ithoff
        0        0        0    0.000 1.000000        0 1.000000
*CONTROL_ENERGY
$#     hgen     rwen   slnten    rylen
        2        2        2        2
*CONTROL_OUTPUT
$#    npopt   neecho   nrefup   iaccop    opifs   ipnint   ikedit   iflush
        0        0        0        0    0.000        0      100     5000
$#    iprtf   ierode    tet10   msgmax   ipcurv
        0        0        0        0        0
*CONTROL_SHELL
$#   wrpang    esort    irnxx   istupd   theory      bwc    miter     proj
20.000000        2       -1        0        2        2        1
$#   rotascl   intgrd   lamsht   cstyp6   tshell   nfail1   nfail4  psnfail
 1.000000
$#   psstupd   irquad
        0        0
*CONTROL_SOLID
$#    esort  fmatrix  niptets
        0        0        4
$#     pm1      pm2    pm3     pm4      pm5      pm6      pm7    pm8      pm9    pm10
        0        0      0       0        0        0        0      0        0       0
*CONTROL_TERMINATION
$#   endtim   endcyc    dtmin   endeng   endmas
 0.150000
*CONTROL_TIMESTEP
$#   dtinit    tssfac     isdo   tslimt    dt2ms     lctm    erode    ms1st
    0.000 0.900000        0    0.000    0.000        0        1
$#   dt2msf   dt2mslc    imscl
    0.000        0        0
*DATABASE_ELOUT
$#       dt   binary     lcur    ioopt
 5.0000E-4        1
*DATABASE_GLSTAT
$#       dt   binary     lcur    ioopt
 5.0000E-4        1
*DATABASE_MATSUM
$#       dt   binary     lcur    ioopt
 5.0000E-4        1
*DATABASE_NCFORC
```

```
$#        dt      binary       lcur       ioopt
 5.0000E-4                 1
*DATABASE_NODFOR
$#        dt      binary       lcur       ioopt
 5.0000E-4                 1
*DATABASE_NODOUT
$#        dt      binary       lcur       ioopt       dthf       binhf
 5.0000E-4                 1
*DATABASE_RCFORC
$#        dt      binary       lcur       ioopt
 5.0000E-4                 1
*DATABASE_SLEOUT
$#        dt      binary       lcur       ioopt
 5.0000E-4                 1
*DATABASE_SPHOUT
$#        dt      binary       lcur       ioopt
 5.0000E-4                 1
*DATABASE_BINARY_D3PLOT
$#        dt        lcdt       beam       npltc
 5.0000E-4
$#     ioopt
          0
*DATABASE_BINARY_D3THDT
$#        dt        lcdt
 5.0000E-4
*DATABASE_EXTENT_BINARY
$#     neiph      neips      maxint      strflg      sigflg      epsflg      rltflg      engflg
           0          0           3           1           1           1           1           1
$#   cmpflg     ieverp      beamip       dcomp        shge       stssz      n3thdt     ialemat
           0          0           1           0           0           0           2
$# nintsld    pkp_sen        sclp      unused       msscl        therm
           1
*DATABASE_HISTORY_NODE_SET
$#       id1        id2         id3         id4         id5         id6         id7         id8
           0          0           0           0           0           0           0           0
$#       id1        id2         id3         id4         id5         id6         id7         id8
           0          0           0           0           0           0           0           0
*LOAD_SEGMENT_SET_ID
$#        id                                                                           heading
           1
$#      ssid       lcid          sf          at
        3001          1    1.000000
*LOAD_SEGMENT_SET_ID
$#        id                                                                           heading
           2
$#      ssid       lcid          sf          at
        1002          2   -1.000000
*CONTACT_AUTOMATIC_SURFACE_TO_SURFACE_ID
$#       cid                                                                             title
           1
$#      ssid       msid       sstyp       mstyp      sboxid      mboxid         spr         mpr
        5001       1002           0           0           0           0           1           1
$#        fs         fd          dc          vc         vdc      penchk          bt          dt
  0.800000   0.600000       0.000       0.000       0.000           0      0.0001 1.0000E+20
$#       sfs        sfm         sst         mst        sfst        sfmt         fsf         vsf
  1.000000   1.000000       0.000       0.000    1.000000    1.000000    1.000000    1.000000
*SET_SEGMENT_TITLE
Support_Surface
$#       sid        da1         da2         da3         da4
        5001
$#        n1         n2          n3          n4          a1          a2          a3          a4
  50002256   50002258    50002264    50002262
  50002258   50002260    50002266    50002264
.
.
.
  50002832   50002834    50002840    50002838
  50002834   50002836    50002842    50002840
*SET_SEGMENT_TITLE
```

183

```
Concrete_Rear
$#     sid       da1       da2       da3       da4
      1002
$#      n1        n2        n3        n4        a1        a2        a3        a4
   1000010   1000001   1001162   1001171
   1000019   1000010   1001171   1001180
.
.
.
   1055711   1055702   1056863   1056872
   1055720   1055711   1056872   1056881
*PART
$# title
Concrete
$#     pid     secid       mid     eosid      hgid      grav    adpopt      tmid
       100         1         1
*SECTION_SOLID_TITLE
Concrete Hex Element
$#   secid     elform       aet
         1         1
*MAT_BRITTLE_DAMAGE_TITLE
CONCRETE_96
$#     mid        ro         e        pr    tlimit    slimit    ftough    sreten
         1 1.7970E-4 2.1690E+6  0.200000 375.00000 1250.0000  0.800000  0.030000
$#    visc    fra_rf      e_rf     ys_rf     eh_rf     fs_rf      sigy
 104.00000     0.000     0.000     0.000     0.000     0.000 2500.0000
*PART
$# title
REBAR
$#     pid     secid       mid     eosid      hgid      grav    adpopt      tmid
       200         2         2
*SECTION_BEAM_TITLE
Rebar Beam Element
$#   secid     elform      shrf   qr/irid       cst     scoor       nsm
         2         1  1.000000         2         1
$#     ts1       ts2       tt1       tt2     nsloc     ntloc
  0.625000  0.625000
*MAT_PLASTIC_KINEMATIC_TITLE
REINFORCING_STEEL_3
$#     mid        ro         e        pr      sigy      etan      beta
         2 7.3390E-4 2.9000E+7  0.290000 60000.000
$#     src       srp        fs        vp
     0.000     0.000  0.180000
*PART
$# title
Foam
$#     pid     secid       mid     eosid      hgid      grav    adpopt      tmid
       500         3       301
*SECTION_SOLID_TITLE
Foam Element
$#   secid     elform       aet
         3         2
*MAT_CRUSHABLE_FOAM_TITLE
Dow_Foam
$#     mid        ro         e        pr      lcid       tsc      damp
       301 2.5527E-6 1790.0000     0.000       301 50.000000  0.100000
*PART
$# title
SUPPORT
$#     pid     secid       mid     eosid      hgid      grav    adpopt      tmid
       501         5         5
*SECTION_SOLID_TITLE
Rigid Hex Element
$#   secid     elform       aet
         5         1
*MAT_RIGID_TITLE
BOUNDARY_20
$#     mid        ro         e        pr         n    couple         m     alias
         5 7.3390E-4 3.0000E+7  0.300000     0.000     0.000     0.000
```

```
$#      cmo      con1      con2
        1.00       7.0       7.0
$#lco or a1      a2        a3        v1        v2        v3
       0.000     0.000     0.000     0.000     0.000     0.000
*DEFINE_CURVE_TITLE
Dow_Curve
$#     lcid      sidr       sfa       sfo      offa      offo    dattyp
        301         0  1.000000  1.000000
$#                a1                  o1
               0.000               0.000
          0.0010000           1.7895910
          0.0020000           3.5791810
          0.0030000           5.3687720
          0.0040000           7.1944108
.
.
.
          0.9650000          67.3277969
          0.9676000          67.4795303
*DEFINE_CURVE_TITLE
LOAD_A
$#     lcid      sidr       sfa       sfo      offa      offo    dattyp
          1         0  1.000000  1.000000
$#                a1                  o1
               0.000         188.1264343
          0.0001000         179.9953766
          0.0002000         172.2073517
          0.0003000         164.7481537
          0.0004000         157.6041870
          0.0005000         150.7639160
.
.
.
          0.0145000           0.0177344
          0.0146000           0.0116966
          0.0147000           0.0060778
          0.0148000       8.5674942e-004
          0.0149000           0.0000000
*DEFINE_CURVE_TITLE
LOAD_B
$#     lcid      sidr       sfa       sfo      offa      offo    dattyp
          2         0  1.000000  1.000000
$#                a1                  o1
               0.000           0.0000000
          0.0148000           0.0000000
          0.0149000          -0.1346723
          0.0150000          -0.1898044
          0.0151000          -0.2446647
.
.
.
          0.0922000      -7.0250803e-004
          0.0923000      -3.3392521e-004
          0.0924000      -1.0251004e-004
          0.0925000      -7.2998687e-006
          0.0926000           0.0000000
*SET_SEGMENT_TITLE
Foam_Front
$#      sid       da1       da2       da3       da4
       3001
$#       n1        n2        n3        n4        a1        a2        a3        a4
   55000002  55000005  55000392  55000389
   55000005  55000008  55000395  55000392
.
.
.
   55018569  55018572  55018959  55018956
   55018572  55018575  55018962  55018959
*ELEMENT_SOLID
```

185

```
$#    eid    pid     n1      n2      n3      n4      n5      n6      n7      n8
 1000001    100 1000001 1000002 1000011 1000010 1001162 1001163 1001172 1001171
 1000002    100 1000002 1000003 1000012 1000011 1001163 1001164 1001173 1001172
 1000003    100 1000003 1000004 1000013 1000012 1001164 1001165 1001174 1001173
 1000004    100 1000004 1000005 1000014 1000013 1001165 1001166 1001175 1001174
.
.
.
 2000129      50150002255500022565000225850002257500022615000226250002264500022630
 2000130      50150002257500022585000226050002259500022635000226450002266500022655
 2000131      50150002261500022625000226450002263500022675000226850002270500022695
 2000132      50150002263500022645000226650002265500022695000227050002272500022715
.
.
.
55000000      500 10000095500000155000041000018 1001170550003885500039110001179
55000001      50055000001550000025500000555000045500038855000389550003925500039155000391
55000002      500 10000185500000455000071000027 10011795500039155000394100011885
55000003      50055000004550000055500000855000075500391550003925500039555000394
*ELEMENT_BEAM
$#    eid    pid     n1      n2      n3     rt1     rr1     rt2     rr2   local
 2000001    200 2000001 2000002 2000003
 2000002    200 2000002 2000004 2000005
 2000003    200 2000004 2000006 2000007
 2000004    200 2000006 2000008 2000009
.
.
.
 2000125    200 2000248 2000250 2000251
 2000126    200 2000250 2000252 2000253
 2000127    200 2000252 2000254 2000255
 2000128    200 2000254 2000256 2000257
*ELEMENT_MASS
$#    eid    nid              mass     pid
       155000392  7.1888999e-004
       255000395  7.1888999e-004
       355000398  7.1888999e-004
       455000401  7.1888999e-004
.
.
.
    597155000005  3.5943999e-004
    597255000008  3.5943999e-004
    597355000011  3.5943999e-004
    597455000014  3.5943999e-004
.
.
.
    632255000386  1.7971999e-004
    632355018962  1.7971999e-004
    632455018578  1.7971999e-004
    632555000002  1.7971999e-004
*NODE
$#    nid              x               y               z      tc      rc
 1000001
 1000002      0.9531250
 1000003      1.9062500
 1000004      2.8593750
 1000005      3.8125000
.
.
.
55018956      9.6250000     126.0000000      48.0000000
55018958      8.6250000     127.0000000      48.0000000
55018959      9.6250000     127.0000000      48.0000000
55018961      8.6250000     128.0000000      48.0000000
55018962      9.6250000     128.0000000      48.0000000
*END
```